KYRGYZ TURKISH MANAS UNIVERSITY
MANAS JOURNAL OF ENGINEERING (MJEN)

ISSN: 1694-7398
Year: 2023
Volume: 11
Issue: 2
http://journals.manas.edu.kg
journals@manas.edu.kg

PUBLICATION PERIOD

Manas Journal of Engineering (MJEN) is published twice year, MJEN is a peer reviewed journal.

CORRESPONDENCE ADDRESS
Kyrgyz Turkish Manas University
Chyngyz Aitmatov Avenue 56 Bishkek, KYRGYZSTAN
URL: http://journals.manas.edu.kg
e-mail: journals@manas.edu.kg
Tel : +996 312 492763- Fax: +996 312 541935

CONTENT

*correction

MANAS Journal of Engineering
ISSN 1694-7398 | e-ISSN 1694-7398

Volume 11, Issue 2, (2023) Pages 166-175
https://doi.org/10.51354/mjen.1217597

A method for calculation of lateral displacements of buildings under distributed loads

Duygu OZTURK[1*], Kanat Burak BOZDOGAN[2], Suleyman AYDIN[3]

[1] Ege University, Izmir, Turkey, duygu.ozturk@ege.edu.tr, ORCID: 0000-0001-7800-7438

[2] Çanakkale Onsekiz Mart University, Çanakkale, Turkey, kbbozdogan@comu.edu.tr, ORCID: 0000-0001-7528-2418

[3] Kırklareli University, Kırklareli, Turkey, suleyman.aydin@klu.edu.tr, ORCID: 0000-0003-2489-9906

ABSTRACT

Lateral displacement is a vary important parameter that we need to calculate when structures are subjected to lateral loads like earthquake and wind loads. In this study, a method is proposed for lateral displacement calculation of structures with different structural systems in different planes. This method is based on the continuum system calculation model. The method suggested in the literature for only top displacement in the case of uniform loading, is developed in this study for the calculation of displacements at each storey level and also in both uniform and triangular loading conditions. At the end of the study, twenty-eight storey building with shear wall-frame bearing system, which was taken from the literature, was solved with the presented method and Finite Element Method. The shear walls were modelled with three different element types for the analysis with the Finite Element Method with structural engineering program used. The results, obtained from the Continuum Method and Finite Element Method were presented in tables and by figures. Thus, the compatibility of the proposed method with the classical Finite Element Method was investigated. From the compared results of the method and the literature or finite element models it was seen that the method used for the case of uniform or triangular distributed loading gives very close results.

ARTICLE INFO

Research article

Received:12.12.2022
Accepted:4.07.2023

Keywords:
Lateral displacement,
uniform distributed load,
triangular distributed load,
timoshenko beam model

**Corresponding author*

1. Introduction

The desire of people to live in big cities for various reasons has increased the immigration to these cities. The increase in immigration has created the need for infrastructure and dwelling in cities. In order to meet these needs and to provide more economical use of residential areas, reinforced concrete or steel multi-storey structures were designed and built. In multi-storey buildings, the lateral loads on the structure increase with the increase in the height of the building. Therefore, lateral loads become more effective than vertical loads in the dimensioning of the bearing systems of such structures. At the same time, under the effect of increasing lateral loads, lateral displacements in the buildings reach high values and as a result, buildings can be damaged. Dynamic analysis is essential to determine this behavior of structures. However, equivalent static analysis methods are still used in low-rise and regular buildings, and the results obtained with dynamic analysis in all buildings are limited to the results obtained with the equivalent static analysis method.

Although static and dynamic calculations of buildings can be made quickly in parallel with the development of computer programs in recent years, approximate methods still maintain their importance both in the pre-sizing stage and in terms of controlling the program outputs. In the programs that analyze with the Finite Element Method, wrong results can be obtained as a result of the wrong element and model selection. At the same time, the structural behavior, which is difficult to understand in the inputs and outputs of complex finite element programs that make element-based analysis, is better understood by using approximate calculation methods and a few parameters. One of the methods used in the analysis of buildings is the Continuum Method. In this method, the multi-storey building is modeled as an equivalent cantilever beam.

The Continuum Method first emerged at the end of the 1940s. Chitty studied the behavior of parallel cantilever beams [1]. Rossmann performed the static analysis of shear walls under

lateral loads using the Continuum Method [2]. Rutenberg and Heidebrecht used the Continuum Method in the analysis of asymmetrical buildings [3]. Murashev et al. conducted studies on the method and applied the method in housing estate projects [4]. The method has been studied by many researchers [5, 6, 7, 8, 9, 10, 11, 12, 13, 14, 15, 16, 17, 1, 19, 20, 21, 22, 23, 24, 25, 26, 27, 28, 29, 30, 31, 32, 33, 34, 35] since then, and studies on the method are still ongoing. In Turkey, a number of studies have been carried out in the literature about the method used and developed by Bilyap [36] and his colleagues, called the Differential Equation Method. [37, 3, 39, 40, 41, 42, 43].

In this study, a method has been proposed for calculating lateral displacements of buildings with different structural systems in different planes. The method, which was suggested in the literature for only top displacement in the case of uniform loading, was developed in this study for the calculation of displacements at each storey level in both uniform and triangular loading conditions.

The following assumptions were made in the development of the method:

a) The material is linear elastic,
b) Second-order effects are negligible,
c) The axial and shear deformations in the beams are negligible,
d) The material, geometry and section properties of the building are constant throughout the height of the building.

2. Methods and materials

Each of the bearing systems (wall, frame) in different planes can be modeled as an equivalent Timoshenko beam as shown in Figure 1.

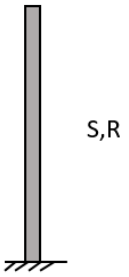

Figure 1 *Equivalent Timoshenko beam*

The total displacement (y) of the equivalent Timoshenko beam is equal to the sum of the bending displacement (y_e) and the shear displacement (y_k) as in Equation (1)

$$y = y_e + y_k \tag{1}$$

In the equivalent Timoshenko beam, S denotes the bending stiffness and corresponds to the global bending stiffness created by the axial displacements in the frames and is calculated with the following equation.

$$S = D = E\sum_{i=1}^{m}\left(A_i t_i^2\right) \tag{2}$$

In this equation; Ai is the cross-sectional area of the i^{th} column element, t^i is the distance of the i^{th} column element to the center of gravity of the column system, m is the number of elements.

For shear walls, S represents the bending stiffness of the wall and can be calculated by Equation (3).

$$S = EI = \sum_{i=1}^{n}\left(EI_i\right) \tag{3}$$

R, seen in Figure 1, shows the shear stiffness of the equivalent Timoshenko beam and is calculated with the following equation for frames.

$$R = \frac{12}{h\left(\frac{1}{r}+\frac{1}{s}\right)} \tag{4}$$

In this equation; r is the sum of all beams stiffness factors, s is the sum of all column stiffness factors at the storey, and h is the storey height. r and s are calculated by Equation (5) and Equation (6), respectively.

$$r = \sum_{i=1}^{n-1}\left(\frac{EI_{ki}}{l_i}\right) \tag{5}$$

$$s = \sum_{i=1}^{n}\left(\frac{EI_{ci}}{h_i}\right) \tag{6}$$

In the above equations; n is the total number of columns, EI_{ki} is the total bending stiffness of the beams, EI_{ci} is the total bending stiffness of the columns, l_i is the length of i^{th} beam, h_i represents the height of each column at the storey.

For shear wall elements, R can be calculated by Equation (7).

$$R = \frac{E}{k*2*(1+\mu)}*A \tag{7}$$

Here, A is the cross-sectional area of the shear wall, k is the shear shape factor, and μ is the poisson's ratio. k is defined as 1.2 for rectangular sections.

2.1 Uniformly Distributed Load Case

In the case of a uniformly distributed load (Figure 2), the displacement (y_e) caused by bending is calculated by Equation (8).

$$y_e(z) = \frac{q}{S}\left[\frac{z^4}{24} - \frac{Hz^3}{6} + \frac{H^2 z^2}{4}\right] \quad (8)$$

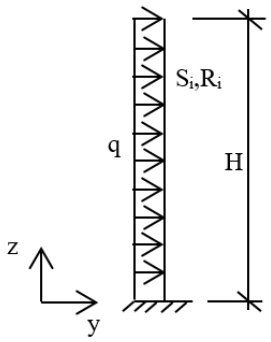

Figure 2 *Equivalent Timoshenko beam under uniformly distributed load*

The displacement caused by shear is calculated by Equation (9).

$$y_k = \frac{qH^2}{2R}\left[\frac{z}{H} - \frac{z^2}{2H^2}\right] \quad (9)$$

2.2 Triangle Distributed Load Case

In case of triangular distributed load shown in Figure 3, the displacement (y_e) caused by bending is calculated by Equation (10).

$$y_e(z) = \frac{q}{S}\left[\frac{z^5}{120H} - \frac{Hz^3}{12} + \frac{H^2 z^2}{6}\right] \quad (10)$$

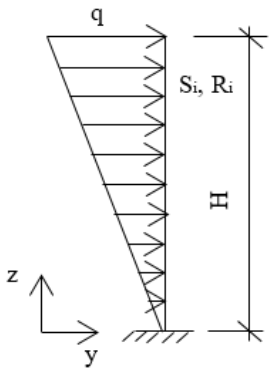

Figure 3 *Equivalent Timoshenko beam under triangular distributed load*

The displacement (y_k) caused by shear is calculated by Equation (11).

$$y_k = -\frac{qz^3}{6HR} + \frac{qH}{2R}z \quad (11)$$

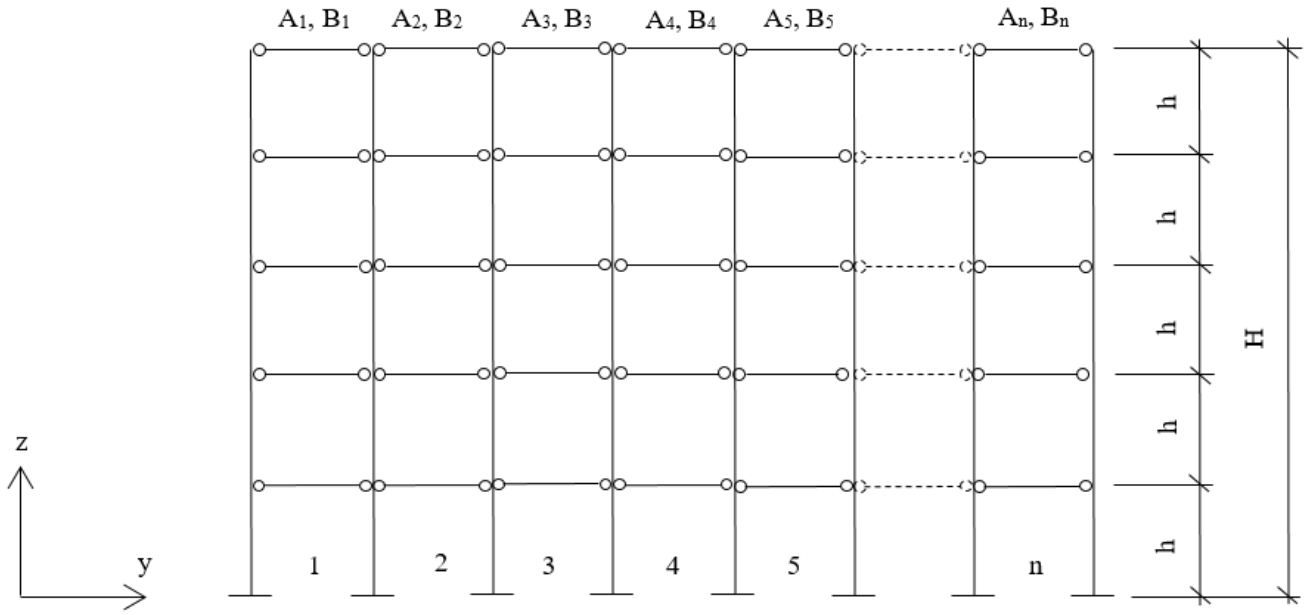

Figure 4. *Equivalent Timoshenko beam models representing the different bearing systems in different planes*

For element j^{th} in Figure 4, the relative storey drift at i^{th} storey is calculated by Equation (12).

$$\Delta_i^j = y_{i+1} - y_i \tag{12}$$

In this equation, y_{i+1}, y_i represent the total displacements at i+1 and i^{th} stories, respectively.
With the shear beam assumption, the lateral shear stiffness of the j^{th} bearing system at i^{th} storey is calculated by Equation (13).

$$k_i^j = \frac{V_i}{\Delta_i^j} \tag{13}$$

In this equation, k_i^j represents the lateral stiffness of the j^{th} element, V_i represents the shear force and Δ_i^j represents the relative storey drifts of the j^{th} element at i^{th} storey. The total stiffness of each storey is calculated with Equation (14).

$$K_i = \sum_{j=1}^{n} k_i^j \tag{14}$$

The drift of the i^{th} storey of the building is calculated with the following equation.

$$\Delta_i = \frac{V_i}{K_i} \tag{15}$$

3. Methods and materials

3.1 Example:

In the example taken from the literature [35], 28-storey reinforced concrete structure whose layout is shown in Figure 5 and whose cross-sectional features are shown in Table 1 was investigated. In this structure; the height of each storey was 3.00 m, the Modulus Elasticity was $25*10^6$ kN/m^2 and the poisson ratio was 0.2.

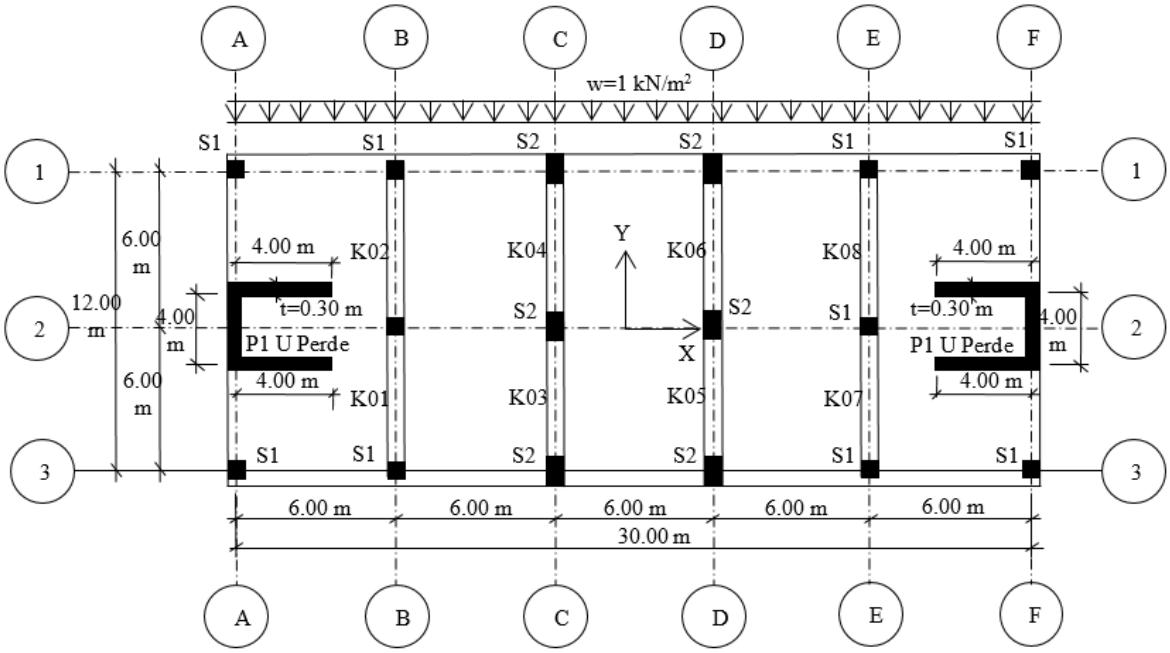

Figure 5. *Layout of the example [35]*

Table 1. *Cross-sections of the building elements*

Beam / Column	Dimensions (m)
K01, K02, K03, K04, K05, K06, K07, K08	0.40/0.40
S1	0.40/0.40
S2	0.40/0.70

In the example, the weight of the building was neglected and the lateral displacements of the building under uniformly distributed load representing the wind loads in the (–y) direction, were calculated analytically by the proposed method and by using the SAP2000 program to analyze with the Finite Element Method.

The lateral displacement of the top floor of the building under uniformly distributed load representing the wind load in the (-y) direction in the same example, was calculated by Zalka [35] as 0.184 m.

In this study, the lateral displacement values at each storey were calculated and shown in the table. In addition, 3 models were used to idealize the structure in the SAP2000 package program for Finite Element Analysis.

In the first model, the centers of gravity of the U-section wall elements were calculated. Then, the strength properties of these shear walls were calculated and these properties were assigned to the frame elements.

In the second model, each rectangular wall element constituting the U-section wall elements was formed as a frame element and assigned to the center of gravity of these elements. Then, these frame elements were connected to each other with infinitely rigid frame elements.

In the third model, each wall element constituting the U-section wall elements was considered as a shell element and divided into 20x20 cm in size square elements.

In all three models, the slabs were assumed to be infinitely rigid and at each storey rigid diaphragms were assigned.

The lateral displacement of each storey in the y-axis direction was calculated by analytical and Finite Element Methods, then shown in Table 2 and in the graph in Figure 6, comparatively.

.

Table 2. *Comparison of lateral storey displacements under uniformly distributed load*

	Lateral Displacements in the y axis line (m)			
Number of Storey	**Model 1**	**Model 2**	**Model 3**	**Analytical**
Ground Floor	-0.0008	-0.0009	-0.0009	-0.0009
1.	-0.0027	-0.0029	-0.0029	-0.0032
2.	-0.0056	-0.0059	-0.0058	-0.0067
3.	-0.0092	-0.0096	-0.0096	-0.0112
4.	-0.0137	-0.0141	-0.0141	-0.0166
5.	-0.0188	-0.0193	-0.0192	-0.0226
6.	-0.0244	-0.025	-0.0249	-0.0292
7.	-0.0306	-0.0313	-0.0311	-0.0363
8.	-0.0372	-0.0380	-0.0378	-0.0437
9.	-0.0442	-0.0450	-0.0448	-0.0515
10.	-0.0515	-0.0524	-0.0520	-0.0595
11.	-0.0591	-0.0600	-0.0596	-0.0676
12.	-0.0668	-0.0678	-0.0673	-0.0759
13.	-0.0748	-0.0757	-0.0752	-0.0842
14.	-0.0828	-0.0838	-0.0833	-0.0925
15.	-0.0910	-0.0920	-0.0914	-0.1007
16.	-0.0992	-0.1002	-0.0995	-0.1088
17.	-0.1074	-0.1085	-0.1077	-0.1168
18.	-0.1156	-0.1167	-0.1159	-0.1247
19.	-0.1238	-0.1249	-0.1240	-0.1323
20.	-0.1320	-0.1331	-0.1321	-0.1396
21.	-0.1401	-0.1413	-0.1402	-0.1467
22.	-0.1482	-0.1494	-0.1482	-0.1534
23.	-0.1563	-0.1574	-0.1562	-0.1598
24.	-0.1642	-0.1654	-0.1641	-0.1658
25.	-0.1722	-0.1733	-0.1720	-0.1713
26.	-0.1800	-0.1812	-0.1798	-0.1763
27.	-0.1879	-0.1890	-0.1875	-0.1807

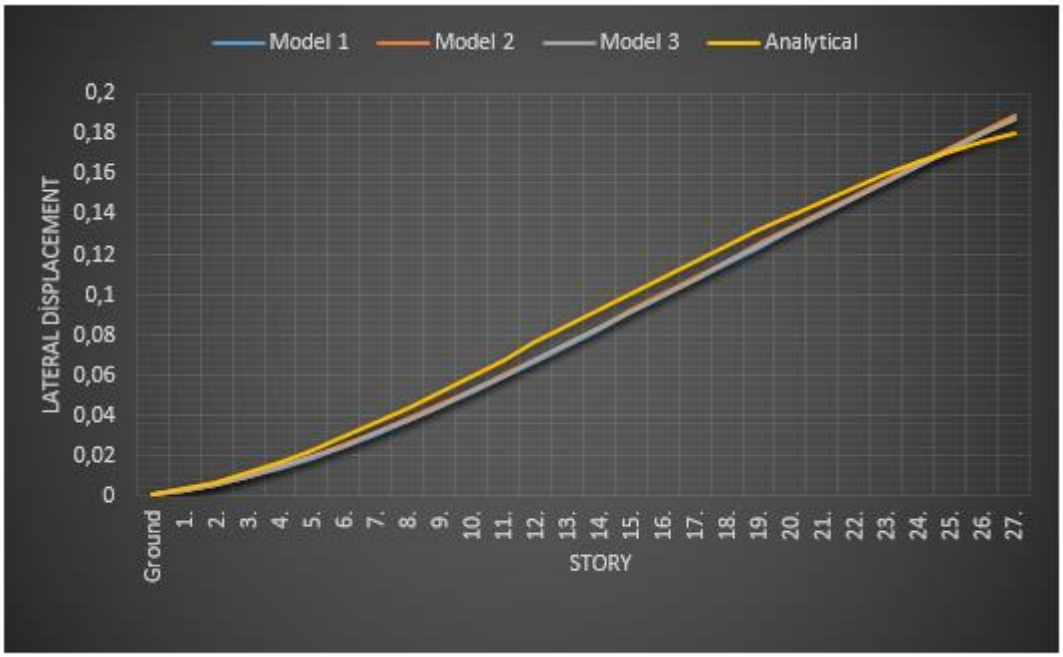

Figure 6. *Graphical comparison of lateral storey displacements under uniformly distributed load*

For the same example, the lateral displacement of each storey of the building under the triangular distributed load representing the earthquake loads in the (–y) direction shown in Figure 7 was calculated both analytically and using the SAP2000 program, which analyzes with the Finite Element Method.

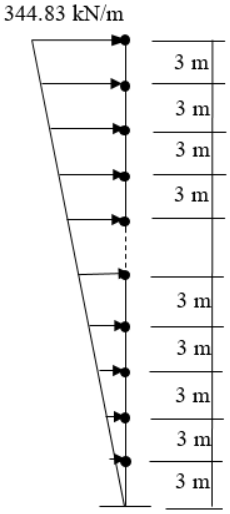

Figure 7. *Triangular distributed load*

The results obtained by the calculation of the displacements in the (–y) direction of each storey using analytical and Finite Element Method are shown in Table 3 and in the graph in Figure 8, comparatively.

.

Table 3. *Comparison of lateral storey displacements under triangular distributed load*

	Lateral Displacements in the y axis line (m)			
Number of Storey	**Model 1**	**Model 2**	**Model 3**	**Analytical**
Ground Floor	-0.0020	-0.0022	-0.0022	-0.0023
1.	-0.0068	-0.0073	-0.0072	-0.0084
2.	-0.0142	-0.0149	-0.0148	-0.0175
3.	-0.0240	-0.0248	-0.0247	-0.0294
4.	-0.0359	-0.0369	-0.0368	-0.0435
5.	-0.0498	-0.0510	-0.0507	-0.0597
6.	-0.0655	-0.0668	-0.0664	-0.0775
7.	-0.0827	-0.0842	-0.0837	-0.0969
8.	-0.1013	-0.1030	-0.1024	-0.1175
9.	-0.1212	-0.1230	-0.1223	-0.1391
10.	-0.1422	-0.1442	-0.1432	-0.1617
11.	-0.1642	-0.1662	-0.1651	-0.1849
12.	-0.1869	-0.1891	-0.1878	-0.2087
13.	-0.2103	-0.2126	-0.2111	-0.2328
14.	-0.2343	-0.2367	-0.2350	-0.2572
15.	-0.2587	-0.2612	-0.2593	-0.2817
16.	-0.2834	-0.2860	-0.2839	-0.3062
17.	-0.3084	-0.3110	-0.3088	-0.3304
18.	-0.3335	-0.3362	-0.3337	-0.3543

19.	-0.3587	-0.3615	-0.3588	-0.3778
20.	-0.3839	-0.3867	-0.3838	-0.4007
21.	-0.4091	-0.4120	-0.4088	-0.4228
22.	-0.4342	-0.4371	-0.4337	-0.4439
23.	-0.4592	-0.4621	-0.4585	-0.4641
24.	-0.4840	-0.4869	-0.4832	-0.4829
25.	-0.5087	-0.5116	-0.5077	-0.5002
26.	-0.5333	-0.5362	-0.5320	-0.5158
27.	-0.5578	-0.5606	-0.5562	-0.5293

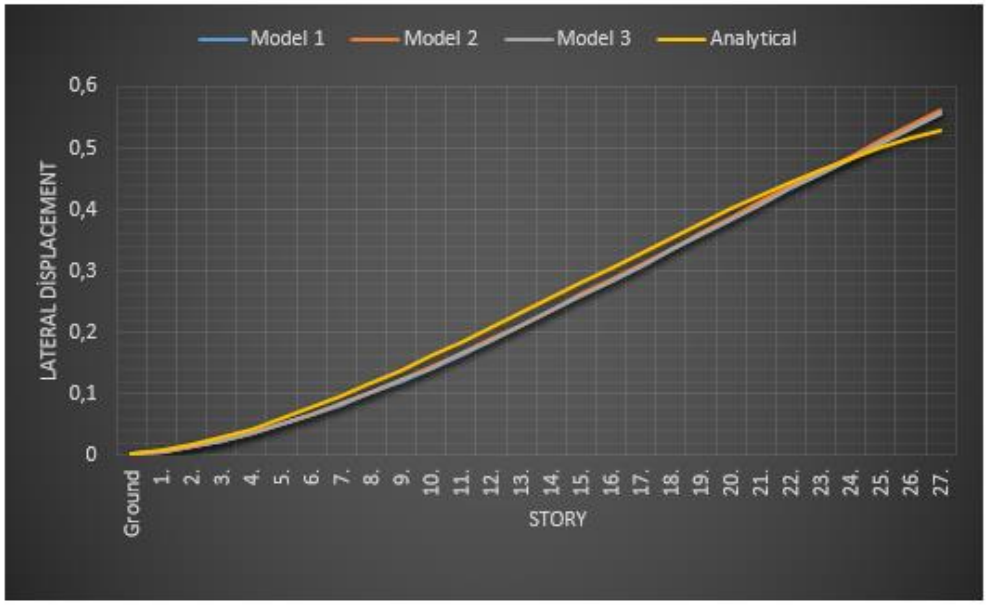

Figure 8. *Graphical comparison of lateral storey displacements under triangular distributed load*

4. Conclusions

In this study, a practical method was proposed to determine the lateral displacements at each storey level of the buildings. The method which was suggested in the literature for only top displacement in the case of uniform loading, was developed in this study for the calculation of displacements at each storey level. In addition to the uniform loading presenting the wind loads, triangular loading presenting the earthquake loads was developed in this study.

At the end of the study, example taken from the literature was solved with the presented method. In addition, for the same example, the lateral displacement at each storey was calculated using different models created by the Finite Element Method. The lateral displacement of the top floor of the building under uniformly distributed load was calculated as 0.184 m in the literature, which was calculated as 0.1807 m by the proposed method. Also for the different three models created by the Finite Element Method the lateral displacement of the top floor was calculated as 0.1879m, 0.1890 m and 0.1875 m. For the convergence of the presented method with respect to the Finite Element Method, it was seen from tables that in the case of uniform and triangular distributed loads, close results were obtained. Thus, the presented method can be used especially in the pre-sizing stage and controlling the package programs.

References

[1] Chitty L., "On the cantilever composed of a number of parallel beams interconnected by cross bars", Philosophical Magazine, London, Series, 7 (38), (1947), 685–699.

[2] Rosman R., "Approximate analysis of shear walls subject to lateral loads", Proceedings of the American Concrete Institute, 61(6), (1964), 717–734.

[3] Rutenberg, A., Heidebrecht A.C., "Approximate analysis of asymmetric wall-frame structures", Building Science, 10(1), (1975), 731–745.

[4] Murashev, V., Sigalov, E., Baikov, V.N., "Design of reinforced concrete structures", Moscow, Mir Publishers, 1976.

[5] Basu, A.K., Nagpal, A.K., & Kaul, S., "Charts for seismic design of frame-wall systems", Journal of Structural Engineering ASCE ,110 (1), (1984), 31–46.

[6] Stafford Smith B, Crowe E., "Estimating periods of vibration of tall building", Journal of the Structural Division, ASCE 112(5), (1986), 1005–1019.

[7] Smith B. S., Yoon Y. S., "Estimating seismic base shears of tall wall-frame buildings", Journal of Structural Engineering ASCE, 117(10), (1991), 3026-3041.

[8] Mancini, E., Savassi, W., "Tall building structures unified plane panels behavior", Structural Design of Tall Buildings, 8, (1999), 155–170.

[9] Ng, S.C., Kuang, J.S, "Triply coupled vibration of asymmetric wall–frame structures", Journal of Structural Engineering ASCE, 126 (8), (2000), 982–987.

[10] Wang, Y., Arnaouti, C., Guo S., "A simple approximate formulation for the first two frequencies of asymmetric wall–frame multi-storey building structures", Journal of Sound and Vibration, 236 (1), (2000), 141–160.

[11] Swaddiwudhipong, S, Lee S.L, Zhou Q., "Effect of axial deformation on vibration of tall buildings", Structural Design of Tall Buildings 10, (2001), 79–91.

[12] Zalka, K.A., "Simplified method for calculation of the natural frequencies of wall–frame buildings", Engineering Structures, 23 (12), (2001), 1544-1555.

[13] Hoenderkamp, J. C. D., "Simplified analysis of asymmetric high-rise structures with cores", The Structural Design of Tall Buildings, 11(2), (2002), 93-107.

[14] Miranda,E., Reyes, C.J., "Approximate lateral drift demands in multistory buildings with nonuniform stiffness", Journal of Structural Engineering ASCE, 128 (7), (2002), 840–849.

[15] Tarján, G. ,László P.K., "Approximate analysis of building structures with identical stories subjected to earthquakes", International Journal of Solids and Structures, 41(5-6), (2004), 1411-1433.

[16] Miranda, E., Akkar, S D., "Generalized interstory drift spectrum", Journal of Structural Engineering ASCE, 132(6), (2006), 840–852.

[17] Clive L.D.,Harry. E.W., "Estimating fundamental frequencies of tall buildings", Journal of Structural Engineering ASCE, 133(10), (2007), 1479-1483.

[18] Georgoussis, G.K., "Approximate analysis of symmetrical structures consisting of different types of bents", The Structural Design of Tall and Special Buildings, 16(3), (2007), 231-247.

[19] Meftah S.A., Tounsi A., El Abbas A.B., "A simplified approach for seismic calculation of a tall building braced by shear walls and thin-walled open section structures", Journal of Engineering Structure, 29(10), (2007), 2576-2585.

[20] Laier ,J.E., "An improved continuous medium technique for structural frame analysis", The Structural Design of Tall and Special Buildings, 17(1), (2008), 25-38.

[21] Rafezy, R. , Howson, W.P., "Vibration analysis of doubly asymmetric, three-dimensional structures comprising wall and frame assemblies with variable cross-section", Journal of Sound and Vibration, 318 (1–2), (2008), 247-266.

[22] Bozdogan, KB., "An approximate method for static and dynamic analyses of symmetric wall-frame buildings", The Structural Design of Tall and Special Buildings, 18(3), (2009), 279–290.

[23] Takabatake, H., "Two-dimensional rod theory for approximate analysis of building structures", Earthquakes and Structures, 1(1), (2010), 1–19.

[24] Bozdogan, K.B., "A method for lateral static and dynamic analyses of wall-frame buildings using one dimensional finite element", Scientific Research and Essays 6(3), (2011), 616-626.

[25] Wdowicki, J., Wdowicka, E., "Analysis of shear wall structures of variable cross section", The Structural Design of Tall and Special Buildings, 21(1), (2012),1–15.

[26] Son, H.J., Park, J., Kim, H., Lee, H.Y., Kim ,D.J. "Generalized finite element analysis of high-rise wall-frame structural systems", Engineering Computations, 34(1), (2017)

[27] StaffordSmith B., Kuster M., Hoenderkainp C. D., "Generalized method for estimating drift in high-rise structures", Journal of Structural Engineering, ASCE, 110(7), (1984), 1549–1562.

[28] Heidebrecht A. C., Rutenberg A., "Applications of drift spectra in seismic design", Proceedings of 12WCEE, Auckland, NZ, New Zealand Society for Earthquake Engineering, (2000), Paper No. 209.

[29] Xie, J., Wen, Z., "A measure of drift demand for earthquake ground motions based on Timoshenko beam mode", The 14th World Conference on Earthquake Engineering. Beijing, China, (2008)

[30] Khaloo A.R., Khosravi, H., "Multi-mode response of shear and flexural buildings to pulse-type ground motions in near-field earthquakes", Journal of Earthquake Engineering, 12(4), (2008), 616–630.

[31] Yang D., Pan J., Li ,G., "Interstory drift ratio of building structures subjected to near-fault ground motions based on generalized drift spectral analysis", Soil Dynamics and Earthquake Engineering, 30(11), (2010),1182–1197.

[32] Shodja, A. H., Rofooei, F. R., "Using a lumped mass, nonuniform stiffness beam model to obtain the interstory drift spectra", Journal of Structural Engineering ASCE, 140(5), (2014)

[33] Tekeli ,H., Atimtay, E., Turkmen M., "An approximation method for design applications related to sway in RC framed buildings", International Journal of Civil Engineering Transaction A: Civil Engineering, 13(3), (2015), 321-330.

[34] Zalka, K. A., "A simplified method for calculation of natural frequencies of wall-frame buildings", Eng. Struct., 23(12), (2001, 1544-1555

[35] Zalka, K.A., "Maximum deflection of symmetric wall-frame buildings", Peri-odica Polytechnica, Civil Engineering, 57(2), (2013), 173–184

[36] Bilyap S., "Betonarme yüksek yapılarda perde çerçeve sistemlerinin yatay kuvvetlere göre hesabı", Ege Üniversitesi Matbaası, İzmir, 1979.

[37] Ertutar Y., Betonarme yüksek yapılarda yatay yük etkisi, Dokuz Eylül Üniversitesi Yayınları, İzmir, 1995.

[38] Ertutar Y., , Yatay kuvvetler etkisindeki perde-çerçeve sistemlerinin burulmalı çözümü, Yeni Deprem Yönetmeliği ve Uygulama Sorunları Sempozyumu Bildiriler Kitabı, İzmir, (1997), 33-39.

[39] Çelebi Ü., Bilyap S., "Burulmalı Perde-Çerçeve sistemlerinin hesabında sürekli burulma çubuğu analojisi yöntemi", Türkiye İnşaat Mühendisliği 11. Teknik Kongresi Bildiriler Kitabı Cilt 1, 8-11 Ekim, İstanbul, (1991), 62-73.

[40] Alku Ö.Z., "Kademeli veya Kesik Perdeler İçeren Binaların Yatay Kuvvetler Etkisinde Yaklaşık Hesabı", Deprem Araştırma Bülteni, Cilt 13, Sayı 53, (1986), 5-31.

[41] Ertutar Y., "Yatay Yüklerin Etkisi Altında Bulunan ve Çerçeve Kayma Rijitliği Yapı Yüksekliğince Nonlineer Değişen Yapılarda Yatay Yer değiştirmelerin Hesabı", Deprem Araştırma Bülteni, Cilt 14,Sayı 57, (1987), 83-92.

[42] Alku Ö.Z., Ertutar Y., "Mafsallı Bağlantı Kirişli Bir Açıklıklı Birleşik Çerçevenin Kayma Rijitliği", Deprem Araştırma Bülteni, Cilt 16, Sayı 66, (1989), 90-100.

MANAS Journal of Engineering
ISSN 1694-7398 | e-ISSN 1694-7398

Volume 11, Issue 2, (2023) Pages 176-189
https://doi.org/10.51354/mjen.1260477

Preconcentration and determination of Cu(II) and Cd(II) ions from wastewaters by using hazelnut shell biosorbent immobilized on Amberlite XAD-4 resin

İbrahim Teğin[1], Selma Akdeniz[1], İhsan Alacabey[2], Kadir Erol[3,*], Orhan Acar[4]

[1] Siirt University, Arts and Science Faculty Department of Chemistry, Siirt, TURKEY, ibrahim.tegin@siirt.edu.tr, ORCID: 0000-0002-5661-7195, akdeniz73562@hotmail.com, ORCID: 0009-0007-6865-8203
[2] Mardin Artuklu University, Vocational School of Health Services, Department of Medical Services and Techniques, Mardin, TURKEY, ihsanalacabey@hotmail.com, ORCID: 0000-0002-3080-2296
[3] Hitit University, Vocational School of Health Services, Department of Medical Services and Techniques, Çorum, TURKEY, kadirerol86@gmail.com, ORCID: 0000-0001-9158-6091
[4] Gazi University, Science Faculty, Department of Chemistry, Ankara, TURKEY, oacar@gazi.edu.tr, ORCID: 0000-0002-0969-2627

ABSTRACT

Hazelnut shell biosorbent immobilized on Amberlite XAD-4 polymer resin as solid phase extraction method was developed and used for preconcentration of Cu(II) and Cd(II) ions from aqueous solutions. Concentrations of analytes in solutions were determined by Flame Atomic Absorption Spectrometry after extraction with column technique. Functional groups of nutshell biosorbent immobilized on resin were characterized by Fourier transform infrared spectrometry. Optimized critical parameters for preconcentration of Cu^{2+} and Cd^{2+} ions from sample solutions with nutshell immobilized on the resin were the pH value of solution, type of eluent solutions, the flow rate of sample solution, quantities of nutshell biosorbent, Amberlite XAD-4 resin, and enrichment factors, respectively. Detection limits of Cu^{2+} and Cd^{2+} ions found were 0.29 µg L^{-1} and 0.25 µg L^{-1}, respectively. The method proposed was applied for determinations of Cu^{2+} and Cd^{2+} ions in standard reference material (BCR-670 aquatic plant sample) for accuracy and applied to real water samples such as wastewater and Van lake water. At the 95% confidence level, relative standard deviations (RSDs) were found as 1.44% for Cd^{2+} and 1.21% for Cu^{2+} ions with three replicate measurements.

ARTICLE INFO

Research article

Received: 5.03.2023
Accepted: 16.05.2023

Keywords:
amberlite XAD-4,
hazelnut shell,
preconcentration,
trace element,
wastewater

**Corresponding author*

1. Introduction

Nowadays, toxic metal contaminations and their effects have widely increased in the environment and waters because of rapid developments in technology, industry, and social life of the people in the world [1-6]. Copper is one of the trace elements found in the body, but its higher level can cause toxic like other metals such as cadmium and lead, even if at low concentrations [7, 8]. Daily intake of copper is 1.0–1.1 mg for an adult woman and 1.2-1.6 mg for an adult man. Excessive or deficient copper causes different health problems such as heart failure, nausea, anaemia, hypertension, and vomiting [9]. Besides, cadmium accumulates in the human body and may increase the risk of lung cancer [10, 11]. Copper and cadmium are widely used in technology such as electrical supplies for construction, heat exchangers, electroplating, electroplate steel, medicine, painting, dying, surface treatment, etc. [12, 13]. For example, some industrial products that included cadmium are power stations, Ni-Cd batteries, alloy manufacture, dyeing, etc. Especially from industrial and agricultural activities, mining, unplanned urbanization, and household wastes, trace levels of copper and cadmium are emitted into the environment and accumulate in nature [14]. These problems have threatened the health of living beings in ecological nature and will affect future generations. Removing these metal contaminations from water solutions is a significant environmental problem because of their toxic effects on living conditions [15]. Therefore, determinations of copper and cadmium contaminants are important in waters because of their poisonous impacts on human health [16, 17].

Traditional methods such as chemical precipitation, ion flotation, ion exchange, coagulation and electrochemical methods have been applied to remove industrial pollution in wastewater in the field of environmental health [18, 19].

These methods are considered economically inexpensive, but they all have some disadvantages and inadequacies in environmental pollution removal. There is always a need for cheaper and more effective solutions. For this, it is seen that the adsorption method using biosorbent gives remarkable results [20-23]. Especially the use of waste materials as an adsorbent in adsorption processes is widespread for the synthesis of cost-effective materials. The peels of herbal products are very sympathetic to scientists within the framework of green chemistry thought [24-26].

In recent years, chelating resins have been functionalized in several assistance materials. The inclusion of commercially available XAD resins and their usage has increased for removing and recovering metals contaminated [27, 28]. Amberlite XAD resins are broadly used to develop chelating materials for preconcentration and enrichment procedures due to their excellent physical and chemical properties such as porosity, high surface area, durability, and purity [29]. Among these resins, Amberlite XAD-4 used as a solid sorbent has perfect physical features such as resistance to acids, bases, oxidizing and reducing agents, large surface area (>750 m^2g^{-1}), well-characterized medium size (0.49– 0.69 mm), and porosity [30].

The solid phase extraction (SPE) method is one of the most commonly used techniques for the preconcentration and enrichment of metals. It provides more elastic study conditions and well selectivity, steady, proximity, ability to work with large sample volume, high concentration capacity and high enrichment capability for metal ions, safety for hazardous samples, and minimum costs due to low consumption of reagents, ease and fast for automation [2, 10, 31, 32]. The fundamental mechanism of SPE is a transference of metals from the aqueous phase into active regions of the solid phase [29, 33].

Various Amberlite XAD resins and biological materials have been used as SPE for trace levels of toxic metals in water samples before instrumental analysis [34, 35]. The usage of natural materials such as yeast, plant leaves, and root tissues for recovery of heavy and toxic metal ions from aqueous solutions has increased in recent years because of the preferable performance and minimum cost of biosorbent materials. Biosorption processes are usually fast and appropriate for the extraction of metals from large volumes of water samples [36, 37]. Biological sorbent materials immobilized on a suitable XAD resin have been used to overcome some problems by offering ideal size, mechanical force, hardness, and porous characteristics to the biological material [35, 38, 39].

In this study, hazelnut shell biosorbent immobilized on Amberlite XAD-4 resin for SPE procedure was developed for preconcentration, enrichment, and determination of Cu^{2+} and Cd^{2+} ions in waters. There was no study observed in the literature with this procedure. The recovery conditions for Cu^{2+} and Cd^{2+} ions using resin immobilized with hazelnut shell as biosorbent in column technique were investigated. Effects of critical parameters such as pH of the solution, eluent type and concentration, solution flow rate, solution volume, foreign ion effects, and column reproducibility were examined in detail to optimize recovery and enrichment conditions for Cu^{2+} and Cd^{2+} ions by using standard solutions. The method proposed was applied to standard reference material (BCR-670 Aquatic plant sample) and real water samples to preconcentrate Cu^{2+} and Cd^{2+} ions, and the ions were determined by Flame Atomic Absorption Spectrometry (FAAS).

2. Materials and methods

2.1. Equipment and working conditions

A Perkin Elmer 700 Analyst model flame atomic absorption spectrometry (Shelton, CT, USA) equipped with a deuterium lamp for background correction was used for absorbance measurements of Cu and Cd in solutions. Operating conditions of Cd and Cu were wavelengths (228.8 and 324.8 nm), bandpasses (0.7 and 0.5 nm), acetylene flow rates (1.8 and 2.0 L min^{-1}), and lamp currents (10.0 and 4.0 mA), respectively, and they were set according to the recommendations of the manufacturer. A Hanna model pH meter (Hanna Instruments, HI 2211 pH/ORP Meter, Romania) equipped with a glass electrode was performed to measure the pH values of all sample solutions. Extraction columns (1.0 cm inner diameter, 10.0 cm length, and 100 mL reservoir at upper end) equipped with polypropylene frites were utilized. A Watson Marlow 120 S brand (Milford, MA) peristaltic pump was utilized to pass solutions through a column and to control the flow rate. A Perkin Elmer 100 model Fourier transform infrared (FT-IR) spectrometer was utilized to analyse filler material to determine functional groups of nutshell immobilized Amberlite XAD-4 resin. Scanning electron microscopy (SEM) images were obtained with a LEO 440 Model Instrument to investigate surface structure. All chemicals and reagents (Merck, Germany) used during the experiments were analytical grade and utilized without purification. During the studies, ultrapure water obtained from a water system (resistivity 18.3 MΩ cm, Human power I+, Human Corporation, Korea) was used. Working standard solutions of Cd^{2+} and Cu^{2+} ions were prepared by diluting atomic absorption standard stock solutions (Merck, Germany, 1000 mg L^{-1} of each).

Glassware and plastic materials utilized in the works were cleaned by using 10% HNO_3 solution, rinsed three times with ultrapure water and dried in an oven at 110°C for use.

2.2. Collection and preparation of samples

Standard reference material (SRM, BCR-670 Aquatic plant sample) taken from Institute for Reference Materials and

Measurements (European Commission, Joint Research Centre) was decomposed by utilizing Berghof Speed Wave (MWS-3) microwave oven digestion system. The 0.50 g of SRM was weighed into a polytetrafluoroethylene (PTFE) digestion vessel. 5 mL of HNO_3 (65%, m/m) and 2 mL of H_2O_2 (30%, m/m) were poured into the vessel and waited for one night at laboratory condition by closing with a cover. The operating states of the digestion system in two steps were used as temperature (from 140 to 195 °C); pressure (50 to 50 bar); power (from 60 to 90 %); T_a (from 5 to 1 min) and time (10 to 10 min). After decomposition, the solution was diluted to 50 mL with ultrapure water. Water samples were collected from Siirt city waste and tap waters, from Van Lake water, Tuzkuyusu saline water, and Billoris spa water. The samples in 1.0 L polypropylene bottles were acidified with 0.1 mol L^{-1} HNO_3 to avoid the adsorption of ions on the walls of the container. In addition, the samples were filtered through ordinary filter paper to remove thick and suspended particles.

2.3. Preparation of Amberlite XAD-4 resin and nutshells

Approximately 50 g of Amberlite XAD-4 polymer resin (polystyrene divinylbenzene, taken from Sigma Aldrich) was mixed with 4 M HCl to modify its structure and remove organic and inorganic impurities. It was washed with ultrapure water until reaching neutral pH (pH was about 7.0) and put into an ethanol-water mixture (1:1) solution, respectively. After washing with ultrapure water, the resin was dried at 105°C and kept in a polyethylene bottle [29, 40]. Nutshells taken from Siirt bazaar were grained by Memert brand mill. After passing through a 60 mesh sieve, they were cleaned with ultrapure water to take out impurities and dried in an oven at 80°C. They were passed through 60 mesh sieves again to obtain powder nutshells [41].

2.4. Preparation of SPE columns for sorption studies

Amberlite XAD-4 resin (1.00 g) and nutshell powder (0.30 g) were mixed with a magnetic stirrer (IKA Werke RT-10P, Germany) for 1 h by adding 15 mL of ultrapure water. After mixing, the solid mixture was dried in an oven at 105°C for 1 h, passed through a 60 mesh sieve, and put into a column having a porous disk and a stopcock to prepare SPE columns [9]. The ultrapure column was conditioned by passing 1.0 mol L^{-1} HCl. 50.0 mL of two test solutions including 2.0 µg mL^{-1} of Cd^{2+} or 2.0 µg mL^{-1} of Cu^{2+} ions were separately prepared from standard stock solutions. Although FAAS could directly determine concentrations of these elements, they were used only to obtain optimization parameters [42]. The pH of each test solution was adjusted to a suitable value and passed from the SPE column by utilizing a peristaltic pump with an adjusted flow rate, and about 15 mL of ultrapure water was spent through the column. Cd^{2+} or Cu^{2+} ions taken by nutshells immobilized on the resin were eluted from two different columns with 5.0 mL of 1.0 mol L^{-1} HCl or 5.0 mL of 1.0 mol L^{-1} HNO_3 solution, separately. FAAS, respectively measured concentrations of Cu^{2+} and Cd^{2+} ions in eluent solutions [40].

3. Results and discussion

3.1. Characterization studies of filler material

The morphology and functional groups of a hazelnut shell, Amberlite XAD-4, and hazelnut shell immobilized on Amberlite XAD-4 resin were researched between 4000 and 400 cm^{-1} by FT-IR spectrometry and results of filler materials taken were shown in Figure 1. As seen in Figure 1, a series of absorption peaks were shown that the column packing material structure is complex. All spectra analyzed have bands at 3300-3500 cm^{-1}, indicating the presence of an alcoholic, phenolic, or acidic OH bond. The broad peak at 3394-3384 cm^{-1} indicates that macromolecular linkage has attached hydroxyl groups (cellulose, pectin, etc.). The peak points observed at 2923 and 2911 cm^{-1} may belong to C-H groups. At 2301-2068 cm^{-1}, the triple bond attached to the group C-N may be picked. The bands around the 1603 - 1601 cm^{-1} were indicated the presence of free and esterified carboxyl groups. FT-IR spectra showed that the carbon bands at 1484 and 1430 cm^{-1} were aliphatic, aromatic, and cyclic with different surface structures. Besides, the bands at 1023 and 981 cm^{-1} indicated that the alcohols and carboxylic acids were C-O [43].

By taking scanning electron microscopes (SEMs) of Amberlite XAD-4 alone, hazelnut shell immobilized on resin, Cu^{2+} and Cd^{2+} ions pasted state of hazelnut shell immobilized resin were performed to examine their surfaces with LEO 440 Computer Controlled Digital Model Instrument, separately and the results obtained were shown in Figure 2. In addition, the Energy Dispersive X-Ray Analysis (EDX) image and thermo-gravimetric analysis (TG/DTA) graph of hazelnut shell immobilized on Amberlite XAD-4 resin were shown in Figures 3a and 3b. As shown in Figure 3a, no Cu and Cd contamination is observed in the column filler material. When Figure 3b was examined, the TGA chart could be viewed in 4 steps. In the first step, there was no mass loss between 68 and 225°C. In the second step, a mass loss of 19.3% was observed between 225 and 404°C. In the next step, 79.0% mass loss appeared between 405 and 479°C. In the final step, there was about 92.4% mass loss observed between 478 and 1006°C. It was also found that the decomposition temperature of column packing material was about 455°C from the derivative weight (mass %/min) analysis.

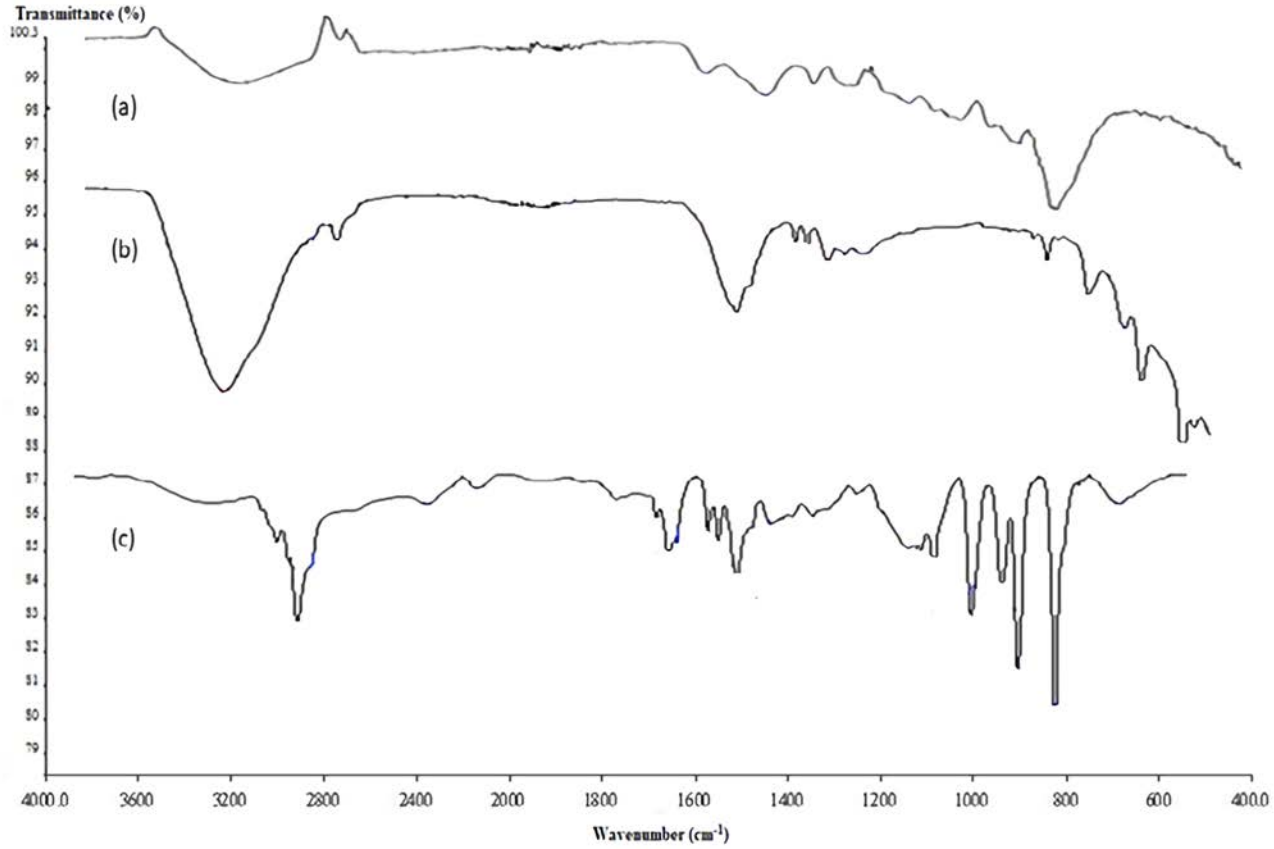

Figure 1. *Comparison of FT-IR images of (a) Hazelnut shell, (b) Amberlite XAD-4 and (c) Hazelnut shell immobilized on Amberlite XAD-4.*

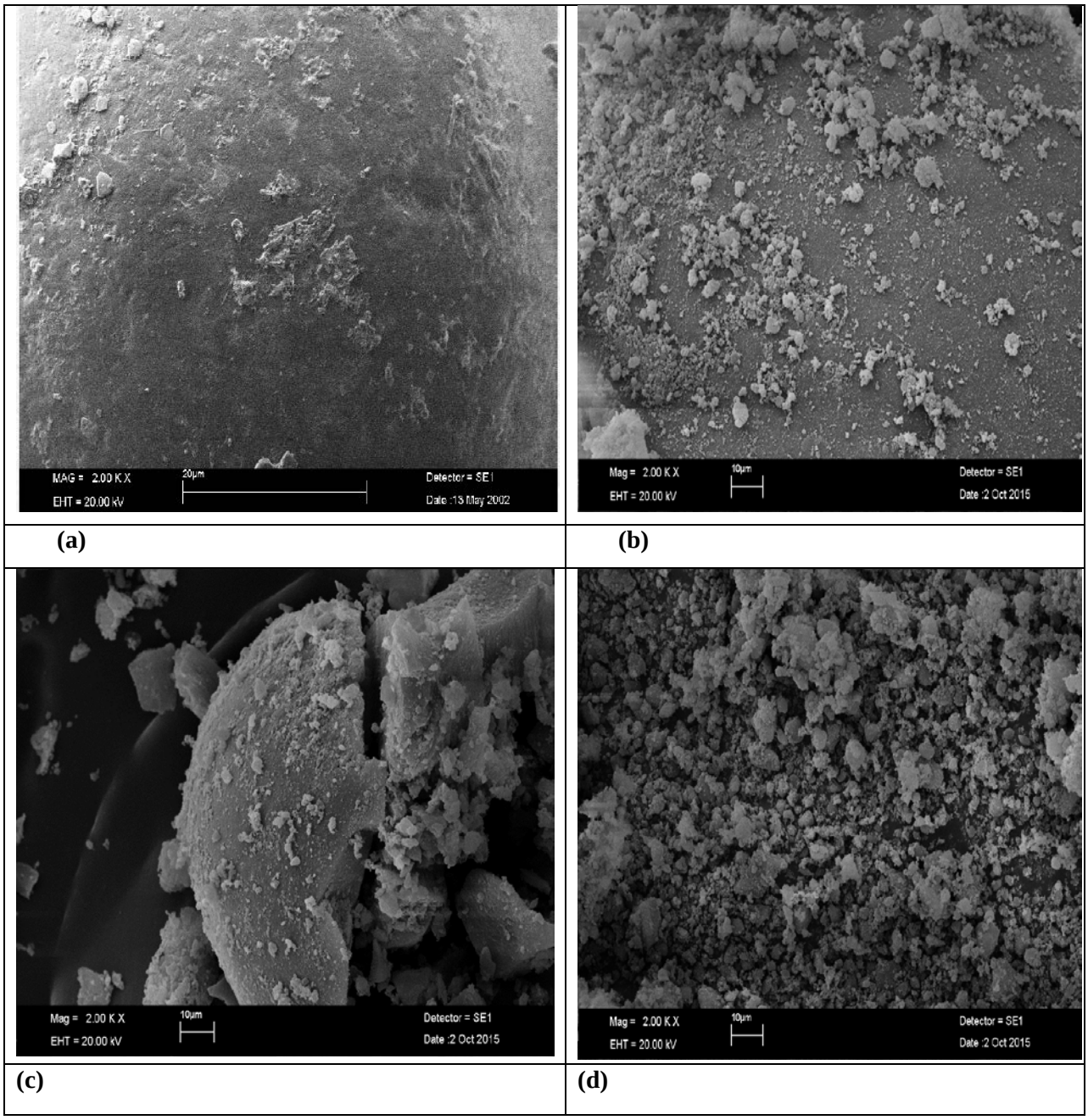

Figure 2. *Comparison of SEM images of (a) Amberlite XAD-4 [43], (b) Hazelnut shell immobilized on Amberlite XAD-4, (c) Cu^{2+} pasted state of hazelnut shell immobilized on Amberlite XAD-4 and (d) Cd^{2+} pasted state of hazelnut shell immobilized on Amberlite XAD-4.*

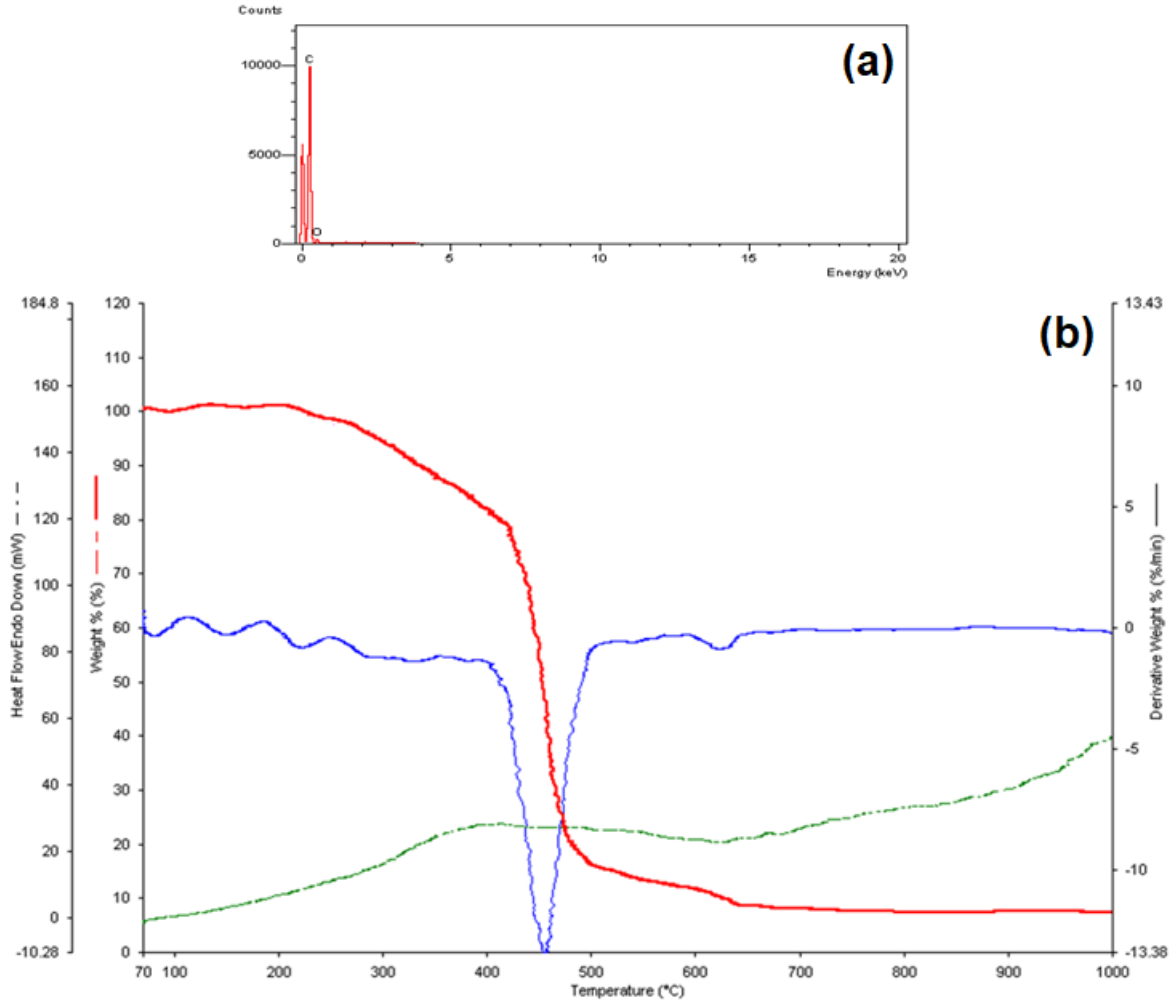

Figure 3. *(a) EDX graph of hazelnut shell immobilized on Amberlite XAD-4 column filler material, (b) TGA graph of hazelnut shell immobilized on Amberlite XAD-4 column filler material.*

3.2. Effect of pH

The pH effect is an important test parameter for the adsorption of metal ions because it affects solubility and ionic attraction of metal ions with functional groups of Amberlite XAD-4 resin immobilized with hazelnut shell sorbent [29]. The pH effect of sample solutions on recoveries of Cu^{2+} and Cd^{2+} ions in hazelnut shells immobilized on the resin was investigated in the pH range from 3.0 to 10.0 by using 1 mol L^{-1} HCl solution or 1 mol L^{-1} NaOH solution. The solutions prepared were passed through the column, and they were eluted by HCl solution or HNO_3 solution. For this purpose, extraction experiments from the column were carried out by utilizing 50.0 mL of test solutions containing 2.0 µg mL^{-1} Cu^{2+} and 2.0 µg mL^{-1} Cd^{2+} ions. Percent recoveries of Cu^{2+} and Cd^{2+} ions versus pH values of solutions for the SPE process were depicted in Figure 4a. As seen in Figure 4a, optimum pH values of solutions were found as 7.0 for Cu^{2+} and 9.0 for Cd^{2+} ions. At these pH values, average percent recoveries of Cu and Cd for three replicate measurements with standard deviations (below 2%) were found as 64.7 ± 1.3% and 76.7 ± 1.8%, respectively. The recovery efficiency for both analytes between pH 3.0 and 5.0 was low due to the acidic medium of the solution. All following solutions were regulated to pH 7.0 for Cu^{2+} and to pH 9.0 for Cd^{2+} ions. The Cu^{2+} and Cd^{2+} ions in eluent solutions were determined by FAAS.

3.3. Effect of solution flow rate

The flow rate effect of the sample solution was investigated to obtain the optimum retention of analytes in Amberlite XAD-4 immobilized with hazelnut shells. Transfer of ions from sample solution into active sides or binding groups of biosorbent could be influenced by the flow rate of sample solution and must be controlled for biosorption recovery.

Therefore, the effect of the flow rate of a sample solution containing only Cu^{2+} at pH 7.0 and another solution containing only Cd^{2+} at pH 9.0 on the recoveries of analytes with the resin immobilized nutshell powder as biosorbent was examined in the range from 1.0 to 6.0 mL min^{-1} by using a peristaltic pump. Average recovery results of Cu^{2+} and Cd^{2+} ions with three replicate measurements found versus flow rate of solution were shown in Figure 4b. As shown in Figure 4b, optimum flow rates of sample solutions were found as 1.8 mL min^{-1} for Cu^{2+} and 2.7 mL min^{-1} for Cd^{2+} ions. Means of Cu^{2+} and Cd^{2+} ions recoveries at these flow rates were found to be 64.7 ± 1.5% and 100.0 ± 1.7%, respectively. When the flow rate of solution was increased above 2 mL min^{-1}, percent recovery of Cu^{2+} ions on biosorbent decreased significantly. This decrease may be due to the less interaction of the analyte with the sorbent species. Percent recovery of Cd^{2+} ions reached a plateau at 2.7 mL min^{-1} and stable by increasing flow rates. These optimized flow rates of sample solutions containing analytes were performed in the following studies.

3.4. Effect of amount of nutshell and resin

The amount of column supporting material is an essential parameter for quantitative recovery of metals in SPE studies. Increasing the mass of biosorbent or mass of resin, percent recoveries of metals can rise to an optimum value because active surfaces and binding groups for biosorption of heavy and toxic metals increase. If biosorbent mass or resin mass was increased over optimum mass, interference between active sides and binding groups could occur, and recovery of metals could reduce [44]. An example of the nutshell as biosorbent for Cu^{2+} and Cd^{2+} ions was examined using optimized sample solutions' optimised individual flow rates and pH values, respectively. The amount of hazelnut shells varied from 0.15 to 0.45 g, while the quantity of Amberlite XAD-4 resin was kept constant as 1.0 g during experimental studies. The means of percent recovery results of Cu^{2+} and Cd^{2+} ions for three replicate measurements with standard deviations (less than 3%) found versus to mass of biosorbent were depicted in Figure 4c. As seen in Figure 4c, recovery values of Cu^{2+} and Cd^{2+} ions increased by the increasing amount of nutshell powder up to 0.3 g and then reached a constant value above this amount. Therefore, 0.3 g of hazelnut shell was adequate for both Cu^{2+} and Cd^{2+} ions. The averages of percent recoveries for Cu^{2+} and Cd^{2+} ions were found as 98.9 ± 1.6% and 99.0 ± 1.9%, respectively.

Effect of Amberlite XAD-4 resin mass on recoveries of Cu^{2+} and Cd^{2+} ions was also examined in the range of 0.25–1.50 g while the mass of nutshell biosorbent was kept constant as 0.3 g during studies. Means of percent recoveries of ions for three replicate measurements with standard deviations (less than 3%) obtained versus the resin mass were shown in Figure 4d. As seen in Figure 4d, maximum percent recoveries (above 90%) were found using 1.0 g resin for both Cu^{2+} and Cd^{2+} ions. When above 1.0 g of resin was used, percent recoveries of Cu^{2+} and Cd^{2+} ions decreased. Therefore, 0.3 g of hazelnut shell powder and 1.0 g of resin optimized were mixed and used for further studies.

3.5. Effect of sample volume

The effect of sample volume is another critical parameter for obtaining reliable analytical results and high enrichment factors (EFs). Since natural waters especially contain trace metal ions, the highest volume of sample solution must be passed through SPE systems under optimum conditions [10, 29, 35]. Volume effect of sample solution on recoveries of Cu^{2+} and Cd^{2+} ions in nutshells immobilized on Amberlite XAD-4 resin was examined in the range of 25.0-400.0 mL solutions containing 2.0 µg mL^{-1} Cu^{2+} and Cd^{2+} ions by passing through SPE column under optimized experimental conditions. Means of recoveries of Cu^{2+} and Cd^{2+} ions found from three replicate measurements with standard deviations (less than 3%) versus volume of sample solution were shown in Figure 4e. As seen in Figure 4e, the averages of recoveries for Cu^{2+} and Cd^{2+} ions were found as 99.0 ± 1.8% and 98.3 ± 2.3%, respectively. When the sample volume was increased above 50 mL, recoveries of metal ions decreased slowly and constantly. It was observed that 50 mL sample solution was adequate for the preconcentration of Cu^{2+} and Cd^{2+} ions at optimized conditions for the next studies.

3.6. Reusability of SPE column

Reusability and cost of column workings in SPE are important for column stability in biosorption studies. The stability of the column was tested by using a 50.0 mL sample solution containing 2.0 µg mL^{-1} Cu^{2+} and Cd^{2+} ions. Cu^{2+} and Cd^{2+} ions retained on the sorbents were eluted with 5.0 mL of HNO_3 (1.0 mol L^{-1}) solution for Cu^{2+} and 5.0 mL of HCl (0.5 mol L^{-1}) solution for Cd^{2+} ions. If concentrations of ions were out of the calibration range, they were diluted with ultrapure water to measurable concentrations and analyzed by FAAS. Column reusability studied was shown in Figure 4f. As seen in the figure, the average percent recovery was higher than 85% for nearly 10 cycles. The column could be reused for 10 cycles sufficiently without reducing the retentions of Cu^{2+} and Cd^{2+} ions in column stability.

3.7. Effect of type, concentration and volume of eluent

The type, concentration and volume of eluent were investigated for reusability of nutshells biosorbent immobilized on Amberlite XAD-4 resin by minimizing damage and retention of metals [10, 29, 35, 45]. A suitable eluent was carried out to obtain a high EF for Cu^{2+} and Cd^{2+} ions from the SPE column. HCl and HNO_3 elution solutions were tested for desorption of Cu^{2+} and Cd^{2+} ions from biosorbent and resin at various volumes and concentrations. The averages of recovery results obtained with standard deviations (less than 2.5%) for three replicate measurements were given in Table 1. As seen in Table 1, when 5.0 mL of 1.0 mol L^{-1} HNO_3 eluent was used for Cu^{2+} ion, the percent

recovery value found was about 96.5 ± 1.8%, and when 5.0 mL of 0.5 mol L^{-1} HCl eluent was used for Cd^{2+} ion, the percent recovery value was found as 94.2 ± 1.9%. Therefore, 5.0 mL of 1.0 mol L^{-1} HNO_3 for Cu^{2+} ion and 5.0 mL of 0.5 mol L^{-1} HCl for Cd^{2+} ion were suitable for studies. The EF for both analytes was found as 10 (50 mL sample/5 mL eluent). As result, we can say that the Cu^{2+} and Cd^{2+} ions in water samples can be directly determined at low concentrations using the method proposed and FAAS.

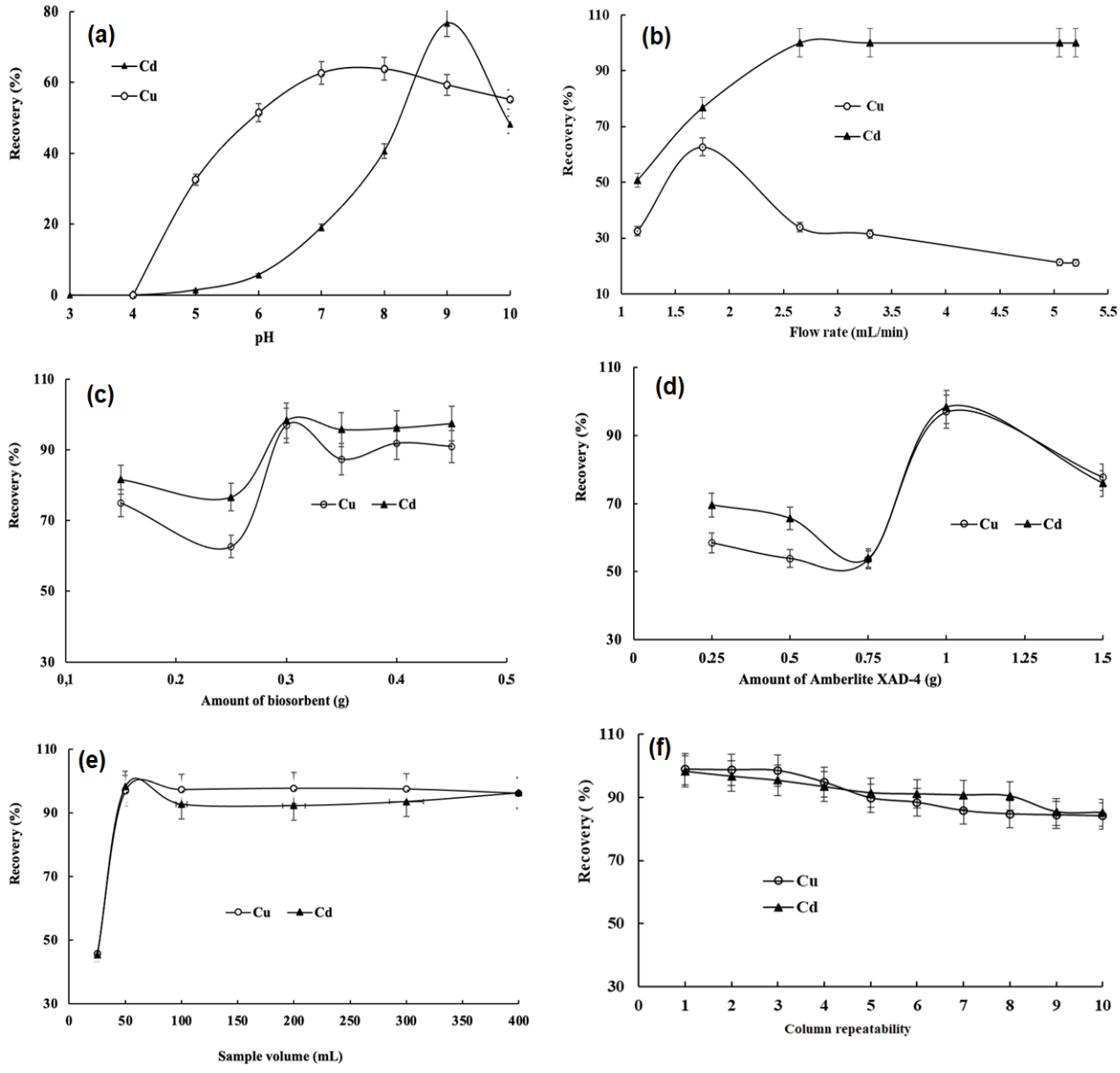

Figure 4. *(a) Recoveries of Cu^{2+} and Cd^{2+} ions with various pH of solutions, (b) Recoveries of Cu^{2+} and Cd^{2+} ions with various flow rates of a solution, (c) Effect of amount of hazelnut shell biosorbent for recoveries Cu^{2+} and Cd^{2+} ions by using 1.0 g of XAD-4, (d) Effect of Amberlite XAD-4 quantity for recoveries of Cu^{2+} and Cd^{2+} ions by using 0.3 g of hazelnut shell biosorbent, (e) Recoveries of Cu^{2+} and Cd^{2+} ions with various volume of sample solution, (f) Stability and reusability of the column with hazelnut shell immobilized on Amberlite XAD-4 for recoveries of Cu^{2+} and Cd^{2+} ions.*

.

Table 1. *Optimization of type and volume of eluent solution for recoveries of Cu^{2+} and Cd^{2+} ions (N=3).*

Eluent type	Concentration (mol L^{-1})	Eluent Volume (mL)	Recovery (%)[a]	
			Cu^{2+}	Cd^{2+}
HCl	0.5	5	90.8 ± 1.7	94.2 ± 1.9
	1.0	5	87.9 ± 2.1	88.6 ± 2.0
	1.5	5	88.3 ± 1.9	88.5 ± 2.3
	2.0	5	87.6 ± 2.0	88.2 ± 2.1
HNO_3	0.5	5	90.8 ± 2.1	89.3 ± 1.8
	1.0	5	96.5 ± 1.8	80.5 ± 2.0
	1.5	5	93.7 ± 2.2	80.2 ± 2.3
	2.0	5	93.0 ± 2.0	80.1 ± 2.2

[a] 95% confidence level, N= 3, $\overline{x} \pm 4.30 \cdot s/\sqrt{N}$

3.8. Influence of interfering ions on recovery of metals

Due to foreign ions' matrix effects, the determination of trace levels of Cu^{2+} and Cd^{2+} ions in real water samples by FAAS is complicated [10, 46]. The effects of interfering ions on the determination of the analytes were studied by using optimized conditions obtained. Different interfering cations and anions such as Na^+, K^+, Mg^{2+}, Ca^{2+}, Cl^-, $SO4^{2-}$ and F^- were added to 50 mL test solution containing 2.0 µg mL^{-1} of Cu^{2+} and Cd^{2+} ions. Means of percent recovery results found from three replicate measurements with standard deviations (about 2%) by using FAAS were summarized in Table 2. As seen in Table 2, the average percent recoveries of analytes were generally higher than 80% for Cu^{2+} (except Ca^{2+} ion) and 83% for Cd^{2+} ions, respectively.

Table 2. *Optimization of type and volume of eluent solution for recoveries of Cu^{2+} and Cd^{2+} ions (N=3).*

Ion	Salts added	Interference to metal ion ratio	Recovery[a] (%)	
			Cu^{2+}	Cd^{2+}
Na^+	NaCl	2500	86.3 ± 2.0	97.1 ± 1.1
Cl^-	$BaCl_2$. $2H_2O$	5	81.9 ± 1.9	84.6 ± 1.5
SO_4^{2-}	$MnSO_4.H_2O$	12.5	86.2 ± 1.8	93.1 ± 1.6
Mg^{2+}	$Mg(NO_3)_2.6\ H_2O$	1250	82.9 ± 1.7	84.1 ± 1.8
Ca^{2+}	$CaCl_2.2H_2O$	750	72.4 ± 1.5	83.7 ± 1.7
F^-	KF	250	100 ± 1.0	90.2 ± 1.9

[a] 95% confidence level, N= 3, $\overline{x} \pm 4.30 \cdot s/\sqrt{N}$

3.9. Analytical features and applicability

Under optimized experimental conditions, the analytical features of the method proposed were performed and assessed. Analytical parameters obtained for Cd^{2+} and Cu^{2+} with the method developed were given in Table 3. By applying to

preconcentrated blank solutions, limits of detection (LOD) and quantification (LOQ) values for Cu^{2+} and Cd^{2+} ions were determined. The LODs for Cu^{2+} and Cd^{2+} ions were depended on the ratio of three times standard deviations of absorbance signals for the blank solution to the slope of the calibration curve (LOD = $3x(S_b/m)$, N=12). After dividing the EF, the analytical LODs for Cu^{2+} and Cd^{2+} ions were found as 0.29 µg L^{-1} and 0.25 µg L^{-1}. Moreover, the LOQ values (LOQ = $10x(S_b/m)$, N=12) for Cu^{2+} and Cd^{2+} ions from related calibration curves were also found as 0.97 µg L^{-1} and 0.83 µg L^{-1}, respectively.

Table 3. *Analytical parameters of metals studied by FAAS with proposed method.*

Analytical Parameter	**Cd^{2+}**	**Cu^{2+}**
LOD (µg L^{-1})	0.25	0.29
LOQ (µg L^{-1})	0.83	0.97
Linear range (mg/L)	0.002 – 8.0	0.002 - 5.8
Regression equation	A = 0.1841 x C + 0.0023	A = 0.1339 x C + 0.0119
R^2	0.9975	0.9998

A = Absorbance, C = Concentration

The precision of the proposed method was tested by using 50 mL of a standard solution containing 2.0 µg mL^{-1} Cu^{2+} and Cd^{2+} ions. Means of recovery results obtained at 95% confidence level (N = 3) were given in Table 4. Relative standard deviations (RSDs) were found as 1.44% for Cu^{2+} and 1.21% for Cd^{2+} ions. Regression coefficients (R^2) were determined as 0.9998 and 0.9975 for Cu^{2+} and Cd^{2+} ions (Table 3), respectively.

To evaluate the accuracy of the method proposed, Cu^{2+} and Cd^{2+} ions in the certified BCR-670 aquatic plant sample (SRM) were determined under optimized conditions. The means of results found were illustrated in Table 4, and they were well consistent with certified values of SRM.

Table 4. *Precision and applicability of method proposed to SRM (BCR-670 Aquatic plant sample).*

Element	**Precision**		**BCR-670 aquatic plant sample**		
	$R\pm4.30\cdot s/\sqrt{N}$ (%)	**RSD (%)**	**Certified value (µg/kg)**	**Found (µg/kg)[a]**	**Relative error (%)**
Cd^{2+}	98.3 ± 0.8	1.44	75.5 ± 2.5	74.2 ± 1.6	-1.72
Cu^{2+}	99.0 ± 0.2	1.21	1820 ± 300	1890 ± 214	3.85

[a] 95% confidence level, N= 3, $\overline{x} \pm 4.30\cdot s/\sqrt{N}$

Comparison of analytical characteristics of the method proposed with the recent methods developed for preconcentration of Cu^{2+} and Cd^{2+} ions with different instruments were illustrated in Table 5. It was clear that detection limits (LODs) and RSDs of Cu^{2+} and Cd^{2+} were compatible with the literature [47]. Besides, EFs found in this study were lower than the literature values [38, 39, 48, 49]. Because of this, the method proposed can be applied for the determination of trace levels of Cu^{2+} and Cd^{2+} ions in various samples.

Table 5. *Comparison of Analytical Features of Pre-concentration Methods for Cu^{2+} and Cd^{2+} ions.*

Method	Instrument	Cu^{2+}			Cd^{2+}			Reference
		LOD (µg L^{-1})	EFs	RSD (%)	LOD (µg L^{-1})	EFs	RSD (%)	
Synthesized 8-hydroxy-2-quinoline carboxy-aldehyde functionalized Amberlite XAD-4	FAAS	0.35	22.3	-	0.14	27.6	-	[48]
Mucor pusillus immobilized Amberlite XAD- 4 biocomposites	HR-CS FAAS	74	50	<8	62	50	<8	[39]
Synthesis and application of a new functionalized resin for use in an on-line, SPE system	FAAS	0.29	27.3	-	0.13	27.6	-	[49]
Preconcentration and determination of trace elements with 2,6-diacetylpyridine functionalized Amberlite XAD-4	FI-ICP-MS	0.34	-	1.2–8.5	0.33	-	1.2–8.5	[47]
	FI-FAAS	10			22			
Bacillus subtilis – immobilized amberlite XAD-16	ICP-OES	0.21	36.4	4.9	-	-	-	[38]
Nutshell biosorbent immobilized on amberlite XAD-4	FAAS	0.29	10	1.44	0.25	10	1.21	This study

The method proposed was also applied to the determinations of Cu^{2+} and Cd^{2+} ions in actual water samples collected from different regions of Siirt city under optimum conditions. Results of analytes found in samples were demonstrated in Table 6. As seen in Table 6, the proposed method can be successfully applied to actual waters such as waste and tap waters.

Table 6. *Recoveries of metal ions in real water samples by applying the method proposed.*

Samples	Recovery (%)[a]	
	Cu^{2+}	Cd^{2+}
Waste water	99.2 ± 1.2	n.d.
Van lake water	40.1 ± 1.9	n.d.
Tap water	99.6 ± 1.3	n.d
Saline water	46.3 ± 2.0	n.d
Billoris spa water	67.9 ± 1.8	n.d.

[a] 95% confidence level, N= 3, $\overline{x} \pm t \cdot s/\sqrt{N}$, n.d.: Not detected

4. Conclusion

Using hazel nutshell powder as biosorbent immobilized on Amberlite XAD-4 resin, the SPE method was improved for recoveries of Cu^{2+} and Cd^{2+} ions from water solutions. It was discovered that both Cu^{2+} and Cd^{2+} ions were adsorbed by

nutshell immobilized resin in the column at pH values 7.0 for Cu^{2+} and 9.0 for Cd^{2+} ions, respectively. In addition, the experimental parameters such as type and concentration of eluent, solution flow rate, solution volume, foreign ions on the recoveries of Cu^{2+} and Cd^{2+} ions, and column reusability were optimized. The feasibility of the proposed method was

validated by analyzing Cu^{2+} and Cd^{2+} ions in the BCR-670 aquatic plant sample. It was demonstrated that the concentrations of analytes found were in good consistent with certified values. Analytical characteristics of Cu^{2+} and Cd^{2+} ions obtained by the proposed method were compared with literature values and found in good agreement with reported values. The method proposed was applied to the determinations of Cd^{2+} and Cu^{2+} ions in actual water samples. It may be used to determine Cd^{2+} and Cu^{2+} ions in any solutions obtained from various samples in the future. It can be concluded that the method proposed is suitable in terms of simplicity, low analytical cost, sensitivity, precision, accuracy, reliability, and column stability.

References

[1]. Bilgin E., Erol K., Köse K., Köse D. A., "Use of nicotinamide decorated polymeric cryogels as heavy metal sweeper", Environmental Science and Pollution Research, 25(27), (2018), 27614-27627.

[2]. Ozay H., Gungor Z., Yilmaz B., Ilgin P., Ozay O., "Dual use of colorimetric sensor and selective copper removal from aqueous media with novel p(HEMA-co-TACYC) hydrogels: Cyclen derivative as both monomer and crosslinker", Journal of Hazardous Materials, 389, (2020), 121848.

[3]. Kumar M., Pakshirajan K., "Continuous removal and recovery of metals from wastewater using inverse fluidized bed sulfidogenic bioreactor", Journal of Cleaner Production, 284, (2021), 124769.

[4]. Lellala K., "Sulphur Embedded On In-Situ Carbon Nanodisc Decorated On Graphene Sheets For Efficient Photocatalytic Activity And Capacitive Deionization Method For Heavy Metal Removal", Journal of Materials Research and Technology, 13, (2021), 1555-1566.

[5]. Shrestha R., Ban S., Devkota S., Sharma S., Joshi R., Tiwari A. P., Kim H. Y., Joshi M. K., "Technological Trends in Heavy Metals Removal from Industrial Wastewater: A Review", Journal of Environmental Chemical Engineering, 9, (2021), 105688.

[6]. Gürbüz F., Akpınar Ş., Özcan S., Acet, Ö, Odabaşı M., "Reducing arsenic and groundwater contaminants down to safe level for drinking purposes via Fe3+-attached hybrid column", Environmental Monitoring and Assessment 191(722), (2019), 1-14.

[7]. Duarte-Nass C., Rebolledo K., Valenzuela T., Kopp M., Jeison D., Rivas M., Azócar L., Torres-Aravena Á., Ciudad G., "Application of microbe-induced carbonate precipitation for copper removal from copper-enriched waters: Challenges to future industrial application", Journal of Environmental Management, 256, (2020), 109938.

[8]. Yan Y., Liang X., Ma J., Shen J., "Rapid removal of copper from wastewater by Fe-based amorphous alloy", Intermetallics, 124, (2020), 106849.

[9]. Elvan H., Ozdes D., Duran C., Sahin D., Tufekci M., Bahadir Z., "Separation and preconcentration of copper in environmental samples on Amberlite XAD-8 resin after complexation with a carbothioamide derivative", Química Nova, 36(6), (2013), 831-835.

[10]. Enez B., Varhan Oral E., Aguloglu Fincan S., Ziyadanogullari B., "Comparison of Methods for the Preconcentration of Cadmium(II) Using Amberlite XAD-16 Resin Modified with Anoxybacillus caldiproteolyticus and Geobacillus stearothermophilus as Novel Biosorbents", Analytical Letters, 53(2), (2020), 322-342.

[11]. Jayakumar V., Govindaradjane S., Senthilkumar P., Rajamohan N., Rajasimman M., "Sustainable removal of cadmium from contaminated water using green alga–Optimization, characterization and modeling studies", Environmental Research, 199, (2021), 111364.

[12]. Chatterjee S., Sivareddy I., De S., "Adsorptive removal of potentially toxic metals (cadmium, copper, nickel and zinc) by chemically treated laterite: Single and multicomponent batch and column study", Journal of Environmental Chemical Engineering, 5(4), (2017), 3273-3289.

[13]. Sun H., Xia N., Liu Z., Kong F., Wang S., "Removal of copper and cadmium ions from alkaline solutions using chitosan-tannin functional paper materials as adsorbent", Chemosphere, 236, (2019), 124370.

[14]. Jiang Q., Song X., Liu J., Shao Y., He W., Feng Y., "In-situ enrichment and removal of Cu(II) and Cd(II) from low-strength wastewater by a novel microbial metals enrichment and recovery cell (MMERC)", Journal of Power Sources, 451, (2020), 227627.

[15]. Bandara T., Xu J., Potter I. D., Franks A., Chathurika J., Tang C., "Mechanisms for the removal of Cd(II) and Cu(II) from aqueous solution and mine water by biochars derived from agricultural wastes", Chemosphere, 254, (2020), 126745.

[16]. Arancibia-Miranda N., Manquián-Cerda K., Pizarro C., Maldonado T., Suazo-Hernández J., Escudey M., Bolan N., Sarkar B., "Mechanistic insights into simultaneous removal of copper, cadmium and arsenic from water by

iron oxide-functionalized magnetic imogolite nanocomposites", Journal of Hazardous Materials, 398, (2020), 122940.

[17]. Ma J., Huang W., Zhang X., Li Y., Wang N., "The utilization of lobster shell to prepare low-cost biochar for high-efficient removal of copper and cadmium from aqueous: Sorption properties and mechanisms", Journal of Environmental Chemical Engineering, 9(1), (2021), 104703.

[18]. Gendy E. A., Ifthikar J., Ali J., Oyekunle D. T., Elkhlifia Z., Shahib I. I., Khodair A. I., Chen Z., "Removal of heavy metals by Covalent Organic Frameworks (COFs): A review on its mechanism and adsorption properties", Journal of Environmental Chemical Engineering, (2021), 105687.

[19]. Ru J., Wang X., Wang F., Cui X., Du X., Lu X., "UiO series of metal-organic frameworks composites as advanced sorbents for the removal of heavy metal ions: Synthesis, applications and adsorption mechanism", Ecotoxicology and Environmental Safety, 208, (2021), 111577.

[20]. Erol B., Erol K., Gökmeşe E., "The effect of the chelator characteristics on insulin adsorption in immobilized metal affinity chromatography", Process Biochemistry, 83, (2019), 104-113.

[21]. Erol K., Yıldız E., Alacabey İ., Karabörk M., Uzun L., "Magnetic diatomite for pesticide removal from aqueous solution via hydrophobic interactions", Environmental Science and Pollution Research, 26(32), (2019), 33631-33641.

[22]. Zhang Y., Cheng Q., Wang C., Li H., Han X., Fan Z., Su G., Pan D., Li Z., "Research progress of adsorption and removal of heavy metals by chitosan and its derivatives: A review", Chemosphere, 279, (2021), 130927.

[23]. Gürbüz F., Özcan, A., Çiftci H., Acet Ö., Odabaşı M., "Treatment of textile effluents through bio-composite column: decolorization and COD reduction", International Journal of Environmental Science and Technology, 16, (2019), 8653–8662.

[24]. Lee L. Y., Gan S., Tan M. S. Y., Lim S. S., Lee X. J., Lam Y. F., "Effective removal of Acid Blue 113 dye using overripe Cucumis sativus peel as an eco-friendly biosorbent from agricultural residue", Journal of Cleaner Production, 113, (2016), 194-203.

[25]. Singh S., Parveen N., Gupta H., "Adsorptive decontamination of rhodamine-B from water using banana peel powder: a biosorbent", Environmental Technology & Innovation, 12, (2018), 189-195.

[26]. Rehman R., Farooq S., Mahmud T., "Use of agro-waste Musa acuminata and Solanum tuberosum peels for economical sorptive removal of emerald green dye in ecofriendly way", Journal of Cleaner Production, 206, (2019), 819-826.

[27]. Ahmad A., Siddique J. A., Laskar M. A., Kumar R., Mohd-Setapar S. H., Khatoon A., Shiekh R. A., "New generation Amberlite XAD resin for the removal of metal ions: A review", Journal of Environmental Sciences, 31, (2015), 104-123.

[28]. Elbadawy H. A., Abdel-Salam A. H., Khalil T. E., "The impact of an Amberlite XAD-16-based chelating resin for the removal of aqueous Cd(II) and Pb(II) ions", Microchemical Journal, 165, (2021), 106097.

[29]. Varhan Oral E., Özdemir S., Dolak I., Okumus V., Dundar A., Ziyadanogullari B., Aksoy Z., Onat R., "Anoxybacillus sp. SO B1–immobilized Amberlite XAD-16 for solid-phase preconcentration of Cu(II) and Pb(II) and their determinations by flame atomic absorption spectrometry", Bioremediation Journal, 19(2), (2015), 139-150.

[30]. ul Hoque M. I., Chowdhury D. A., Holze R., Chowdhury A. N., Azam M. S., "Modification of Amberlite XAD-4 resin with 1, 8-diaminonaphthalene for solid phase extraction of copper, cadmium and lead, and its application to determination of these metals in dairy cow's milk", Journal of Environmental Chemical Engineering, 3(2), (2015), 831-842.

[31]. Ghaedi M., Montazerozohori M., Hekmati A., Roosta M., "Solid phase extraction of heavy metals on chemically modified silica-gel with 2-(3-silylpropylimino) methyl)-5-bromophenol in food samples", International Journal of Environmental Analytical Chemistry, 93(8), (2013), 843-857.

[32]. Dogan S., Dinçer Kaya F. N., Atakol O., "Enrichment of copper and nickel with solid phase extraction using multiwalled carbon nanotubes modified with Schiff bases", International Journal of Environmental Analytical Chemistry, 95(8), (2015), 698-712.

[33]. Varhan Oral E., Dolak I., Temel H., Ziyadanogullari B., "Preconcentration and determination of copper and cadmium ions with 1, 6-bis (2-carboxy aldehyde phenoxy) butane functionalized Amberlite XAD-16 by flame atomic absorption spectrometry", Journal of Hazardous Materials, 186(1), (2011), 724-730.

[34]. Amin A. S., Moalla S. M., Khalil M. A., "Solid Phase Extraction Utilization for Colorimetric Determination of Zinc in Waters, Food, Milk, and Biological Samples", International Journal of Analytical and Bioanalytical Methods, 1(006), (2019), 1-8.

[35]. Özdemir S., Kılınç E., Fatih S., "A novel biosorbent for preconcentrations of Co(II) and Hg(II) in real samples", Scientific Reports, 10(1), (2020), 1-9.

[36]. Barquilha C. E., Cossich E. S., Tavares C. R., da Silva E. A., "Biosorption of nickel(II) and copper(II) ions from synthetic and real effluents by alginate-based biosorbent produced from seaweed Sargassum sp", Environmental Science and Pollution Research, 26(11), (2019), 11100-11112.

[37]. de Freitas G. R., da Silva M. G. C., Vieira M. G. A., "Biosorption technology for removal of toxic metals: a review of commercial biosorbents and patents", Environmental Science and Pollution Research, 26(19), (2019), 19097-19118.

[38]. Okumuş V., Özdemir S., Kılınç E., Dündar A., Yüksel U., Baysal Z., "Preconcentration with Bacillus subtilis–immobilized amberlite XAD-16: determination of Cu2+ and Ni2+ in river, soil, and vegetable samples", Bioremediation Journal, 19(1), (2015), 47-55.

[39]. Baytak S., Channa A. M., Çamuroğlu E., "Mucor pusillus immobilized Amberlite XAD-4 biocomposites for preconcentration of heavy metal ions by solid-phase extraction method", Journal of Analytical Science and Technology, 9(1), (2018), 1-6.

[40]. Özdemir S., Okumuş V., Kılınç E., Bilgetekin H., Dündar A., Ziyadanogˇulları B., "Pleurotus eryngii immobilized Amberlite XAD-16 as a solid-phase biosorbent for preconcentrations of Cd2+ and Co2+ and their determination by ICP-OES", Talanta, 99, (2012), 502-506.

[41]. Jagung P. T., "Removal of Zn(II), Cd(II) and Mn(II) from aqueous solutions by adsorption on maize stalks", Malaysian Journal of Analytical Sciences, 15(1), (2011), 8-21.

[42]. Özdemir S., Okumuş V., Dündar A., Kılınç E., "The use of fungal biomass Agaricus bisporus immobilized on amberlite XAD-4 resin for the solid-phase preconcentration of Thorium", Bioremediation Journal, 18(1), (2014), 38-45.

[43]. García A. V., Santonja M. R., Sanahuja A. B., Selva M. d. C. G., "Characterization and degradation characteristics of poly(ε-caprolactone)-based composites reinforced with almond skin residues", Polymer Degradation and Stability, 108, (2014), 269-279.

[44]. Yahaya Y. A., Don M. M., "Pycnoporus sanguineus as potential biosorbent for heavy metal removal from aqueous solution: A review", Journal of Physical Science, 25(1), (2014), 1.

[45]. Ziaei E., Mehdinia A., Jabbari A., "A novel hierarchical nanobiocomposite of graphene oxide–magnetic chitosan grafted with mercapto as a solid phase extraction sorbent for the determination of mercury ions in environmental water samples", Analytica Chimica Acta, 850, (2014), 49-56.

[46]. Özdemir S., Kilinc E., Celik K. S., Okumus V., Soylak M., "Simultaneous preconcentrations of Co2+, Cr6+, Hg2+ and Pb2+ ions by Bacillus altitudinis immobilized nanodiamond prior to their determinations in food samples by ICP-OES", Food Chemistry, 215, (2017), 447-453.

[47]. Kara D., Fisher A., Hill S. J., "Preconcentration and determination of trace elements with 2,6-diacetylpyridine functionalized Amberlite XAD-4 by flow injection and atomic spectroscopy", Analyst, 130(11), (2005), 1518-1523.

[48]. Karadaş C., Kara D., "On-line preconcentration and determination of trace elements in waters and reference cereal materials by flow injection–FAAS using newly synthesized 8-hydroxy-2-quinoline carboxaldehyde functionalized Amberlite XAD-4", Journal of Food Composition and Analysis, 32(1), (2013), 90-98.

[49]. Karadaş C., Turhan O., Kara D., "Synthesis and application of a new functionalized resin for use in an on-line, solid phase extraction system for the determination of trace elements in waters and reference cereal materials by flame atomic absorption spectrometry", Food Chemistry, 141(2), (2013), 655-661.

MANAS Journal of Engineering
ISSN 1694-7398 | e-ISSN 1694-7398

Volume 11, Issue 2, (2023) Pages 190-203
https://doi.org/10.51354/mjen.1265134

Wastewater treatment plant design and modeling for the city of Erzurum

Erdinç Aladağ[1,*], Alper Nuhoğlu[2]

[1] Department of Environmental Engineering, Faculty of Engineering, Van Yuzuncu Yil University, Van, 65080, Turkey, erdincaladag@gmail.com, ORCID: 0000-0003-1354-0930

[2] Department of Environmental Engineering, Faculty of Engineering, Atatürk University, Erzurum, 25240, Turkey, anuhoglu@yahoo.com, ORCID: 0000-0001-7887-0987

ABSTRACT

Currently large amounts of wastewater are produced by domestic and industrial activities. Discharge of wastewater to the receiving environment without treatment causes significant health and environmental problems. Modeling and optimization of Wastewater Treatment Plants (WWTP) developed to treat domestic wastewater play key roles in determining unit components, design parameters and operation conditions. Several models were proposed to predict the treatment performance in WWTP. The Activated Sludge Model No. 1 (ASM1) is one of the commonly-used standard models developed to better understand removal of carbonaceous and nitrogenous materials. In this study, a WWTP is proposed for domestic wastewater using grit chamber, circular primary and secondary clarifiers, completely-mixed aeration tank, sludge thickener, sludge dewatering and anaerobic digestion processes together. The WWTP was modeled with ASM1 noting the topographic and meteorological features of the city. The treatment performances with wastewater temperatures of 10°C and 20°C were investigated for this plant, operating at high elevation. Removal efficiencies at 20°C were 95.7%, 92.2%, 97.9% and 99.2% for MLSS, COD, BOD and NH_4, while effluent concentrations were 14.83, 48.51, 6.55 and 0.3 mg L^{-1}, respectively. At 10°C, removal efficiencies were 88.9%, 88%, 93.2%, and 26.9%, while effluent concentrations were 38, 75, 21.83 and 26.13 mg L^{-1}, respectively. A clear reduction was observed in nitrogenous material removal at low temperatures. Additionally, keeping dissolved oxygen concentration in the aeration tank at 1.5 mg L^{-1} with PID control increased nitrification efficiency by 30%. The findings reveal the importance of modeling studies during planning of WWTP.

ARTICLE INFO

Research article

Received: 14.03.2023
Accepted: 26.06.2023

Keywords:
WWTP,
ASM1,
GPS-X,
COD,
MLSS,
Nitrogen

**Corresponding author*

1. Introduction

In spite of 70% of the Earth's surface being covered with water, only 0.5% of this amount can be used as drinking water. Due to rapid population increase and unplanned urbanization, limited water resources are rapidly polluted and the demand for clean water is increasing every day. Uncontrolled discharge of domestic and industrial wastewaters into receiving environments negatively affects human health and the ecological balance. The correlation between the use of drinking water sources polluted by wastewater and diseases was determined for the first time by Dr. John Snow in 1854 [1, 2]. Since this date, intense research began to focus on wastewater treatment. Firstly the focus was on removal of carbonaceous organic matter. However, discharge of this partially treated water into still waters like lakes and estuaries caused eutrophication due to high nitrogen and phosphorus content. As a result, wastewater treatment plants founded in later years targeted the removal of carbonaceous material along with nitrogenous and phosphorous materials. The activated sludge process (ASP) developed by Ardern and Lockette in 1914 was a turning point in terms of biological treatment [3]. ASP is based on biologically-useful material in wastewater being consumed by microorganisms for energy acquirement or structural change [4]. These systems, named "active or activated" biomass produced to stabilize waste under aerobic conditions, became rapidly popular from the 1940s due to success in treating wastewater [5]. Activated sludge (AS) is a mixture containing living and dead microorganisms along with organic and inorganic materials. ASP comprises two separate stages of aeration and precipitation. In the first stage, sludge aerated by mixers or diffusers is not permitted to precipitate. Theoretically full mixing is ensured for organic matter, oxygen and microorganisms. In this environment, called suspended growth systems, organic matter in wastewater is degraded, while continuous active biomass sludge develops. After this stage, though organic

matter is removed, the treatment process is not complete. Wastewater is a solid-fluid mixture in suspension containing suspended solid matter with organic and inorganic form. For separation of treated water and sludge, this mixture is transferred to the second stage. In the clarification tank, mixing is not performed and water speed is very low. As some of the precipitated sludge may continue wastewater treatment in the first stage, it is returned to the completely-mixed aeration tank, while the remaining portion is removed from the system to be used in sludge dryers or biogas units [6]. Nearly every wastewater treatment plant (WWTP) includes ASP, which is the most commonly chosen biological treatment system in the present day [7]. Though several studies have been performed to date about the operation of this process, which has an overly complicated biological mechanism, it still involves several unsolved problems [8]. The population distribution of microorganisms in the process, the seasonal and hourly differences in flow rate and organic load amounts in the system, yearly and daily changes in independent external factors like temperature, pH and waste content are among the leading reasons making it more difficult to understand AS systems [9]. The lack of detailed analysis of water entering the plant, lack of sufficient investigation of external environmental conditions and not performing accurate modeling studies may cause deficiencies or unnecessary scaling in process design and mistaken applications in operating procedures. Currently most ASP are constructed with dimensions that are able to deal with much higher flow than the wastewater flow rate entering the system. Additionally, it appears that even plants operating well cannot provide effluent water standards within certain periods of the operating duration [10].

To be able to better understand ASP, one of the most complicated microbial systems designed for a certain purpose, it is crucial important to model process dynamics. Several different heterotroph and autotroph bacterial groups must act together to fulfil different functions like stabilization of organic carbon, nitrification, denitrification and advanced biological phosphorus removal. Currently, metabolic activities of microorganisms can be predicted through modeling and system parameters can be separately checked to ensure optimum performance of the process [11]. In the early period, the three-component activated sludge model (ASM) focusing on oxygen use, substrate consumption and biomass production was used. However, this basic approach remained inadequate to assess wastewater treatment performance and to predict sludge amounts most of the time. As a result, the International Association on Water Pollution Research and Control (IAWPRC) created a working group in 1983 with the aim of ensuring implementation of more practical and realistic modeling for both the design and operation stages of ASP. This study group published their work with the name activated sludge model no. 1 (ASM1) in 1987 [12]. This model is a very comprehensive ASM comprising 13 components and 8 processes. In later periods, two new models were developed comprising many more components than ASM1 and were more explanatory for determination of biological phosphorus removal, nitrification, and denitrification processes [13]. However, ASM1 is a widely-accepted model that successfully explains removal of carbonaceous and nitrogenous material in single sludge systems for domestic wastewater [14].

The rapid development of computer and electronic technologies in the present day have made it possible for personal computer users to access equipment that used to be expensive, difficult to access and require large spaces. Software technology has adapted to these developments. New generation computer software has begun to be used with advanced visual interfaces, able to solve more complicated mathematical models in a short duration, making it possible to run a variety of scenarios, using open-source code and open to development. As in every area, new generation software has become popular for the modeling and simulation of wastewater treatment plants and more comprehensive computer software is offered to the market with every passing day. ASM models developed by IWA have been successfully applied using diverse design, simulation and optimization software like GPS-X (Hydromantis Environmental Software Solutions, Inc. Hamilton, ON, Canada), BioWin (EnviroSim associates LTD. Hamilton, ON, Canada), ASIM Activated Sludge SIMulation Program (Swiss Federal Institute of Aquatic Science and Technology Eawag, Dübendorf, Switzerland), SIMBA (IFAK-Institut für Automation und Kommunikation e.V. Magdeburg, Germany), WEST (DHI A/S Hørsholm, Denmark), STOAT (WRc plc. Wiltshire, UK) and Sumo (Dynamita, Sigale, France) [15, 16]. Among these, GPS-X software developed by the Canadian Hydromantis firm founded in 1985 is among the most commonly chosen at present and this software has features with broad scope for modeling and simulation of wastewater treatment plants. The GPS-X software includes nearly all processes that may occur in a WWTP. Additionally, it offers great possibilities for design and operation of WWTP with unrivaled features like useful interface, advanced graphic applications, determination of interactions between processes, optimization of critical parameters during design, and the ability to offer dynamic solutions to topics about reactions during special situations that may be encountered in WWTP.

In this study, modelling was performed for a WWTP proposed for domestic wastewater treatment in Erzurum city center, located at high elevation in continental climate conditions, using the GPS-X software. While modeling ASP, ASM1 was chosen, which is most commonly used in the literature to model the performance of full-scale domestic wastewater treatment plants. The wastewater components of COD, dissolved COD, BOD, MLSS and nitrogen parameters were characterized in the model. Literature screening was

performed for other parameters and values widely used for domestic wastewater were accepted. The type, number, and physical features of treatment processes included in the plant and influent properties were mathematically modeled with the aid of GPS-X software. The effect of wastewater temperature on effluent concentration was researched to investigate whether the calculated value met the effluent standards or not. Later, the correlation between dissolved oxygen concentration in the aeration tanks, fixed to a certain value with PID control, with carbonaceous and nitrogenous material removal was investigated.

2. Materials and methods

2.1 Study area and wastewater characteristics

Erzurum city center, chosen as study area, is located in the Northeast Anatolian region in Türkiye. The city is divided into three central counties of Aziziye, Palandöken and Yakutiye and is home to 428,302 people according to 2021 Turkish Statistical Institute (TÜİK) data. The city center is located at 1853 m above sea level and is the country's most crowded city at high elevation [17]. The main industries linked to the urban wastewater system in Erzurum are the organized industrial zone, slaughterhouse and milk processing industries. Table 1 presents the characterization of wastewater from Erzurum.

In plants where biological treatment will be performed, the biologically degradable and non-degradable (inert) parts play important roles in terms of operation and modeling of ASP. COD, showing the total carbonaceous matter in influent, comprises the total of soluble inert organic matter (S_I), readily biodegradable substrate (S_S), particulate inert organic matter (X_I) and slowly biodegradable substrate (X_S) values. As the readily biodegradable substrate in wastewater comprises volatile fat acids, carbohydrates, alcohols, peptones and amino acids, it can be rapidly absorbed by heterotroph microorganisms under aerobic and anoxic conditions. According to research, the slowly biodegradable substrate comprises 35-60% of wastewater and is formed of relatively more complicated molecules, so microorganisms require a longer time to convert it to simple molecules [18]. The concentration of slowly biodegradable substrate is important in terms of modeling the hydrolysis process, while it partly plays a role in determining the age of sludge. Particulate inert organic matter is held by clarifiers and discarded from the system. Soluble inert organic matter has great importance in terms of determining the performance of the system as it is included in the effluent COD concentration [19]. Nitrogenous components include soluble nitrite and nitrate nitrogen (S_{NO}), soluble free and ionized ammonia nitrogen (S_{NH}), soluble biodegradable organic nitrogen (S_{ND}) and particulate biodegradable organic nitrogen (X_{ND}). Due to these parameters, used to be able to better understand plant operation, total nitrogen (TN) may be investigated in inert, readily degradable and slowly degradable portions.

Table 1. *Wastewater characteristics of Erzurum city center.*

Parameter	Unit	Value
Q_{design}	$m^3\ h^{-1}$	5329
Q_{mean}	$m^3\ h^{-1}$	3468
Q_{min}	$m^3\ h^{-1}$	2210
Q_{max}	$m^3\ h^{-1}$	7265
pH	-	6.99-8.87
MLSS	$g\ m^{-3}$	343
COD	$g\ m^{-3}$	631
BOD	$g\ m^{-3}$	321
TKN	$g\ m^{-3}$	54
TP	$g\ m^{-3}$	13
S_I	$g\ m^{-3}$	30
S_S	$g\ m^{-3}$	149.36
X_S	$g\ m^{-3}$	332.45
X_I	$g\ m^{-3}$	112.39
S_{NO}	$g\ m^{-3}$	0
S_{NH}	$g\ m^{-3}$	35.75
S_{ND}	$g\ m^{-3}$	1.93
X_{ND}	$g\ m^{-3}$	9.68

2.2. Wastewater treatment processes

In this study, the WWTP used grit chambers, distribution and collection structures, circular primary and secondary clarifier tanks, completely-mixed aeration tank, sludge thickener and dewatering tanks and anaerobic digesters. Wastewater was sent to the aerated grit chambers after preliminary physical processing. Sand was removed to prevent unwanted accumulation in other units and wear on machinery. All types of organic matter were removed from sand by passing through separators and washers before it is transferred to containers. Grease was removed from the surface of the wastewater and pumped to grease collection units. Wastewater was divided through distribution structures linked to the number of reactors in the treatment plant. Additionally, backups were present considering any possible breakdown of the distribution valves. Water coming from the secondary clarifier tank was sent to the recycling line with this distribution structure. In the circular primary clarifier tank, suspended solid matter and organic matter is removed. The clarified wastewater is discharged through weirs and the precipitated primary sludge is thickened in sludge cones. The distributed wastewater passing from the reactors is combined using collecting structures and thus becomes homogeneous. Wastewater passing through the circular primary clarifier tank is sent to the ASP to remove organic matter and nutrients after passing through a pumping station. AS tanks

are aerated by fine bubble disc diffusors. Additionally, submerged mixers are used with the aim of ensuring that both suspended solid matter precipitate and better aeration within the tank. Wastewater is sent to the circular secondary clarifier tanks from the aeration tanks. The circular secondary clarifier tanks, where suspended solid matter and treated water are separated, are one of the most important components of ASPs. Some of the precipitated sludge is returned to the AS tanks to check sludge age and sludge thickening. Excess sludge taken from the system is concentrated through sludge thickeners working with the traditional gravity method. Thickened sludge from the circular primary and secondary clarifiers is converted into end products like carbon dioxide and methane in the anaerobic tank. Sludge is sent continuously or in batches and kept in the reactor for varying durations. Sludge removed from the reactor has reduced concentrations of organic matter and pathogenic microorganisms. Sludge passing through the anaerobic tanks is dried by being centrifuged or pressed. Later it is stored in containers or buried. When creating the model in GPS-X software, the ASP and units affecting the operation of this process were included. The plant uses 4 grit chambers, 4 circular primary clarifier tanks, 5 fully mixed completely-mixed aeration tanks and 6 circular secondary clarifier tanks. Four sludge thickener tanks are used each for excess sludge from the circular primary and secondary clarifiers. The thickened sludge is sent to anaerobic digesters with the aim of gas production. Water from the sludge thickener tanks is recycled to the circular primary clarifier input and aeration tank input. The design parameters and technical information for units included in the WWTP modeling study are shown in Table 2.

Table 2. *Technical specifications of the processes in the wastewater treatment plant.*

Process	Parameter	Unit	Value
Grit chamber	Number of units	-	4
	Volume per unit	m^3	209
	Hydraulic retention time, (Q_{max})	minute	7
	Sand production per volume	g m^{-3}	20
Circular primary clarifier	Number of units	-	4
	Volume per unit	m^3	1130
	Hydraulic retention time, (Q_{mean})	hour	1
	Diameter	m	24
	Height	m	2.5
	Surface load, (Q_{max})	m^3 m^{-2}·day^{-1}	100
	Sludge load	kg day^{-1}	14010
Completely-mixed aeration tank	Number of units	-	5
	Volume per unit	m^3	17578.2
	Hydraulic retention time, (Q_{max})	hour	12
	Sludge age	day	13
	Oxygen flow rate	m^3 $hour^{-1}$	12000
	MLSS concentration	kg m^{-3}	3.7
Circular secondary clarifier	Number of units	-	6
	Volume per unit	m^3	5273.67
	Hydraulic retention time, (Q_{max})	hour	4.4
	Diameter	m	38
	Height	m	4.65
	Surface load, (Q_{max})	m^3 m^{-2}·day^{-1}	25.7
	Sludge flow rate	m^3 day^{-1}	2700
	Recycle sludge rate	m^3 m^{-3}	0.75
Primary sludge thickener	Number of units	-	4
	Volume per unit	m^3	353.45
	Diameter	m	10
	Concentrated sludge flow rate	m^3 day^{-1}	200
Secondary sludge thickener	Number of units	-	4
	Volume per unit	m^3	450
	Diameter	m	11.3
	Concentrated sludge flow rate	m^3 day^{-1}	400
Anaerobic digester	Number of units	-	4
	Volume per unit	m^3	4342
	Temperature	°C	35
	Hydraulic retention time	day	25

2.3. Activated Sludge Model No. 1 (ASM1)

The ASM developed by the study group founded by IAWPRC was published under the name ASM1 in 1987. The first aim when developing the model was to create a consensus about a simple model to investigate available models and to be able to realistically predict the performance of carbon-removal, nitrification and denitrification systems. In later years, the IAWPRC took the name International Association on Water Quality (IAWQ) and developed ASM2 in 1995, ADM2d in 1999 and ASM3 in 2000 [20]. However, ASM1 developed by Henze et al. (1987) is a comprehensive model comprising 13 components and 8 processes that is adequate for biological treatment of domestic wastewater [12]. Table 3 shows the explanations of the components and units used in the model. In this notation, S symbolizes soluble compounds, while X symbolizes insoluble compounds. B, S and O subindexes represent biomass, substrate and oxygen, respectively. A and H show autotrophic and heterotrophic microorganisms. In the model, the COD parameter is chosen in terms of making connections between organic matter, biomass and electron receivers. Organic matter is separated into two main groups of biodegradable and non-degradable matter. Biodegradable matter is grouped as readily degradable (S_S) and slowly degradable matter (X_S); while non-degradable matter is grouped as inert (S_I) and particulate (X_I). The particulate matter emerging with degradation of biomass (X_P) comprises slowly biodegradable substrate as a result of the decay of microorganisms. Though alkalinity (S_{ALK}) is not one of the basic components of the model, it is important in terms of revealing pH changes in the model. In the model, ammonium nitrogen (S_{NH}), organic nitrogen (S_{ND}) and particulate nitrogen (X_{ND}) are accepted as being biodegradable. Particulate nitrogen may be hydrolyzed to soluble nitrogen during hydrolysis of the slowly biodegrading substrate. Soluble organic nitrogen may be converted to ammonium nitrogen by heterotrophic bacteria. Later ammonium nitrogen is used as a nitrogen source for heterotrophic bacteria, while it is used as an energy source and for new cell synthesis by autotropic bacteria. Particulate nitrogen emerges as a result of the decay of both heterotrophic and autotrophic bacteria [21].

Table 3. *ASM1 state variables.*

Component	State variable	Symbol	Unit
1	Soluble inert organic matter	S_I	g COD m^{-3}
2	Readily biodegradable substrate	S_S	g COD m^{-3}
3	Particulate inert organic matter	X_I	g COD m^{-3}
4	Slowly biodegradable substrate	X_S	g COD m^{-3}
5	Active heterotrophic biomass	X_{BH}	g COD m^{-3}
6	Active autotrophic biomass	X_{BA}	g COD m^{-3}
7	Particulate products arising from biomass decay	X_P	g COD m^{-3}
8	Dissolved oxygen	S_O	g O_2 m^{-3}
9	Nitrate and nitrite nitrogen	S_{NO}	g N m^{-3}
10	Free and ionized ammonia nitrogen	S_{NH}	g N m^{-3}
11	Soluble biodegradable organic nitrogen	S_{ND}	g N m^{-3}
12	Particulate biodegradable organic nitrogen	X_{ND}	g N m^{-3}
13	Alkalinity	S_{ALK}	Molar units

ASM1 comprises 8 processes encompassing proliferation and decay of microorganisms, ammo-nitrification of soluble organic nitrogen, and hydrolysis of slowly degrading substrate and particulate organic nitrogen. The relationships between the parameters and compounds used to create these processes are mentioned in brief below [22].

- Aerobic proliferation of heterotrophs: This is accepted as the main process for COD removal. In this process using oxygen as an electron acceptor, in the process the readily degraded substrate and ammonium nitrogen are consumed to obtain energy and synthesize new cells.
- Anoxic proliferation of heterotrophs: The denitrification event occurs in this process. Heterotrophs consume nitrate as electron acceptor while using the readily degraded organic matter as substrate. In this process, ammonium nitrogen is used for synthesis of new cells. Since substrate removal under anoxic conditions occurs more slowly than under aerobic conditions, the rate expression is multiplied by the correction factor η_g which is less than 1.
- Aerobic proliferation of autotrophs: In this process, oxygen and ammonium nitrogen are consumed to produce nitrifying microorganisms and nitrate emerges at the end of the process. Additionally, autotrophs cause

a pronounced effect on alkalinity when proliferating aerobically.

- Decay of heterotrophs: This process is modeled according to the death-renewal hypothesis. According to this approach, some of the active biomass converts to slowly decaying particulate matter and inert particulate products. In the death renewal approach, an electron acceptor like O_2 or NO_3 is not used and it is accepted that COD removal does not occur.
- Decay of autotrophs: This is modeled with the death-renewal approach as for degradation of heterotrophic microorganisms. Autotrophic biomass decays and is converted to slowly degrading particulate matter and inert particulate matter.
- Ammo-nitrification of soluble organic nitrogen: In this process, biodegradable nitrogen is converted to ammonium nitrogen by heterotrophic microorganisms. During ammo-nitrification, alkalinity variations occur as hydrogen ions are consumed.
- Hydrolysis of captured organics: This event is the conversion of slowly biodegradable substrate captured in sludge to readily degraded substrate by extracellular enzymes. Hydrolysis rate is connected to the delay in electron acceptor consumption during substrate removal.
- Hydrolysis of captured organic nitrogen: This is the hydrolysis of particulate organic nitrogen to soluble organic nitrogen. Hydrolysis rate is accepted as being dependent on the ratio of particulate organic nitrogen to the slowly biodegradable substrate.

Table 4 includes the matrix view of the components and processes in ASM1. The matrix view allows the opportunity to more readily understand complicated models involving many parameters [23]. Here, the i variable are column components, while the rows shown by j represent processes. The rate equation for each process is included in the rightmost column. The conversion rate equation (r_i) for each component in the model is calculated with the aid of the following equation (Eq.1).

$$r_i = \sum_j \nu_{ij}\rho_j \quad (1)$$

In this equation, ν is the component coefficient and ρ is the process rate equation.
For example, the readily biodegradable substrate (S_S) may be expressed as follows with this method (Eq. 2).

$$r_{S_S} = \frac{dS_S}{dt} = \nu_{2,1}\rho_1 + \nu_{2,2}\rho_2 + \nu_{2,7}\rho_7 = -\frac{1}{Y_H}\left(\mu_{Hmax}\left(\frac{S_S}{K_S+S_S}\right)\left(\frac{S_O}{K_{OH}+S_O}\right)X_{BH}\right) - \frac{1}{Y_H}\left(\mu_{Hmax}\left(\frac{S_S}{K_S+S_S}\right)\left(\frac{K_{OH}}{K_{OH}+S_O}\right)\left(\frac{S_{NO}}{K_{NO}+S_{NO}}\right)\eta_g X_{BH}\right) + k_h\frac{X_S/X_{BH}}{K_X+(X_S/X_{BH})}\left[\left(\frac{S_O}{K_{OH}+S_O}\right)+\eta_h\left(\frac{K_{OH}}{K_{OH}+S_O}\right)\left(\frac{S_{NO}}{K_{NO}+S_{NO}}\right)\right]X_{BH} \quad (2)$$

Table 4. *Matrix representation of ASM1.*

Component → (i)	1	2	3	4	5	6	7	8	9	10	11	12	13	Process rate, ρ_j [$ML^{-3}T^{-1}$]
Process ↓ (j)	S_I	S_S	X_I	X_S	X_{BH}	X_B	X_P	S_O	S_{NO}	S_{NH}	S_{ND}	X_{ND}	S_{ALK}	
1 Aerobic growth of heterotrophs		$-\frac{1}{Y_H}$			1			$-\frac{1-Y_H}{Y_H}$		$-i_{XB}$			$-\frac{i_{XB}}{14}$	$\hat{\mu}_H\left(\frac{S_S}{K_S+S_S}\right)\left(\frac{S_O}{K_{O,H}+S_O}\right)X_{B,H}$
2 Anoxic growth of heterotrophs		$-\frac{1}{Y_H}$			1				$-\frac{1-Y_H}{2.86Y_H}$	$-i_{XB}$			$\frac{1-Y_H}{14\times 2.68Y_H}-\frac{i_{XB}}{14}$	$\hat{\mu}_H\left(\frac{S_S}{K_S+S_S}\right)\left(\frac{K_{O,H}}{K_{O,H}+S_O}\right)\left(\frac{S_{NO}}{K_{NO}+S_{NO}}\right)\eta_g X_{B,H}$
3 Aerobic growth of autotrophs						1		$-\frac{4.57-Y_A}{Y_A}$	$\frac{1}{Y_A}$	$-i_{XB}-\frac{1}{Y_A}$			$-\frac{i_{XB}}{14}-\frac{1}{7Y_A}$	$\hat{\mu}_A\left(\frac{S_{NH}}{K_{NH}+S_{NH}}\right)\left(\frac{S_O}{K_{O,A}+S_O}\right)X_{B,A}$
4 Decay of heterotrophs				$1-f_P$	-1		f_P					$-i_{XB}-f_P i_{XP}$		$b_H X_{B,H}$
5 Decay of autotrophs				$1-f_P$		-1	f_P					$-i_{XB}-f_P i_{XP}$		$b_A X_{B,A}$
6 Ammonification of soluble organic N										1	-1		$\frac{1}{14}$	$k_a S_{ND} X_{B,H}$
7 Ammonification of soluble organic N		1												$k_h\frac{X_S/X_{B,H}}{K_X+(X_S/X_{B,H})}\left[\left(\frac{S_O}{K_{O,H}+S_O}\right)+\eta_h\left(\frac{K_{O,H}}{K_{O,H}+S_O}\right)\left(\frac{S_{NO}}{K_{NO}+S_{NO}}\right)\right]X_{B,H}$
8 Hydrolysis of entrapped organic N											1	-1		$\rho_7\left(\frac{X_{ND}}{X_S}\right)$

The rates of change of components in ASM1 are linked to the basic features of the microorganisms and wastewater, environmental conditions and a variety of correction coefficients, as well as the relationship of the components with each other. In the model a total of 19 parameters were used, with 5 stochiometric and 13 kinetic parameters. The explanations and symbols for these parameters are included in Table 5. The stochiometric parameters include substrate removal and biomass formation yield, conversion coefficients and carbon:nitrogen (C:N) ratio. The kinetic parameters include a variety of coefficients and correction factors related to microorganism proliferation and decay rates, ammonization and hydrolysis. The values determined for these parameters by the IAWQ at temperatures of 10°C and 20°C and intervals in the literature are shown in Table 6 [12].

Table 5. *Description of ASM1 parameters.*

Description	Symbol
Stoichiometric parameters	
Yield for heterotrophic biomass	Y_H
Yield for autotrophic biomass	Y_A
Fraction of biomass leading to particulate products	f_P
Mass of nitrogen per mass of COD in biomass	i_{XB}
Mass of nitrogen per mass of COD in endogenous biomass	i_{XE}
Kinetic parameters	
Maximum specific growth rate for heterotrophic biomass	μ_{Hmax}
Half-saturation coefficient for heterotrophic biomass	K_S
Oxygen half-saturation coefficient for heterotrophic biomass	K_{OH}
Nitrate half-saturation coefficient for denitrifying heterotrophic biomass	K_{NO}
Decay coefficient for heterotrophic biomass	b_H
Correction factor for μ_H under anoxic conditions	η_g
Correction factor for hydrolysis under anoxic conditions	η_h
Maximum specific hydrolysis rate	k_h
Half-saturation coefficient for hydrolysis of slowly biodegradable substrate	K_X
Maximum specific growth rate for autotrophic biomass	μ_{Amax}
Ammonia half-saturation coefficient for autotrophic biomass	K_{NH}
Oxygen half-saturation coefficient for autotrophic biomass	K_{OA}
Ammonification rate	k_a
Decay coefficient for autotrophic biomass	b_A

For a WWTP model to be applicable, it is necessary to make some assumptions and acknowledge limitations. Some of these are related to the physical structure of the system, while some are related to the mathematical model. The assumptions and limitations, though ignored when creating the model, can be added to the model if desired by the user. The assumptions and limitations of ASM1 are listed below [10, 12, 22]:

- As temperature variations will affect the processes and coefficients, the system is assumed to operate at fixed temperature. If a correlation of parameters in the model with temperature is to be made, the Arrhenius equation may be used.
- The pH value is fixed and close to neutral. Though affected by several parameters, the statements related to pH are limited. To be able to monitor the effect of pH in the model, the alkalinity component (S_{ALK}) may be used.
- The variations caused to organic matter in wastewater within the reactor are not reflected in the model. For this reason, the parameters related to organic matter are fixed.
- In situations where nitrogen, phosphorus and other inorganic matter is limited, it should be checked whether inorganic nutrients have sufficient amounts, as the model does not include how organic matter removal and cell growth will be affected.
- The values for the correction factors for the denitrification process of η_g and η_h are assumed to be fixed for wastewater. Though it is possible that these parameters are affected by system structuring, this is ignored in the model.

- The coefficients for nitrification are assumed to be fixed. These coefficients are determined to reflect the inhibitory effects of other compounds in wastewater.
- The heterotrophic biomass is assumed to be homogeneous and there is no change in species over time. As parameters related to heterotrophic biomass are assumed to be fixed, the effects of substrate concentration gradient, reactor structuring and sludge precipitation features are not included in the model.
- Adhesion of organic matter with particulate structure to biomass is accepted as instantaneous.
- Hydrolysis of organic matter and organic nitrogen is assumed to occur at equal rates and simultaneously in connection with each other.
- The electron acceptor type is not affected by losses occurring due to decay of active biomass.

Table 6. *Typical values of ASM1 parameters.*

Symbol	Unit	Value at 10°C	Value at 20°C	Range
Y_H	g cell COD formed (g COD oxidized)$^{-1}$	0.67	0.67	0.38-0.75
Y_A	g cell COD formed (g N oxidized)$^{-1}$	0.24	0.24	0.07-0.28
f_P	dimensionless	0.08	0.08	-
i_{XB}	g N (g COD)$^{-1}$ in biomass	0.086	0.086	-
i_{XE}	g N (g COD)$^{-1}$ in endogenous mass	0.06	0.06	-
μ_{Hmax}	day^{-1}	3	6	0.6-13.2
K_S	g COD m^{-3}	20	20	5-225
K_{OH}	g O^2 m^{-3}	0.2	0.2	0.01-0.2
K_{NO}	g NO_3-N m^{-3}	0.5	0.5	0.1-0.5
b_H	day^{-1}	0.2	0.62	0.05-1.6
η_g	dimensionless	0.8	0.8	0.6-1
η_h	dimensionless	0.4	0.4	-
k_h	g slowly biodegradable COD (g cell COD·day)$^{-1}$	1	3	-
K_X	g slowly biodegradable COD (g cell COD)$^{-1}$	0.01	0.03	-
μ_{Amax}	day^{-1}	0.3	0.8	-
K_{NH}	g NH_3-N m^{-3}	1	1	-
K_{OA}	g O_2 m^{-3}	0.4	0.4	0.4-2
k_a	m^3·COD (g. day)$^{-1}$	0.04	0.08	-
b_A	day^{-1}	0.1	0.2	0.05-0.2

2.4. GPS-X software

The GPS-X software, containing nearly all processes that may occur in a WWTP developed by the Canadian Hydromantis firm, is among modeling and simulation software commonly used both academically and commercially. The GPS-X software allows the opportunity to mathematically model processes in the plant, in addition to investigating the reactions in the plant by trialing simulations, checks and a variety of scenarios. The modeling and simulation screen images for the GPS-X software are shown in Figure 1 [24].

The GPS-X software contains 6 libraries prepared according to the system to be modeled and the detail of the model. Explanations related to these libraries are given below.

- Carbon-nitrogen (cnlib): The basic library containing 12 state variables related to carbon oxidation, nitrification and denitrification processes.
- Advanced carbon-nitrogen (cn2lib): This is similar to the cnlib; however, it also models nitrite and nitrate. It has 19 state variables.
- Carbon-nitrogen-phosphorus (cnplib): A library containing 17 state variables including biological and chemical phosphorus removal.
- Carbon-nitrogen-industrial pollutant (cniplib): A library containing the cnlib library and 30 user-defined state variables.
- Advanced carbon-nitrogen-industrial pollutant (cn2iplib): This is a library containing the cn2lib and 30 user-determined state variables.

- Carbon-nitrogen-phosphorus-industrial pollutant (cnpiplib): This is a library containing the cniplib and 30 user-defined state variables.

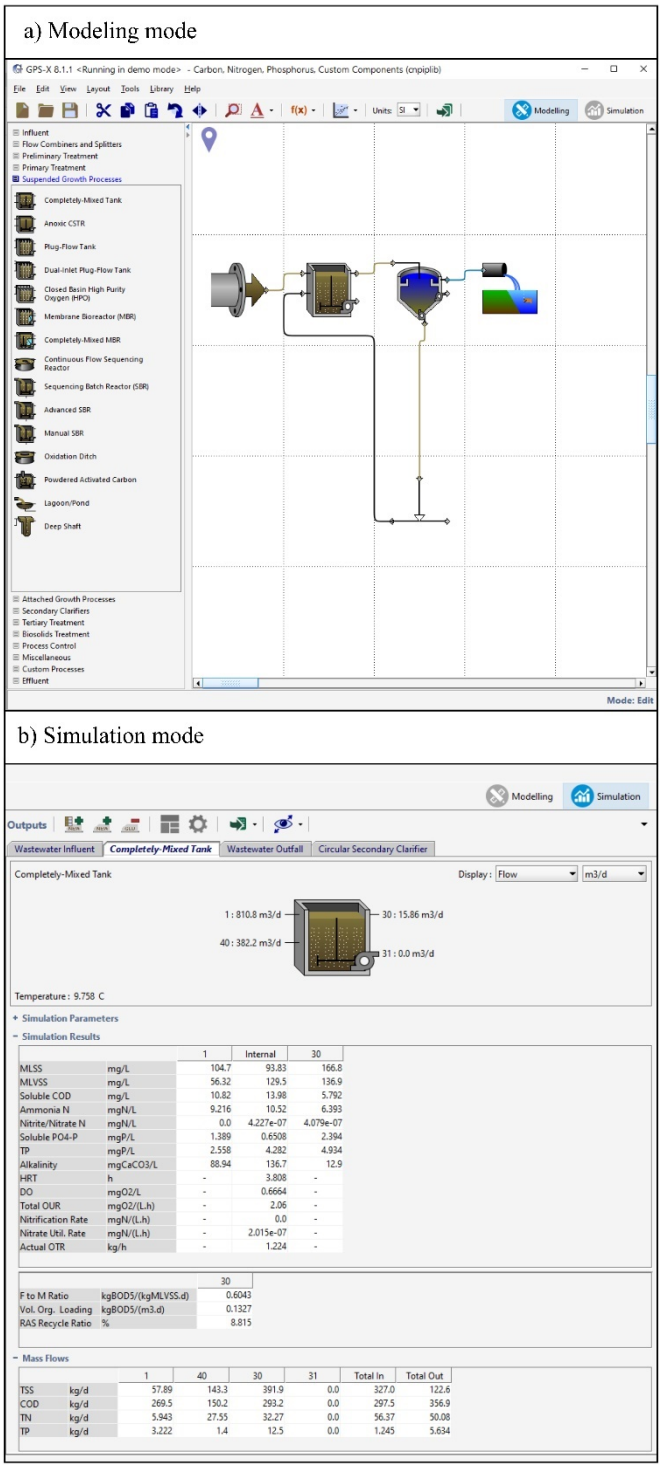

Figure 1. *Screenshot of (a) modeling and (b) simulation panels of GPS-X software.*

The software includes many units including batch and continuous wastewater input into the wastewater treatment plant, combination and distribution structures, pumping station, equilibrium tank, grit chamber, full mixed and piston flow reactors, drop filters, oxidation trench, pure oxygen tank, rotating biodiscs, lagoon, clarifying tanks, anaerobic sludge digesters, sludge dewatering and drying devices, sand filtration, membrane filters and disinfection unit. The GPS-X contains some modules where the flow scheme is prepared, reviewed and the simulation is completed. These modules are mentioned in brief below.

- Simulator: This module creates a flow diagram for units in the wastewater treatment plant and is the module determining the physical features of the processes. Additionally, model selection for operation of processes is performed in this module.
- Builder: The flow diagram developed by the user is converted to computer code in this module. The previously-chosen models are converted to mathematical model equations. This software previously used Fortran and new versions use Python and it makes the model statements operable as computer software. There are 4 types of build choices. This selection should be made appropriate to the dimension of the plant to be modeled and the number of processes.
- Analyzer: This module in the GPS-X software is able to investigate the effect of stochiometric, kinetic or physical parameters on dependent variables in the processes. This module may use 3 types of analysis methods to investigate the status of variables, according to steady state by ignoring the time variable, process dynamics and time showing the effect of the independent variables on the dependent variable at any time.
- Optimizer: This module calculates the optimum values for the independent variables to be able to determine certain intervals for certain parameters in the plant to be modelled.

Additionally, the software contains additional modules like dynamic parameter estimator, advanced control, multiple sampling license and scenario manager.

In this study, the cnlib library containing the basic features of domestic wastewater, and 12 state variables related to carbon oxidation, nitrification and denitrification processes was used. Influent characterization was defined by the BOD-based model called bod-based. All processes and connections in the plant were created using elements found in the Process table toolbox. The flow diagram for the model prepared in GPS-X software is shown in Figure 2.

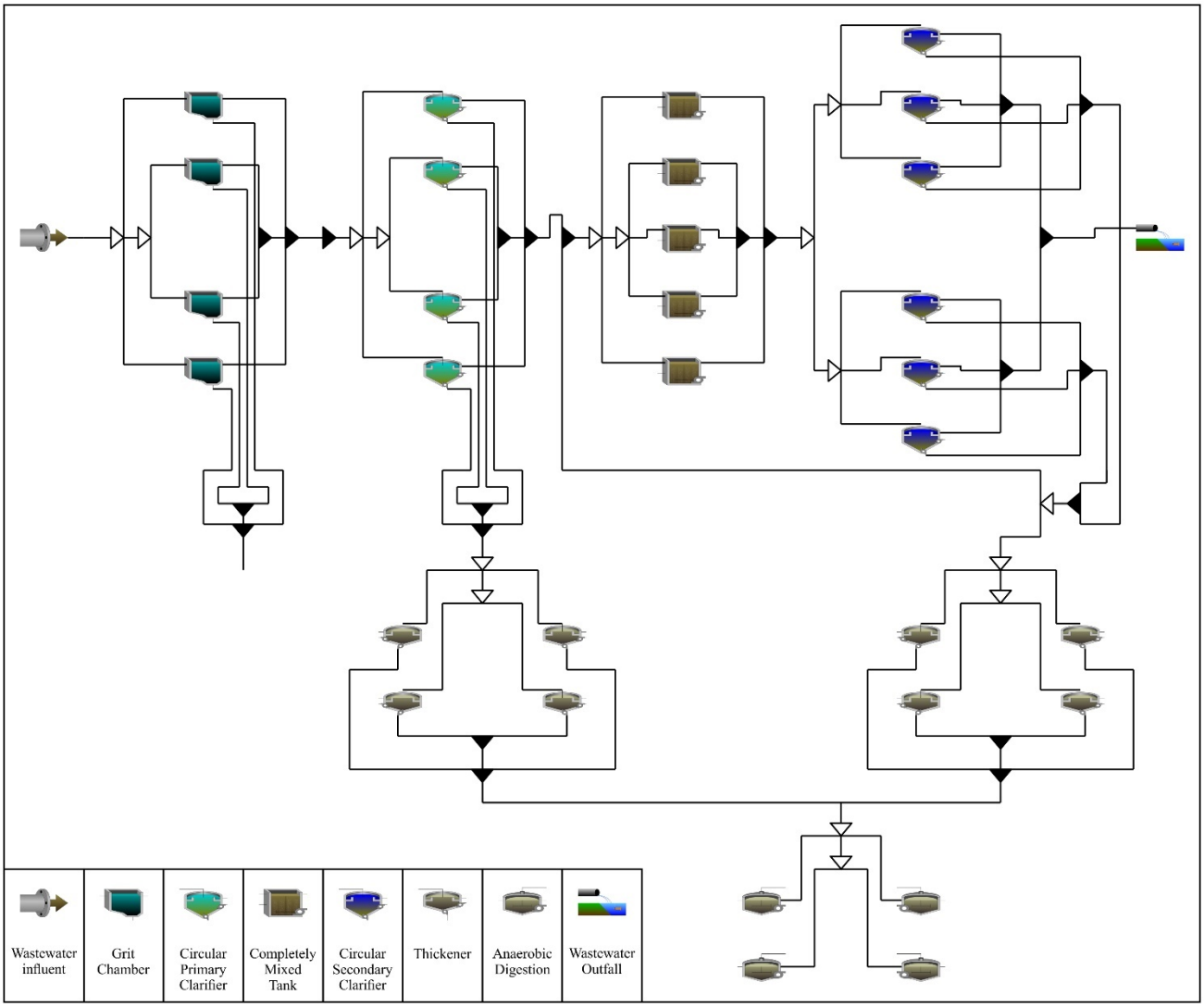

Figure 2. *Flow diagram of WWTP processes modeled in GPS-X software.*

The flow diagram was saved with the GPS-X software file format of the layout (.LYT) extension. After this, model selection was made for processes in the plant. For grit chambers, the sand amount produced per meter cube volume was determined using the standard *empiric* model in the software. It was assumed that no biological reaction occurred in the circular primary and secondary clarifiers, so the *simple1d* model was chosen. The completely-mixed aeration tanks were modeled using the ASM1 model. The sludge removed from the clarifying tanks was transferred to separate sludge thickener tanks for the circular primary and secondary clarifiers. For thickener tanks in sludge removal, the standard model in the software of the *simple1d* model was used. The water coming from the sludge thickener was recycled into the circular primary clarifier and aeration tanks. The target was to use thickened sludge to provide gas production by sending it to anaerobic digesters using the *basic* model [22]. As the software allows at most 5 distribution and collection structures, 2 and 3 distribution and collection structures were used together before and after the circular secondary clarifier, as seen in Figure 2. In the next stage, the physical features of the units in the plant like volumes, depths, surface areas and heights were input using suitable models for the WWTP in the GPS-X software. Later, information like the influent and reactor operating temperature, elevation of the plant above sea level and open-air pressure, types of precipitators, motor power of mixers used in the completely-mixed aeration tank, aeration method, amount of air used, biological treatment recycle sludge flow rate, and sludge flow rates discharged from clarifiers and sludge thickeners was entered into the relevant data entry sections. The BOD-based definitions in the carbon-nitrogen (cnlib) library and a variety of stochiometric coefficients for influent used in the ASM1 model were determined as shown in Table 7 using Influent Advisor, assisting software for the GPS-X program.

Table 7. *Basic user inputs of Influent Advisor (Library: cnlib).*

Parameter (User input)	Unit	Value
Readily biodegradable fraction of total COD (frss)	-	0.31
Ammonium fraction of soluble TKN (frsnh)	-	0.65
Ratio of particulate organic nitrogen to total organic nitrogen (fnd)	-	0.90
Ratio of particulate COD to VSS (icv)	g COD g $VMLSS^{-1}$	2.20
Ratio of volatile suspended solids to TSS (ivt)	g VSS g TSS^{-1}	0.60
Ratio of BOD_5 to ultimate BOD (fbod)	-	0.66
Nitrogen content of active biomass (ixbn)	g N g COD^{-1}	0.086
Nitrogen content of endogenous/inert mass (ixun)	g N g COD^{-1}	0.060

The wastewater entering the system comes to the completely-mixed aeration tanks after grit chambers and circular primary clarifier. Each of the 5 completely-mixed aeration tanks where biodegradation occurs are given 12000 m^3 h^{-1} air through diffusors. It is assumed that sludge is not discharged from the completely-mixed aeration tanks. After 7 hours in the completely-mixed aeration tanks, collection and distribution structures are used to send water to the circular secondary clarifier tank and after being left for a duration, the water is discharged into the receiving environment. The precipitated sludge is sent back to the completely-mixed aeration tanks with 0.75 recycle rate. A total of 2700 m^3 day^{-1} sludge is discharged from the circular secondary clarifier and sent to the sludge thickeners. The separately condensed sludge from the primary and secondary sludge thickeners is combined and transferred to anaerobic digesters with the aim of gas production. The WWTP simulation was created using the *Build* command which is the review process in the GPS-X software. Later the simulation was observed on the screen and a variety of scenarios are run.

3. Results and Discussion

3.1. Effect of wastewater at different temperatures on effluent

The plant operating under stable conditions had COD, BOD and NH_4 concentrations calculated for influent with temperatures 10°C and 20°C using the GPS-X software. Figure 3 shows the treatment efficiency obtained according to the ASM1 model. As the dissolved oxygen concentration was inversely correlated with temperature and due to the reduction in active biomass concentration, at 20°C the dissolved oxygen concentration was 0.7 mg L^{-1}, while at 10°C the dissolved oxygen concentration reached 6 mg L^{-1}. Additionally, the MLSS concentration in effluent was calculated as 14.83 mg L^{-1}. According to the model, MLSS is a composite parameter encompassing X_S, X_I, X_{BH} and X_{BA} components. The MLSS value is a parameter sensitive to the amount of sludge discharged from the circular secondary clarifier tank, surface load changes and hold time changes. The effluent from the plant operated at 20°C had COD concentration 48.51 mg L^{-1} and BOD concentration 6.55 mg L^{-1}. The dissolved COD concentration, calculated as 34.87 mg L^{-1}, is a composite parameter comprising the combination of the soluble inert substrate and soluble readily degradable substrate. The 30 mg L^{-1} inert portion in the influent leaves the system without any change. Theoretically, the dissolved COD value is expected to be the same as S_i. However, as a result of biochemical activity in the system, the expected readily degradable S_S value is found in effluent, though only partly. The NH_4 concentration in output water was 0.3 mg L^{-1} under stable conditions, while the NO_3 concentration was calculated as 18.2 mg L^{-1}. The nitrate and nitrite concentrations occurring as a result of the nitrification process are related to the nitrifying microorganism concentration in the completely-mixed aeration tank and dissolved oxygen concentration. According to the dissolved oxygen concentration calculated by the model for the completely-mixed aeration tank, it appears nitrification occurred. However, for nitrification to occur more efficiently, the dissolved oxygen concentration should not be lower than 1.5 mg L^{-1}. The total nitrogen concentration in effluent, comprising ammonium, nitrate, soluble organic and inert nitrogen, was calculated as 20.2 mg L^{-1}. As only nitrification occurred in the system, the nitrate concentration increased. Nitrate removal may occur with denitrification and the quality of the discharge water may be increased.

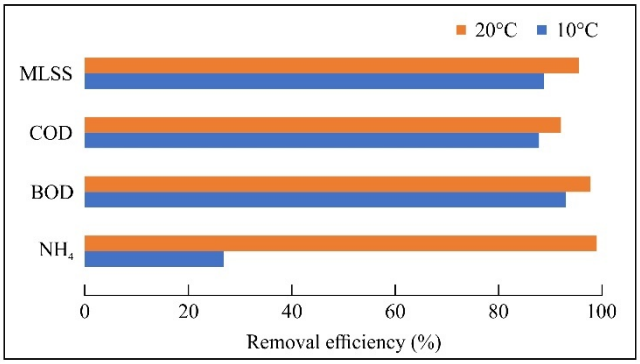

Figure 3. *Effect of wastewater temperature on effluent quality.*

The WWTP operated under stable conditions for 10 days at 10°C had mean values in effluent of 75 mg L^{-1} for COD, 21.83 mg L^{-1} for BOD and 38 mg L^{-1} for MLSS. When the concentration of wastewater entering the completely-mixed aeration tank is noted, it is possible to mention biological activity of heterotrophs, though slow. However, when the obtained results are compared with effluent concentrations at 20°C, a 30% reduction in removal of carbonaceous material is observed. As the majority of the COD concentration comprises the inert portion, negligible rates (nearly 1%) of variation were observed in COD. The value of 26.13 mg L^{-1} obtained for NH_4 shows the nitrification process reached the point of stopping. As nitrifying autotrophic microorganisms are more sensitive to environmental conditions, especially, it is not always possible for nitrification to occur at operating conditions lower than 10°C and higher than 50°C [25]. When the simulation results are investigated, it is possible to state that efficient carbon and nitrogen removal will not occur in the biological treatment units in December-January. With the aim of minimizing the effect of these temperature changes in the winter month on the ASP, completely-mixed aeration tanks may be constructed with the top enclosed.

3.2. Effect of controlling DO concentration with PID on effluent

The dissolved oxygen (DO) concentration is among the determinative parameters for carbonaceous material removal and the nitrification process in completely-mixed aeration tanks. DO concentration should be controlled using automatic control systems to balance sudden flow increases and changes in influent concentration. One of the features of the GPS-X software is proportional-integral-derivative (PID) control used to keep the dissolved oxygen level in the completely-mixed aeration tanks at 1.5 mg L^{-1}. The effect of keeping the DO concentration at 1.5 mg L^{-1} on effluent COD, BOD and NH_4 removal efficiency is shown in Figure 4.

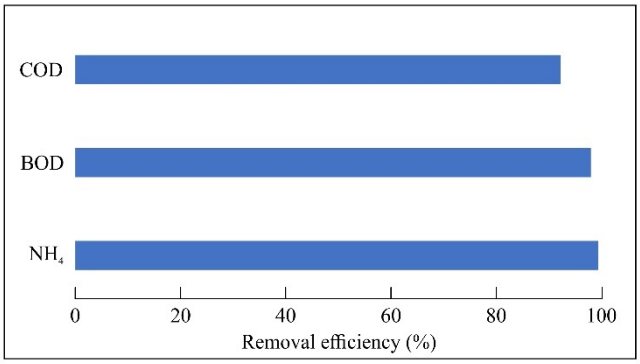

Figure 4. *Effect of PID-controlled dissolved oxygen (DO) concentration on effluent quality.*

As a result of the simulation operated under stable conditions with DO concentration fixed to 1.5 mg L^{-1}, COD was calculated as 48.37 mg L^{-1}, BOD 6.46 mg L^{-1} and NH_4 0.22 mg L^{-1}. Comparing these results with the COD and BOD values calculated using the criteria determined for plant design, it appears that 12000 m^3 h^{-1} air flow rate is sufficient for carbonaceous matter removal. The nitrate concentration was calculated as 25.72 mg L^{-1}. With PID control, the nitrification efficiency appeared to increase by 30%. This situation reveals the need to increase the amount of air for more efficient nitrification [26]. To be able to keep the DO concentration in the aeration tank at 1.5 mg L^{-1}, it was calculated that nearly 14000–15000 m^3 h^{-1} of air should be used.

4. Conclusion

It is necessary to design large-scale wastewater treatment plants to treat significant amounts of wastewater before discharge into the receiving environment. Most of the time, the treatment efficiency of these plants cannot be predicted before operation. Treatment models assist in estimating the treatment performance before building large-scale treatment plants. The ASM1 model is a successful model for prediction of carbonaceous and nitrogenous material removal from domestic wastewater especially. Additionally, it ensures determination of some operating conditions. Using a model created with GPS-X software, the typical parameters for domestic wastewater like suspended solids, carbon and nitrogen concentrations in the effluent from the operating plant were investigated. Later stages of the study researched the effect of dissolved oxygen concentration and temperature parameters. The results obtained in this study are given below:

- The effluent from the plant operated at 20°C had values of 48.51 mg L^{-1} for COD, 34.87 mg L^{-1} for dissolved COD, 6.55 mg L^{-1} for BOD and 14.38 mg L^{-1} for MLSS.
- When values of 0.3 mg L^{-1} for NH_4 and 18.2 mg L^{-1}, for nitrate are investigated, it appears nitrification partially occurred. However, it was observed that dissolved oxygen concentration around 0.7 mg L^{-1} was inadequate for nitrification.
- Effluent from the plant operated at 10°C contained 38 mg L^{-1} MLSS, 75 mg L^{-1} COD, 21.83 mg L^{-1} BOD and 26.13 mg L^{-1} NH_4. According to the results calculated with the model, biological activity slowed for heterotrophs while nitrification reached stopping point.
- Holding dissolved oxygen concentration to 1.5 mg L^{-1} using PID did not play a great role in carbonaceous matter removal; however, it was identified to cause a 30% improvement for the nitrification process. For nitrification to occur in a healthy way, it was determined to be necessary to use 14000–15000 m^3 h^{-1} air in the completely-mixed aeration tanks.

Future studies are suggested to use models encompassing phosphorus removal in addition to carbonaceous and

nitrogenous material removal. Additionally, plant treatment efficiency should be investigated in other extraordinary situations like sudden changes in flow rate, and excessive carbon and nitrogen loading, apart from temperature.

Acknowledgements

This study was prepared using data from a Master's thesis (Thesis No: 299805) by Erdinç Aladağ supervised by Alper Nuhoğlu.

Conflict of interest

There is no conflict of interest.

References

[1]. S.J. Burian, S.J. Nix, R.E. Pitt, S.R. Durrans, "Urban wastewater management in the United States: Past, present, and future", Journal of Urban Technology, 7, (2000), 33–62.

[2]. Y. Muslu, "Atıksuların arıtılması", Cilt-1, İstanbul, İTÜ Matbaası, (1996).

[3]. E. Ardern, W.T. Lockett, "Experiments on the oxidation of sewage without the aid of filters", Journal of the Society of Chemical Industry, 33, (1914), 523–539.

[4]. K.V. Gernaey, M.C. Van Loosdrecht, M. Henze, M. Lind, S.B. Jørgensen, "Activated sludge wastewater treatment plant modelling and simulation: state of the art", Environmental Modelling & Software, 19, (2004), 763–783.

[5]. S. Yıldız, O.Ö. Namal, M. Çekim, "Atık su arıtma teknolojilerindeki tarihsel gelişimler", Selçuk Üniversitesi Mühendislik, Bilim ve Teknoloji Dergisi, 1, (2013), 55–67.

[6]. R. Hreiz, M. Latifi, N. Roche, "Optimal design and operation of activated sludge processes: State-of-the-art", Chemical Engineering Journal, 281, (2015), 900–920.

[7]. Y. Liu, "Chemically reduced excess sludge production in the activated sludge process", Chemosphere, 50, (2003), 1–7.

[8]. H. Siegrist, M. Tschui, "Interpretation of experimental data with regard to the activated sludge model no. 1 and calibration of the model for municipal wastewater treatment plants", Water Science and Technology, 25, (1992), 167–183.

[9]. W. El-Shorbagy, A. Arwani, R.L. Droste, "Optimal sizing of activated sludge process with ASM3", International Journal of Civil & Environmental Engineering, 11, (2011), 19–55.

[10]. E. Aladağ, "Erzurum kenti için aktif çamur tesisi tasarımı ve modellenmesi", Atatürk Üniversitesi, Fen Bilimleri Enstitüsü, Çevre Mühendisliği Anabilim Dalı, Yüksek Lisans Tezi, Erzurum, (2011).

[11]. D. Orhon, "Evolution of the activated sludge process: the first 50 years", Journal of Chemical Technology & Biotechnology, 90, (2015), 608–640.

[12]. M. Henze, W. Gujer, T. Mino, M.C. van Loosdrecht, "Activated sludge models ASM1, ASM2, ASM2d and ASM3", IWA publishing, 2000.

[13]. M. Puteh, K. Minekawa, N. Hashimoto, Y. Kawase, "Modeling of activated sludge wastewater treatment processes", Bioprocess Engineering, 21, (1999), 249–254.

[14]. M. Nelson, H.S. Sidhu, "Analysis of the activated sludge model (no. 1)", Applied Mathematics Letters, 22, (2009), 629–635.

[15]. A. Al-Shahwan, A. Balhaddad, H. Al-Soudani, D. Nuhu, I. Abdel-Magid, "Municipal wastewater treatment plants monitoring and evaluation: Case study Dammam Metropolitan Area", Advance Research Journal of Multi-Disciplinary Discoveries, 1, (2016), 1–9.

[16]. N.D. Mu'azu, O. Alagha, I. Anil, "Systematic modeling of municipal wastewater activated sludge process and treatment plant capacity analysis using GPS-X", Sustainability, 12, (2020), 8182.

[17]. E. Aladağ, "Forecasting of particulate matter with a hybrid ARIMA model based on wavelet transformation and seasonal adjustment", Urban Climate, 39, (2021), 100930.

[18]. S.W. How, J.H. Sin, S.Y.Y. Wong, P.B. Lim, A. Mohd Aris, G.C. Ngoh, T. Shoji, T.P. Curtis, A.S.M. Chua, "Characterization of slowly-biodegradable organic compounds and hydrolysis kinetics in tropical wastewater for biological nitrogen removal", Water Science and Technology, 81, (2020), 71–80.

[19]. E. Morgenroth, R. Kommedal, P. Harremoës, "Processes and modeling of hydrolysis of particulate organic matter in aerobic wastewater treatment–a review", Water Science and Technology, 45, (2002), 25–40.

[20]. W. Gujer, M. Henze, T. Mino, M. Van Loosdrecht, "Activated sludge model No. 3", Water Science and Technology, 39, (1999), 183–193.

[21]. B. Petersen, K. Gernaey, M. Henze, P. Vanrolleghem, "Calibration of activated sludge models: A critical review of experimental designs", Biotechnology for the Environment: Wastewater Treatment and Modeling, Waste Gas Handling, (2003), 101–186.

[22]. A. Nuhoğlu, "Erzincan kenti evsel atıksularının karakterizasyonu ve atıksu arıtma tesisinin GPS-X Bilgisayar programı kullanılarak modellenmesi", Atatürk Üniversitesi, Fen Bilimleri Enstitüsü, Çevre Mühendisliği Anabilim Dalı, Doktora Tezi, Erzurum, (2000).

[23]. H. Hauduc, L. Rieger, A. Oehmen, M. Van Loosdrecht, Y. Comeau, A. Héduit, P. Vanrolleghem, S. Gillot, "Critical review of activated sludge modeling: state of process knowledge, modeling concepts, and limitations", Biotechnology and Bioengineering, 110, (2013), 24–46.

[24]. E.S.S.I. Hydromantis, "GPS-X Technical Reference", Environmental Software Solutions Inc, Hamilton, (2017).

[25]. J. Choubert, A. Marquot, A.E. Stricker, S. Gillot, Y. Racault, A. Heduit, "Maximum growth and decay rates of autotrophic biomass to simulate nitrogen removal at 10 C with municipal activated sludge plants", Water SA, 34, (2008), 71–76.

[26]. I. Jubany, J. Carrera, J. Lafuente, J.A. Baeza, "Start-up of a nitrification system with automatic control to treat highly concentrated ammonium wastewater: Experimental results and modeling", Chemical Engineering Journal, 144, (2008), 407–419.

MANAS Journal of Engineering
ISSN 1694-7398 | e-ISSN 1694-7398

Volume11, Issue 2, (2023) Pages 204-215
https://doi.org/10.51354/mjen.1312700

Response surface methodology optimization of electrode modification parameters toward hydrazine electrooxidation on Pd/MWCNT/GCE

Berdan Ulas[1, 2, *]

[1] Department of Mining Engineering, Faculty of Engineering, Van Yuzuncu Yil University, Van, Turkey, berdanulas@yyu.edu.tr, ORCID: 0000-0003-0650-0316

[2] Department of Chemical Engineering, Institute of Natural and Applied Sciences, Van Yuzuncu Yil University, Van, Turkey,

ABSTRACT

In this study, MWCNT supported Pd (Pd/MWCNT) was synthesized by $NaBH_4$ reduction method as catalyst for hydrazine electrooxidation reaction (HEOR). Characterization methods namely inductively coupled plasma mass spectrometry (ICP-MS), elemental mapping, and scanning electron microscopy with energy dispersive X-ray (SEM-EDX) were used to analyze the surface morphology and metal composition of the catalysts. The Pd/MWCNT catalyst's average particle size is estimated to be 6.35 nm based on SEM images. Glassy carbon electrode (GCE) modification parameters namely the amount of catalyst ink transferred to the GCE surface (V_s), ultrasonication time of the catalyst ink (t_u), and the drying time of the Pd/MWCNT/GCE (t_d) were optimized by using response surface methodology as 4.92 µL, 1 min and 19.52 min, respectively. Experimental specific activity value for HEOR was obtained as 7.13 mA cm^{-2} with 2.59% deviation under optimum conditions. Optimization of electrode preparation conditions is an inexpensive and facile method that could be used to improve the performance of anode catalysts for fuel cells.

ARTICLE INFO

Research article

Received: 10.06.2023
Accepted: 26.06.2023

Keywords:
response surface methodology,
hydrazine,
electrocatalyst

*Corresponding author

1. Introduction

The increasing population, accelerating industrialization, and environmental pollution have been gradually increased the need for green energy [1]. Power conversion devices based on hydrogen energy are potential technologies to meet this energy demand. Fuel cells, especially proton exchange membrane fuel cells (PEMFCs), are promising power conversion systems due to their flexible operating temperature, environmental friendliness, and high energy density [2]. However, liquid fuel cells are preferred for their ease of transportation and storage, despite PEMFCs being the most popular type of fuel cells [3]. Fuels such as methanol [4], ethanol [5], formic acid [6], and $NaBH_4$ [7] have been frequently reported for direct liquid fuel cells. Among direct liquid fuel cells, direct methanol fuel cells (DMFCs) are the closest to commercialization [8, 9]. However, DMFCs have disadvantages such as greenhouse gas formation, high fuel crossover, and anode catalyst poisoning [9, 10]. Hydrazine has high potential as a fuel for fuel cells. Despite its high toxicity, hydrazine is easily accessible, does not contain carbon, and is cost-effective, making it a good alternative to other fuels [11]. The ability to store hydrazine as a solid (hydrazone) significantly reduces the risks associated with its high toxicity [12]. Direct hydrazine fuel cells (DHFCs) are environmentally friendly power conversion devices with only nitrogen and water as emissions [13, 14]. They can compete with DMFCs in terms of power density (5.4 kWh L^{-1}) and cell voltage (1.56 V) [15]. Unlike DMFCs, DHFCs do not suffer from CO poisoning in the anode catalyst since they do not contain carbon in their structure [13, 16]. The anode, cathode, and overall reactions in DHFCs are given in equation (1-3).

$$2N_2H_4 + 8OH^- \rightarrow N_2 + 4H_2O + 8e^- \quad (1)$$

$$O_2 + 2H_2O + 4e^- \rightarrow 4OH^- \quad (2)$$

$$2N_2H_4 + O_2 \rightarrow N_2 + 4H_2O \quad (3)$$

The electrooxidation of hydrazine is an important half-reaction for DHFCs due to its high conversion efficiency and rapid kinetics in an alkaline environment [17]. The hydrazine

electrooxidation reaction (HEOR) has a voltage-lowering effect compared to the oxygen evolution reaction [18]. Therefore, the design of anode catalysts with high activity, stability, and selectivity for HEOR is a critical issue for the commercialization of DHFCs. Catalyst systems composed of relatively inexpensive transition metals such as Cu [19], Ni [20], and Co [21] have been frequently reported to exhibit high performance in alkaline environments. However, the oxide layer formed on these catalysts negatively affects the activity and stability of the catalyst system for HEOR. Precious metals such as Rh, Ru, Pd, and Pt, despite their high cost, are widely preferred as DHFC anode catalysts due to their high performance for HEOR. Additionally, the performance of electrodes prepared with catalysts significantly affects the electrochemical efficiency. Optimization of electrode preparation parameters has been previously reported by our research group to significantly increase the specific activity of a conventional anode catalyst. Optimum electrode preparation parameters for glucose electrooxidation have been determined with Pd and Pt anode catalysts, and a 1.5-fold higher specific activity has been observed compared to similar catalysts in the literature [22].

In conventional optimization methods, such as one factor at a time, the effect of an independent variable on the response is examined at constant values of other parameters. The simultaneous analysis of the effects of parameters on the response brings statistical experimental design methods such as the response surface method to the fore. The response surface method establishes a mathematical model between the investigated parameters and the response function. It also enables numerical and graphical optimization with statistical analysis of the created mathematical model. RSM has been frequently reported by researchers for optimizing adsorption conditions [23]. Due to its advantages such as revealing the interaction of parameters, reduced number of experiments and chemical amount, RSM has started to be used in other fields as well.

In this study, the Pd/MWCNT catalyst was prepared via $NaBH_4$ reduction method and characterized using scanning electron microscopy with energy dispersive X-ray spectroscopy (SEM/EDX), elemental mapping, and inductively coupled plasma mass spectrometry (ICP-MS). The glassy carbon electrode (GCE) modified with Pd/MWCNT was investigated for anode catalyst performance for HEOR, and the optimum electrode preparation conditions were determined using RSM. The optimization of electrode preparation parameters for Pd/MWCNT/GCE toward HEOR has not been reported in the literature yet. By optimizing the electrode preparation parameters of Pd/MWCNT/GCE, electrodes with lower cost and higher specific activity were obtained.

2. Materials and methods

2.1. Synthesis and characterization of Pd/MWCNT

The typical $NaBH_4$ reduction method was used to synthesis of MWCNT supported Pd [24]. First, 10 ml of distilled water were used to dissolve the analytical grade K_2PdCl_4 that was employed as a precursor. The specified amount of MWCNT was added to the solution. The $NaBH_4$ solution was then added dropwise and the mixture agitated on a magnetic stirrer for the following 2 h. After the reduction was finished, the final solution was agitated for 24 h before being filtered, washed, and dried at 80°C. SEM-EDX, elemental mapping, and ICP-MS were utilized as analytical techniques for characterization of the Pd/MWCNT. The elemental composition and morphological features of Pd/MWCNT were investigated through SEM-EDX with elemental mapping (Zeiss Sigma 300) and ICP-MS (Agilent 7800).

2.2. Electrochemical evaluation

Electrochemical experiments were performed using a CH Instrument 660E Potentiostat/Galvanostat with conventional three electrodes. A catalyst slurry was formed by dissolving 3 mg of MWCNT in 1 ml of Nafion in an ultrasonic water bath for 10 minutes in order to modify the working electrode. The glassy carbon electrode (GCE) was sprayed with the prepared catalyst slurry, and it was then dried for the identified lengths of time (t_d) at room temperature.

2.3. Response surface methodology

The GCE electrode was modified with Pd/MWCNT and the modification conditions were optimized with the RSM center composite design (CCD). The amount of catalyst ink transferred to the GCE surface, the ultrasonication time of the catalyst ink, and the drying time of the Pd/MWCNT/GCE electrode were chosen as independent variables for the modification of GCE, and are indicated by A (V_s), B (t_u), and C (t_d), respectively. The A, B, and C parameter ranges for HEOR on Pd/MWCNT/GCE and the specific activity values at the determined experimental points are presented in Table 1. The -1, 0, and +1 shown in Table 1 represent the minimum, middle, and maximum points, respectively. The experimental program proposed by Design Expert consists of 6 replicate points and 14 different points.

.

Table 2. *CCD for HEOR on Pd/MWCNT/GCE.*

Run	Factor 1 A:V_s (µL)	Factor 2 B:t_u (min)	Factor 3 C:t_d (min)	Response Specific Activity for HEOR (mA cm^{-2})
1	10 (+1)	60 (+1)	40 (+1)	39.92
2	10 (+1)	1 (-1)	1 (-1)	5.23
3	0.5 (-1)	60 (+1)	1 (-1)	7.32
4	5.25 (0)	30.5 (0)	20.5 (0)	5.12
5	0.5 (-1)	60 (+1)	40 (+1)	6.21
6	5.25 (0)	60 (+1)	20.5 (0)	20.65
7	10 (+1)	1 (-1)	40 (+1)	11.40
8	10 (+1)	30.5 (0)	20.5 (0)	4.18
9	10 (+1)	60 (+1)	1 (-1)	9.33
10	5.25 (0)	30.5 (0)	20.5 (0)	4.83
11	5.25 (0)	30.5 (0)	1 (-1)	1.61
12	5.25 (0)	30.5 (0)	20.5 (0)	5.30
13	5.25 (0)	30.5 (0)	20.5 (0)	5.18
14	5.25 (0)	30.5 (0)	40 (+1)	3.79
15	0.5 (-1)	1 (-1)	1 (-1)	9.05
16	5.25 (0)	30.5 (0)	20.5 (0)	4.55
17	5.25 (0)	30.5 (0)	20.5 (0)	3.97
18	5.25 (0)	1 (-1)	20.5 (0)	1.23
19	0.5 (-1)	30.5 (0)	20.5 (0)	1.09
20	0.5 (-1)	1 (-1)	40 (+1)	5.27

3. Results and discussion

3.1. Physical characterization

The surface morphology of Pd/MWCNT was examined by SEM and is shown in Figure 1. From Figure 1a and b the network of the CNT is clearly visible. It was determined from Figure 1c and d that Pd did not agglomerate on the CNT surface. It was also observed that Pd nanoparticles adhered to both the inner and outer walls of the CNT (Figure 1e and f). The mean particle size of Pd nanoparticles in SEM images was determined as 6.35 nm with ImageJ software. Elemental mapping analysis to Pd/MWCNT was performed to confirm the distribution of Pd nanoparticles. C, O, Pd, and overlay elemental mapping images of Pd/MWCNT are shown in Figure 2. Since the metal ratio of Pd/MWCNT to the support material is 10% by weight, it is clearly seen that carbon is more dominant than other elements in the elemental mapping images (Figure 2a). Furthermore, the oxygen detected in the catalyst structure was attributed to the presence of PdO, since K_2PdCl_4 cannot be fully reduced with $NaBH_4$ and Pd is easily oxidized (Figure 2b) [25]. It was observed from Figure 2c that the Pd nanoparticles were homogeneously dispersed on the MWCNT. Also from the overlay images of all elements, it is more clearly seen as the elements are uniformly distributed on MWCNT (Figure 2d). Pd, O and C peaks were detected in the EDX spectrum of Pd/MWCNT. Carbon exhibited a very high peak intensity, while the intensity of the oxygen peak was very weak. In this context, the EDX spectrum also support the elemental mapping results. ICP-MS results of Pd/MWCNT were determined as 11.2:100 of Pd:MWCNT by mass. The closeness of the obtained metal ratio to the targeted ratio indicates that the synthesis was successful.

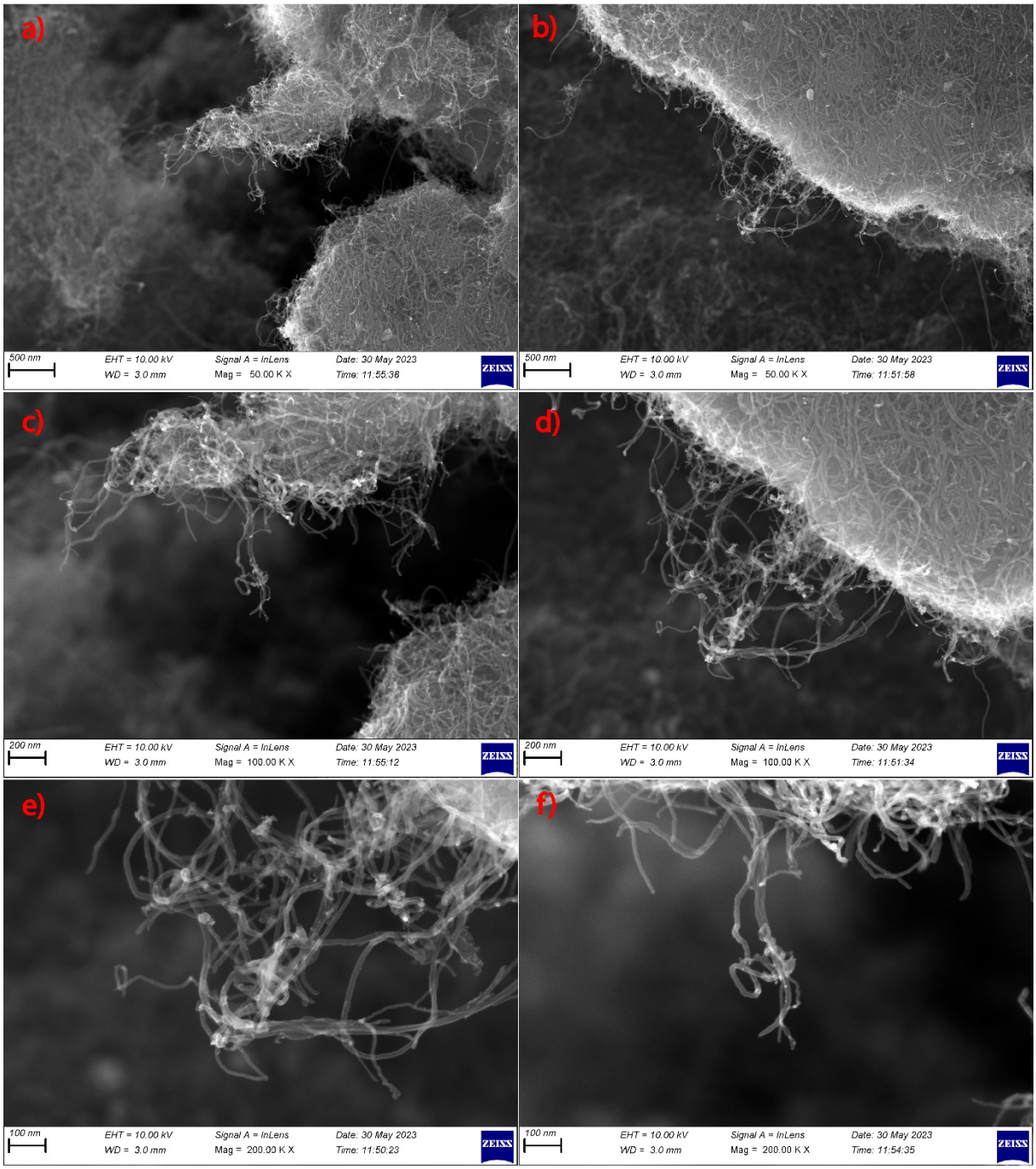

Figure 1. *SEM images of Pd/MWCNT.*

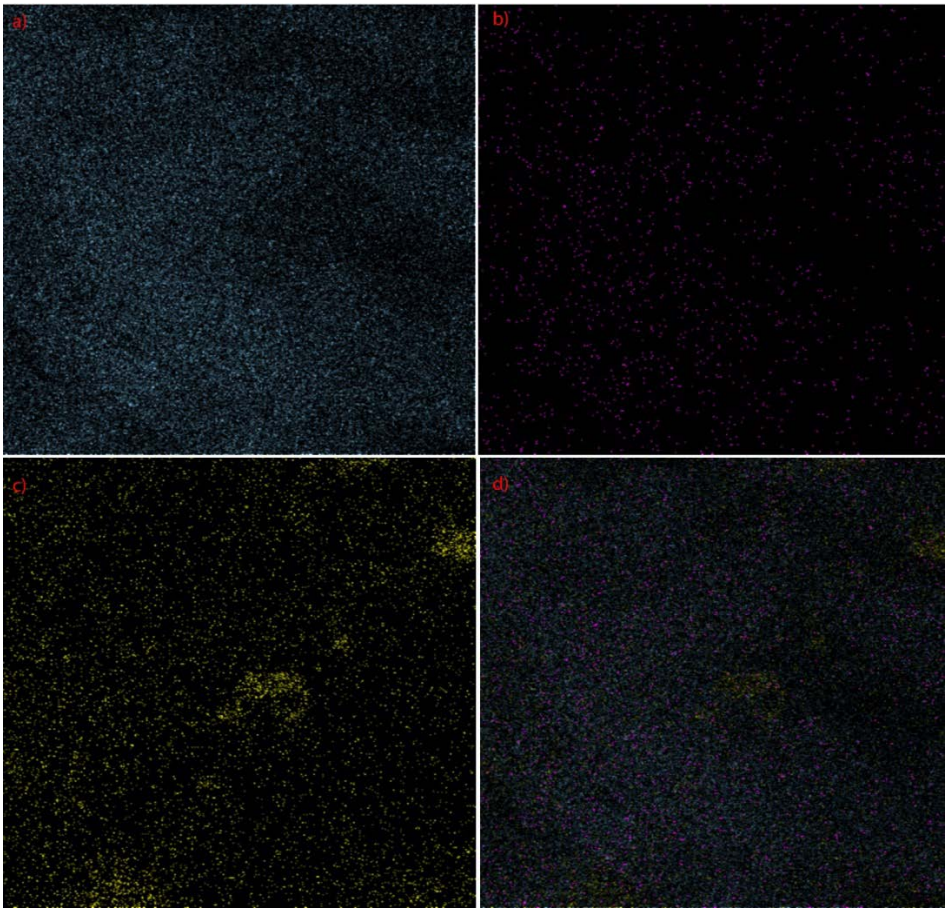

Figure 2. *SEM images of Pd/MWCNT.*

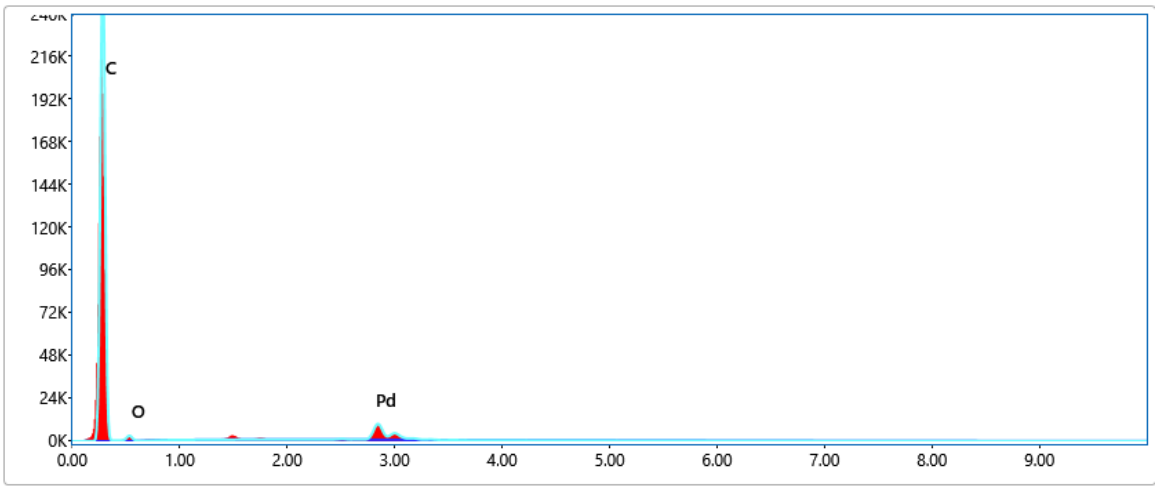

Figure 3. *EDX spectrum for Pd/MWCNT.*

3.2. Response surface methodology

The specific activities for HEOR of the Pd/MWCNT/GCE electrode prepared at the V_s, t_u and t_d values given in Table 1 were determined in 0.1 M KOH + 0.02 M N_2H_2 solutions. Voltammograms of each experimental set are given in Figure 4. The

obtained results were statistically analyzed with the Design Expert software.

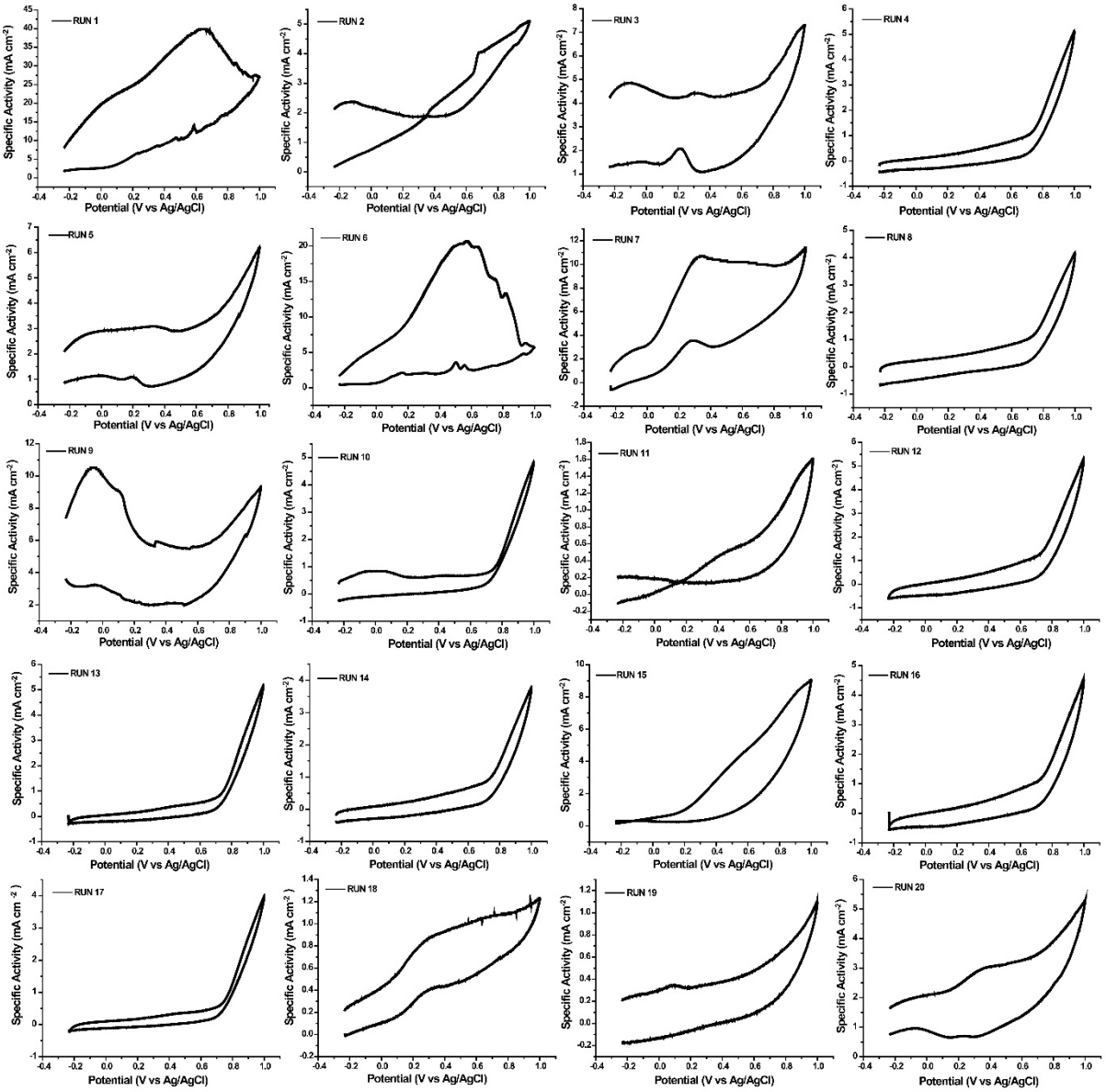

Figure 4. *CV profiles for CCD.*

The model with which the experimental results were compatible was investigated with the Design Expert software and is given in Tables 2 and 3. Table 2 exhibites that the lack of fit tests of linear, 2FI and quadratic models suggested by the software are statistically significant, while the cubic model is aliased. In this case, it is understood that cubic model terms cannot be estimated individually and the cubic model should be used as a summary of these combined effects. According to the lack fit test results, except for the aliased cubic model, the lowest F value is the quadratic model with 124.72. As can be seen from Table 3, the R^2 values of the cubic, quadratic, 2FI and linear models were obtained as 0.991, 0.893, 0692 and 0.38, respectively. Because of the aliased model terms it contains, the highest correlation coefficient is reported for the cubic model. In addition, the quadratic model showed the lowest standard deviation and PRESS values (excluding linear model) with 3.927 and 2072.65, respectively. When the statistical parameters reported for the models suggested by the software are evaluated together, it is concluded that the model with the highest predictive performance is the quadratic model.

Table 2. *Lack of fit tests for suggested models.*

Source	Sum of Squares	df	Mean Square	F Value	p-value Prob > F	
Linear	891.17	11	81.01	330.18	< 0.0001	
2FI	442.73	8	55.34	225.54	< 0.0001	
Quadratic	153.01	5	30.60	124.72	< 0.0001	Suggested
Cubic	11.308	1	11.31	46.087	0.0011	Aliased
Pure Error	1.2268	5	0.245			

Table 3. *Model summary statistics for HEOR on Pd/MWCNT/GCE.*

Source	Std. Dev.	R-Squared	Adjusted R-Squared	PRESS	
Linear	7.468	0.38	0.264	1858.68	
2FI	5.844	0.692	0.549	2978.18	
Quadratic	3.927	0.893	0.796	2072.65	Suggested
Cubic	1.445	0.991	0.972	13896.1	Aliased

The proposed quadratic model in terms of actual values and coded for HEOR on Pd/MWCNT/GCE is shown in Eqn. (3-4). Analysis of variance (ANOVA) was performed for the proposed model and is given in Table 4. It is known that a p value less than 0.05 in the 95% confidence interval indicates that the relevant model term is statistically significant. Accordingly, it is seen that the suggested model terms A, B, C, AB, AC, BC and B^2 are statistically significant. A^2 and C^2 terms were not statistically significant with p values of 0.8897 and 0.9106. However, the terms A^2 and C^2 were not removed from the model, as it was concluded that the model improved the predictive performance [23].

Specific Activity for HEOR =

$$+4.08+4.11*A+5.12*B+3.41*C+4.18*A*B+5.21*A*C+3.39*B*C-0.34*A^2+7.97*B^2-0.27*C^2 \quad (3)$$

Specific activity for HEOR =

$$+12.97337-(1.03953*V_s)-(0.66207*t_u)-(0.27075*t_d)+(0.029819*V_s*t_u)+(0.056216*V_s*t_d)+(5.89115E-003*t_u*t_d)-(0.014935*V_s2)+(0.00915484*t_u2)-(0.000717167*t_d2) \quad (4)$$

Table 4. *ANOVA table for HEOR on Pd/MWCNT/GCE.*

Source	**Sum of Squares**	**df**	**Mean Square**	**F Value**	**p-value Prob > F**	
Model	1285.75	9	142.86	9.26	0.0009	significant
A-V_s	169.03	1	169.03	10.96	0.0079	
B- t_u	262.56	1	262.56	17.02	0.0021	
C- t_d	115.99	1	115.99	7.52	0.0207	
AB	139.67	1	139.67	9.06	0.0131	
AC	216.9	1	216.9	14.06	0.0038	
BC	91.88	1	91.88	5.96	0.0348	
A^2	0.31	1	0.31	0.02	0.8897	
B^2	174.55	1	174.55	11.32	0.0072	
C^2	0.2	1	0.2	0.013	0.9106	
Residual	154.24	10	15.42			

Pure Error	1.23	5	0.25
Cor Total	1439.99	19	

In Figure 5, the compatibility of the quadratic model and experimental data is discussed. The distribution of model data relative to the actual data for HEOR on Pd/MWCNT is shown in Figure 5. Although very few of the experimental points expected to be dispersed around the diagonal deviated, it was observed that the majority of them dispersed around the diagonal. Figure 5b shows the distribution of errors. It has been determined that the errors are distributed around the standard line. The random distribution of errors indicates that there is no systematic error. The plot of the residuals against the predicted values is given in Figure 5c. The random distribution between the boundary lines determined by the software is explained by the non-constant variance. The plot of the residues according to the experiment number is exhibited in Figure 5d. It has been determined that the graph obtained as a result of combining the residual values with a line does not show a recurrent trend. Therefore, it was concluded that the residuals were not caused by a systematic error. Model validation graphs and ANOVA test results show that the proposed quadratic model is a good predictor.

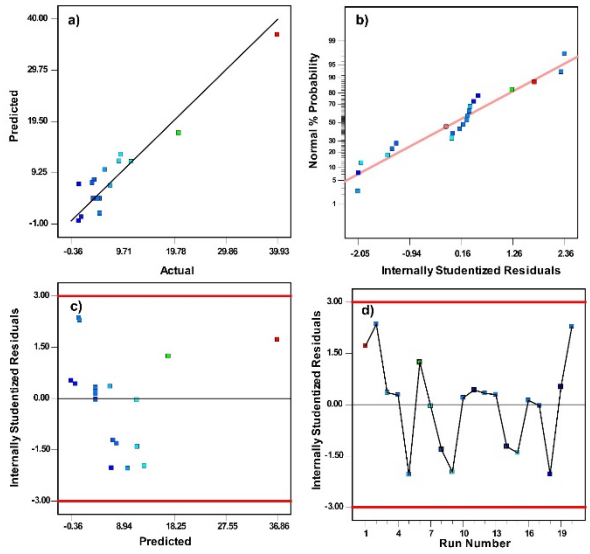

Figure 4. *Model validation plots for HEOR on Pd/MWCNT/GCE.*

In Figure 6, response surface plots of V_s, t_u and t_d are presented. The binary interactions of t_u and V_s are shown in Figure 6a. When the t_u value was increased from 1 min to 30.5 min, a decrease of 1.627 mA cm^{-2} in the specific activity was observed (V_s=5.25 µL and t_d=20.5 min). After the t_u value of 30.5 min, the specific activity increased sharply and reached 17.175 mA cm^{-2} (Figure 6a). At constant t_u=30.5 min and t_d=20.5 min, when V_s was increased from 0.5 µL to 5.25 µL, the specific activity for HEOR increased from 1.097 mA cm^{-2} to 4.828 mA cm^{-2} (Figure 6b). After the V^s value of 5.25 µL, the specific activity gradually decreased to a value of 4.175 mA cm^{-2}. From Figure 6c, as a result of increasing t_d from 1 min to 40 min, the specific activity increased almost linearly from 0.405 mA cm^{-2} to 7.217 mA cm^{-2}.

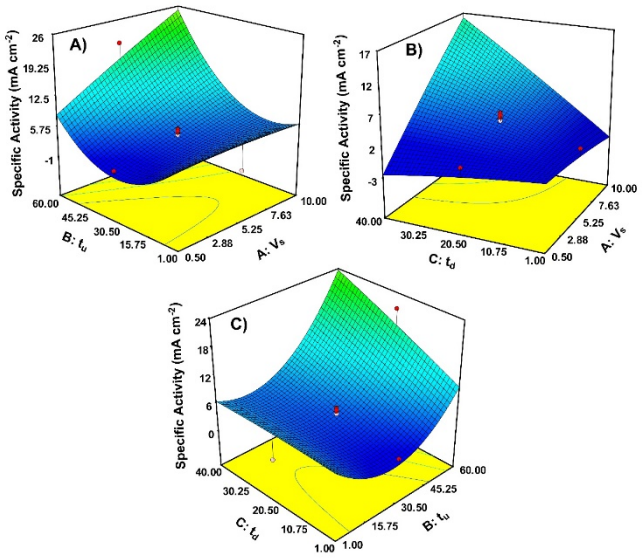

Figure 6. *Response surface plots for HEOR on Pd/MWCNT/GCE A) t_u vs V_s, B) t_d vs V_s, and C)t_d vs t_u.*

Numerical optimization was performed for HEOR on Pd/MWCNT/GCE with Design Expert software. In the optimization process, the specific activity value is maximized by minimizing V_s, t_u and t_d. While the optimum V_s, t_u and t_d values were determined as 4.92 µL, 1 min and 19.52 min, respectively, the model specific activity value was found as 6.95 mA cm^{-2}. Experimental specific activity value for HEOR was determined as 7.13 mA cm^{-2} with 2.59% deviation by CV measurements performed under optimum conditions.

The electrochemical behavior of Pd/MWCNT at optimum conditions determined by RSM is given in Figure 7. Electrochemical experiments were carried out at a scanning rate of 100 mV s^{-1} and in 0.1 M KOH+0.02 M N_2H_2 solution. Figure 7a exhibits the voltammogram of Pd/MWCNT in a 0.1 M KOH support electrolyte. In the forward scan, no electrochemical phenomena were observed between 0 V and 0.3 V, and it was concluded that this potential range is a double layer region [26]. The narrow peak observed at a potential of about 0.3 V in reverse scan is due to PdO reduction [27]. 50 cycle CV profiles of Pd/MWCNT are given in Figure 7b. Pd/MWCNT showed 7.13 mA cm^{-2} specific activity under optimum electrode preparation conditions and this specific activity decreased to 1.42 mA cm^{-2} after 50

cycles. The decrease in the activity of Pd/MWCNT could be attributed to the accumulation of intermediate compound on the electrode surface [28].

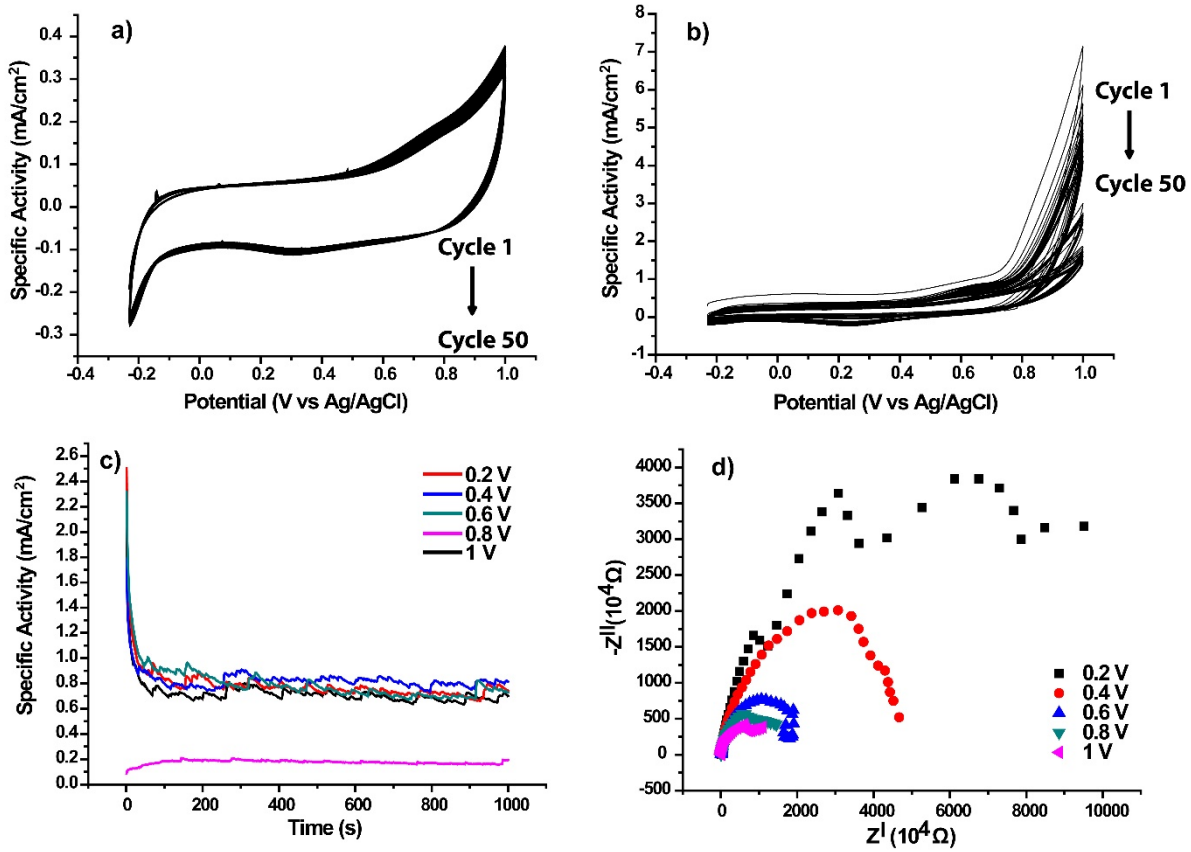

Figure 7. *a) CV in 0.1 M KOH, b) CV in 0.1 M KOH + 0.02 M N_2H_2, c) CA curves at 0.2-1 V in 0.1 M KOH + 0.02 M N_2H_2, and d) EIS profiles at 0.2-1 V in 0.1 M KOH + 0.02 M N_2H_2.*

Chronoamperometric curves of Pd/MWCNT at 0.2, 0.4, 0.6, 0.8, and 1 V potentials are presented in Figure 7c. Except for the CA curve at 0.8 V potential, all CA profiles are similar to each other. Pd/MWCNT exhibited good stability over 1000 s despite fluctuations in current. EIS curves of Pd/MWCNT at varying potentials are given in Figure 7d. It is known that as the diameter of the EIS curves decreases, the charge transfer resistance decreases and the electrocatalytic activity increases [29]. In this direction, as can be seen from Figure 7d, the electrocatalytic activity of Pd/MWCNT increased as the applied potential increased. In this case, it was concluded that the HEOR mechanism on Pd/MWCNT/GCE is predominantly driven by charge transfer kinetics.

4. Conclusion

In this study, GCE was modified with Pd/MWCNT catalysts synthesized by the $NaBH_4$ reduction method and its performance as a catalyst for HEOR was investigated. From the SEM-EDX results, it was determined that the average particle size of Pd/MWCNT was 6.35 nm. Elemental mapping results show that Pd is homogeneously distributed on MWCNT, and the metal composition of Pd/MWCNT was determined as 11.2% by ICP-MS. Optimum electrode preparation conditions for HEOR on Pd/MWCNT/GCE were determined by RSM as 4.92 µL V_s, 1 min t_u, and 19.52 min t_d. Under optimum conditions, experimental specific activity value for HEOR was obtained as 7.13 mA cm^{-2} with 2.59% deviation. The R^2 value of the proposed quadratic model for HEOR on Pd/MWCNT/GCE was determined as 0.893, and the model was found to be statistically significant in according to the ANOVA test. This study clearly revealed that the use of optimization methods for the electrode preparation stage is very important in terms of increasing the specific activity. It is concluded that conducting electrode optimization researches for future designed catalysts will bring cheaper, stable and active catalysts to the literature.

References

[1]. Su, M., Wang, Q., Li, R., Wang, L. "Per Capita Renewable Energy Consumption in 116 Countries: The Effects of Urbanization, Industrialization, Gdp, Aging, and Trade Openness", Energy, 254, (2022), 124289; Li, W., Yu, X., Hu, N., Huang, F., Wang, J., Peng, Q. "Study on the Relationship between Fossil Energy Consumption and Carbon Emission in Sichuan Province", Energy Reports, 8, (2022), 53-62.

[2]. Nguyen, H. Q., Shabani, B. "Proton Exchange Membrane Fuel Cells Heat Recovery Opportunities for Combined Heating/Cooling and Power Applications", Energy Conversion Management, 204, (2020), 112328; Jamil, A., Rafiq, S., Iqbal, T., Khan, H. A. A., Khan, H. M., Azeem, B., Mustafa, M., Hanbazazah, A. S. "Current Status and Future Perspectives of Proton Exchange Membranes for Hydrogen Fuel Cells", Chemosphere, (2022), 135204; Yeetsorn, R., Maiket, Y., Kaewmanee, W. "The Observation of Supercapacitor Effects on Pemfc–Supercapacitor Hybridization Performance through Voltage Degradation and Electrochemical Processes", RSC advances, 10, (2020), 13100-13111.

[3]. Wan, Z., Tao, Y., Shao, J., Zhang, Y., You, H. "Ammonia as an Effective Hydrogen Carrier and a Clean Fuel for Solid Oxide Fuel Cells", Energy Conversion Management, 228, (2021), 113729; Li, M., Bai, Y., Zhang, C., Song, Y., Jiang, S., Grouset, D., Zhang, M. "Review on the Research of Hydrogen Storage System Fast Refueling in Fuel Cell Vehicle", International Journal of Hydrogen Energy, 44, (2019), 10677-10693.

[4]. Ulas, B., Caglar, A., Kivrak, A., Kivrak, H. "Atomic Molar Ratio Optimization of Carbon Nanotube Supported Pdauco Catalysts for Ethylene Glycol and Methanol Electrooxidation in Alkaline Media", Chemical Papers, 73, (2019), 425-434; Zhao, F., Zheng, L., Yuan, Q., Yang, X., Zhang, Q., Xu, H., Guo, Y., Yang, S., Zhou, Z., Gu, L. "Ultrathin Pdaubite Nanosheets as High-Performance Oxygen Reduction Catalysts for a Direct Methanol Fuel Cell Device", Advanced Materials, 33, (2021), 2103383.

[5]. Zheng, Y., Wan, X., Cheng, X., Cheng, K., Dai, Z., Liu, Z. "Advanced Catalytic Materials for Ethanol Oxidation in Direct Ethanol Fuel Cells", Catalysts, 10, (2020), 166; Wang, K., Wang, F., Zhao, Y., Zhang, W. "Surface-Tailored Ptpdcu Ultrathin Nanowires as Advanced Electrocatalysts for Ethanol Oxidation and Oxygen Reduction Reaction in Direct Ethanol Fuel Cell", Journal of Energy Chemistry, 52, (2021), 251-261.

[6]. Caglar, A., Ulas, B., Cogenli, M. S., Yurtcan, A. B., Kivrak, H. "Synthesis and Characterization of Co, Zn, Mn, V Modified Pd Formic Acid Fuel Cell Anode Catalysts", Journal of Electroanalytical Chemistry, 850, (2019), 113402; Ulas, B., Kivrak, A., Aktas, N., Kivrak, H. "Carbon Monoxide and Formic Acid Electrooxidation Study on Au Decorated Pd Catalysts Prepared Via Microwave Assisted Polyol Method", Fullerenes, Nanotubes Carbon Nanostructures, 27, (2019), 545-552.

[7]. Kaya, S., Yilmaz, Y., Er, O. F., Alpaslan, D., Ulas, B., Dudu, T. E., Kivrak, H. "Highly Active Rupd Bimetallic Catalysts for Sodium Borohydride Electrooxidation and Hydrolysis", Journal of Electronic Materials, 51, (2022), 403-411; Ulas, B., Alpaslan, D., Yilmaz, Y., Dudu, T. E., Er, O. F., Kivrak, H. "Disentangling the Enhanced Catalytic Activity on Ga Modified Ru Surfaces for Sodium Borohydride Electrooxidation", Surfaces Interfaces, 23, (2021), 100999.

[8]. Martinaiou, I., Videla, A. H. M., Weidler, N., Kübler, M., Wallace, W. D. Z., Paul, S., Wagner, S., Shahraei, A., Stark, R. W., Specchia, S. "Activity and Degradation Study of an Fe-Nc Catalyst for Orr in Direct Methanol Fuel Cell (Dmfc)", Applied Catalysis B: Environmental, 262, (2020), 118217; Ulas, B., Yagizatli, Y., Demir-Kivrak, H. (2022) Metal-Free Catalysts for Fuel Cell Applications, In *Carbon-Based Metal Free Catalysts*, pp 67-109, Elsevier.

[9]. Osman, S. H., Kamarudin, S. K., Basri, S., A. Karim, N. "Three-Dimensional Graphene Aerogel Supported on Efficient Anode Electrocatalyst for Methanol Electrooxidation in Acid Media", Catalysts, 13, (2023), 879.

[10]. Fadzillah, D., Kamarudin, S., Zainoodin, M., Masdar, M. "Critical Challenges in the System Development of Direct Alcohol Fuel Cells as Portable Power Supplies: An Overview", International Journal of Hydrogen Energy, 44, (2019), 3031-3054; Zakaria, Z., Kamarudin, S. K., Abd Wahid, K. A., Hassan, S. H. A. "The Progress of Fuel Cell for Malaysian Residential Consumption: Energy Status and Prospects to Introduction as a Renewable Power Generation System", Renewable Sustainable Energy Reviews, 144, (2021), 110984.

[11]. Zhang, Z., Tang, P., Wen, H., Wang, P. "Bicontinuous Nanoporous Ni-Fe Alloy as a Highly Active Catalyst for Hydrazine Electrooxidation", Journal of Alloys Compounds, 906, (2022), 164370; Askari, M. B., Salarizadeh, P., Beitollahi, H., Tajik, S., Eshghi, A., Azizi, S. "Electro-Oxidation of Hydrazine on Nife2o4-Rgo as a High-Performance Nano-Electrocatalyst in Alkaline Media", Materials Chemistry Physics, 275, (2022), 125313.

[12]. Luo, L., Cheng, J., Chen, S., Zhang, P., Chen, S., Tang, Z., Zeng, R., Xu, M., Hao, Y. "A near-Infrared Ratiometric Fluorescent Probe for Hydrazine and Its Application for Gaseous Sensing and Cell Imaging", Spectrochimica Acta Part A: Molecular Biomolecular Spectroscopy, 296, (2023), 122692.

[13]. Hosseini, M. G., Abdolmaleki, M., Daneshvari-Esfahlan, V. "Fabrication and Evaluation of the Performance of Co/Coniznag Nanoporous Structures as a Good Candidate for Using as Anode Catalyst in a Hydrazine Fuel Cell", Materials Technology, 34, (2019), 697-703.

[14]. Liu, W., Xie, J., Guo, Y., Lou, S., Gao, L., Tang, B. "Sulfurization-Induced Edge Amorphization in Copper–Nickel–Cobalt Layered Double Hydroxide Nanosheets Promoting Hydrazine Electro-Oxidation", Journal of Materials Chemistry A, 7, (2019), 24437-24444.

[15]. Feng, Z., Li, D., Wang, L., Sun, Q., Lu, P., Xing, P., An, M. "In Situ Grown Nanosheet Nizn Alloy on Ni Foam for High Performance Hydrazine Electrooxidation", Electrochimica Acta, 304, (2019), 275-281; Hwang, H., Hong, S., Kim, D.-H., Kang, M.-S., Park, J.-S., Uhm, S., Lee, J. "Optimistic Performance of Carbon-Free Hydrazine Fuel Cells Based on Controlled Electrode Structure and Water Management", Journal of Energy Chemistry, 51, (2020), 175-181.

[16]. Balčiūnaitė, A., Budrytė, E., Vaičiūnienė, J., Niaura, G., Kruusenberg, I., Kaare, K., Volperts, A., Dobele, G., Zurins, A., Tamašauskaitė-Tamašiūnaitė, L. "One-Pot Synthesis of Nitrogen-Doped Carbon Supported Mn-Co Nanoparticles for Hydrazine Oxidation", ECS Transactions, 97, (2020), 593.

[17]. Feng, Z., Zhang, H., Gao, B., Lu, P., Li, D., Xing, P. "Ni–Zn Nanosheet Anchored on Rgo as Bifunctional Electrocatalyst for Efficient Alkaline Water-to-Hydrogen Conversion Via Hydrazine Electrolysis", International Journal of Hydrogen Energy, 45, (2020), 19335-19343; Wang, T., Cao, X., Jiao, L. "Progress in Hydrogen Production Coupled with Electrochemical Oxidation of Small Molecules", Angewandte Chemie International Edition, (2022), e202213328.

[18]. Liu, X., Han, Y., Guo, Y., Zhao, X., Pan, D., Li, K., Wen, Z. "Electrochemical Hydrogen Generation by Oxygen Evolution Reaction-Alternative Anodic Oxidation Reactions", Advanced Energy Sustainability Research, 3, (2022), 2200005.

[19]. Crisafulli, R., de Paula, D. F., Zignani, S. C., Spadaro, L., Palella, A., Boninelli, S., Dias, J. A., Linares, J. J. "Promoting Effect of Cu on Pd Applied to the Hydrazine Electro-Oxidation and Direct Hydrazine Fuel Cells", Catalysts, 12, (2022), 1639; Wang, W., Wang, Y., Liu, S., Yahia, M., Dong, Y., Lei, Z. "Carbon-Supported Phosphatized Cuni Nanoparticle Catalysts for Hydrazine Electrooxidation", International Journal of Hydrogen Energy, 44, (2019), 10637-10645; Jiang, H., Wang, Z., Kannan, P., Wang, H., Wang, R., Subramanian, P., Ji, S. "Grain Boundaries of Co (Oh) 2-Ni-Cu Nanosheets on the Cotton Fabric Substrate for Stable and Efficient Electro-Oxidation of Hydrazine", International Journal of Hydrogen Energy, 44, (2019), 24591-24603.

[20]. Feng, Z., Li, D., Wang, L., Sun, Q., Lu, P., Xing, P., An, M. J. E. A. "In Situ Grown Nanosheet Nizn Alloy on Ni Foam for High Performance Hydrazine Electrooxidation", 304, (2019), 275-281; Chen, C., Wen, H., Tang, P.-P., Wang, P. "Supported Ni@ Ni2p Core–Shell Nanotube Arrays on Ni Foam for Hydrazine Electrooxidation", ACS Sustainable Chemistry Engineering, 9, (2021), 4564-4570; Wen, H., Gan, L.-Y., Dai, H.-B., Wen, X.-P., Wu, L.-S., Wu, H., Wang, P. "In Situ Grown Ni Phosphide Nanowire Array on Ni Foam as a High-Performance Catalyst for Hydrazine Electrooxidation", Applied Catalysis B: Environmental, 241, (2019), 292-298.

[21]. Li, J., Dong, C., Guo, M., Gao, W., Kang, L., Lei, F., Hao, P., Xie, J., Tang, B. "Cerium-Induced Lattice Disordering in Co-Based Nanocatalysts Promoting the Hydrazine Electro-Oxidation Behavior", Chemical Communications, 58, (2022), 6845-6848; Feng, G., An, L., Li, B., Zuo, Y., Song, J., Ning, F., Jiang, N., Cheng, X., Zhang, Y., Xia, D. "Atomically Ordered Non-Precious Co3ta Intermetallic Nanoparticles as High-Performance Catalysts for Hydrazine Electrooxidation", Nature Communications, 10, (2019), 4514; Firdous, N., Janjua, N. K. "Coptx/Γ-Al2o3 Bimetallic Nanoalloys as Promising Catalysts for Hydrazine Electrooxidation", Heliyon, 5, (2019), e01380.

[22]. Kaya, S., Ulas, B., Duzenli, D., Onal, I., Er, O. F., Yilmaz, Y., Tezsevin, I., Kivrak, H. "Glucose Electrooxidation Modelling Studies on Carbon Nanotube Supported Pd Catalyst with Response Surface Methodology and Density Functional Theory", Journal of Physics and Chemistry of Solids, 168, (2022), 110810; Kaya, S., Ulas, B., Er, O. F., Yılmaz, Y., Kivrak, H. "Optimization of Electrode Preperation Conditions for Enhanced Glucose Electrooxidation on Pt/Cnt by Response Surface Methodology", Journal of Electronic Materials, 51, (2022), 2971-2981.

[23]. Yılmaz, Ş. "Facile Synthesis of Surfactant-Modified Layered Double Hydroxide Magnetic Hybrid Composite and Its Application for Bisphenol a Adsorption: Statistical Optimization of Operational Variables", Surfaces and Interfaces, 32, (2022), 102171.

[24]. Ulas, B., Caglar, A., Sahin, O., Kivrak, H. "Composition Dependent Activity of Pdagni Alloy Catalysts for Formic Acid Electrooxidation", Journal of Colloid and Interface Science, 532, (2018), 47-57.

[25]. Cao, Z., Chen, H., Zhu, S., Zhang, W., Wu, X., Shan, G., Ziener, U., Qi, D. "Preparation of Janus Pd/Sio2 Nanocomposite Particles in Inverse Miniemulsions", Langmuir, 31, (2015), 4341-4350.

[26]. Lima, C. C., Rodrigues, M. V., Neto, A. F., Zanata, C. R., Pires, C. T., Costa, L. S., Solla-Gullon, J., Fernandez, P. S. "Highly Active Ag/C Nanoparticles Containing Ultra-Low Quantities of Sub-Surface Pt for the Electrooxidation of Glycerol in Alkaline Media", Applied Catalysis B: Environmental, 279, (2020), 119369; Kopač Lautar, A., Bitenc, J., Rejec, T., Dominko, R., Filhol, J.-S., Doublet, M.-L. "Electrolyte Reactivity in the Double Layer in Mg Batteries: An Interface Potential-Dependent Dft Study", Journal of the American Chemical Society, 142, (2020), 5146-5153.

[27]. Qiu, C., Wang, S., Gao, R., Qin, J., Li, W., Wang, X., Zhai, Z., Tian, D., Song, Y. "Low-Temperature Synthesis of Pdo-Ceo2/C toward Efficient Oxygen Reduction Reaction", Materials Today Energy, 18, (2020), 100557; Kottayintavida, R., Gopalan, N. K. "Pd Modified Ni Nanowire as an Efficient Electro-Catalyst for Alcohol Oxidation Reaction", International Journal of Hydrogen Energy, 45, (2020), 8396-8404.

[28]. Hanifah, M. F. R., Jaafar, J., Othman, M., Ismail, A., Rahman, M., Yusof, N., Aziz, F. "One-Pot Synthesis of Efficient Reduced Graphene Oxide Supported Binary Pt-Pd Alloy Nanoparticles as Superior Electro-Catalyst and Its Electro-Catalytic Performance toward Methanol Electro-Oxidation Reaction in Direct Methanol Fuel Cell", Journal of Alloys Compounds, 793, (2019), 232-246; Wang, J., Sun, H.-b., Shah, S. A., Liu, C., Zhang, G.-y., Li, Z., Zhang, Q.-f., Han, M. "Palladium Nanoparticles Supported by Three-Dimensional Freestanding Electrodes for High-Performance Methanol Electro-Oxidation", International Journal of Hydrogen Energy, 45, (2020), 11089-11096.

[29]. Li, Q., Bai, A., Xue, Z., Zheng, Y., Sun, H. "Nitrogen and Sulfur Co-Doped Graphene Composite Electrode with High Electrocatalytic Activity for Vanadium Redox Flow Battery Application", Electrochimica Acta, 362, (2020), 137223.

MANAS Journal of Engineering
ISSN 1694-7398 | e-ISSN 1694-7398

Volume 11, Issue 2, (2023) Pages 216-222
https://doi.org/10.51354/mjen.1344493

Investigation of the performance of *(4-(3-iodobenzo[b]thiophen-2-yl)-N,N-dimethyllaniline* as an anode catalyst for glucose electrooxidation

Omruye Ozok Arici[1*], Sefika Kaya[2], Aykut Caglar[3], Hilal Kivrak[2,4*], Arif Kivrak[3,5]

[1] Department of Biomedical Engineering, Faculty of Engineering and Architectural Sciences, Eskisehir Osmangazi University, Eskisehir, 26040, Turkey, omruye.ozok@ogu.edu.tr, ORCID: 0000-0002-4164-8650

[2]Department of Chemical Engineering, Faculty of Engineering and Architectural Sciences, Eskisehir Osmangazi University, Eskisehir, 26040, Turkey, sefikakaya@ogu.edu..tr, ORCID: 0000-0003-3556-6461

[3]Technology and Innovation Center, Advance Organic Synthesis Laboratory, Eskisehir Osmangazi University, Eskişehir 26040, Turkey, aykut_802@hotmail.com, ORCID: 0000-0001-0681-1096

[4]Translational Medicine Research and Clinical Center, Eskisehir Osmangazi University, 26040 Eskisehir, Turkey, hilaldemir.kivrak@ogu.edu.tr, ORCID: 0000-0001-8001-7854

[5]Department of Chemistry, Faculty of Sciences, Eskisehir Osmangazi University, 26040 Eskisehir, Turkey, arif.kivrak@ogu.edu.tr , ORCID: 0000-0003-4770-2686

ABSTRACT

In this study (4-(3-iodobenzo[b]thiophen-2-yl)-N,N-dimethyllaniline (4), Sonagashira Coupling Reaction was synthesized using Electrophilic Cyclization Reactions. Then, the anode catalyst performance for glucose electrooxidation was investigated. The electrocatalytic activities of the organic catalyst were investigated by CV, CA and EIS measurements in 1 M KOH + 0.5 M $C_6H_{12}O_6$ solution. Interestingly, electrochemical depositing on organic catalyst by Pd metal increased the specific activity, and it was calculated as 0.61 mA/cm^2 Consequently, Pd@4 catalyst will be used as an electrocatalyst with high specific and stability and low charge transfer activity.

ARTICLE INFO

Research article

Received: 16.07.2023
Accepted: 6.12.2023

Keywords:
Catalyst,
electrooxidation,
glucose,
Pd.

*Corresponding author

1. Introduction

Energy is one of the most important factors for nature and social life. Energy production, conversion and consumption are considered as an important factor for the environment and a sustainable life. Technological developments, industrialization and the increase in the world population increase the demand for energy day by day [1]. With energy systems, environmental damage occurs in the stages from energy production to consumption and disposal.

Recently, important solutions have been developed for the current environmental problems associated with the release of substances harmful to the environment and human health. Among these solutions, renewable energy sources take an important place as an alternative [2]. Recently, among the renewable energy sources, batteries [3], organic solar cells [4], and fuel cells [5], stand out as clean energy sources. glucose [6], hydrazine [7], formic acid [8] and methanol [9] are often used in fuel cells. The direct use of glucose in fuel cells is one of the most popular methods due to its advantages [10]. Glucose is the most abundant natural monosaccharide and has a high energy density, making it a toxic, explosive and non-volatile organic molecule [11]. When a glucose molecule is completely oxidized, it forms 24 e^- and non-toxic products carbon dioxide and water (CO_2 and H_2O) [12]. Glucose electro-oxidation reactions in alkaline medium are shown below:

Anode: $C_6H_{12}O_6 + 36OH^- \rightarrow 6CO_3^{2-} + 24H_2O + 24e^-$ (1)

Cathode: $6O_2 + 24e^- + 12\,H_2O \rightarrow 24OH^-$ (2)

Overall: $C_6H_{12}O_6 + 6O_2 + 12OH^- \rightarrow 6CO_3^{2-} + 12\,H_2O$ (3)

Recently, many researchers have been working on the oxidation of glucose using anode electrocatalysts. Chai et al. found that Pd/C, Pd_3Cu/C and Pd_3Cu-B/C electrocatalysts and Pd_3Cu-B/C catalyst prepared by a simple aqueous phase approach exhibited the best stability and higher activity in glucose electrooxidation [13]. Yan et al. found that Pd_xAu_y/C exhibits a very sensitive and linear amperometric response for glucose molecules [14]. In addition, Basu et al. reported that Au/C and Pt-Au/C catalysts were tested in the glucose electrooxidation reaction and the Pt-Au/C catalyst showed more activity than the Au/C catalyst and showed lower activity than Pt/C[15].

Heterocyclic compounds such as thiophenes, indoles, pyridines are of vital importance for materials science as well as their biological activities[16]. Benzothiophene derivatives are among the most well-known heteroaromatic compounds. Organic molecules have advantages such as greater flexibility, lower molecular weight and wide absorption bands[17]. For this reason, organic catalysts are used for clean energy.

In this study, we aimed to develop glucose electrooxidation reaction organic-based catalysts to reduce the high cost of anode catalysts due to the high cost of noble metals. (4-(3-iodobenzo[b]thiophen-2-yl)-N,N-dimethyllanilin was synthesized as anode catalysts for the glucose electrooxidation reaction. All designed benzothiophene derives were defined by using ^{1}H NMR, and ^{13}C NMR. After characterization, the electro-oxidation activity of glucose as the anode catalyst of this organic catalyst was investigated. Glucose electrooxidation activities were found by CV, CA and EIS analyses. In addition, Pd metal was electrodeposited on the benzothiophene derivative to explore the effects of electrochemical activity. A-Pd-doped organic catalyst (Pd-4A) was characterized using electron microscopy with energy dispersive x-ray (SEM-EDX). Pd-Organic catalyst systems could be promising to work as fuel cell anode catalysts.

2. Experimental measurement

2.1. Preparation of organic catalysts

Synthesis of N,N-dimethyl-4-((2-(methylthio)phenyl)ethinyl)aniline (3)

2-Iodothianisole (1) (1 equiv.), $PdCl_2(PPh_3)_2$ (0.05 equiv.), 4-ethinyl-N,N-dimethylaniline (2) (1.2 equiv.) and CuI (0,05 equiv.) in THF (10 mL) and triethylamine (15 mL) were mixed at room temperature for 24 hours. When starting compound was gone, the mixture was extracted with EtOAc (3 X 15 mL). The organic phase was dried with $MgSO_4$, filtrated and concentrated under reduced pressure. The residue purified by using flash column chromatography on silica gel Hexane/Ethyl acetate (100:1) to give N,N-dimethyl-4-((2-(methylthio)phenyl)ethinyl)aniline (3) (89%). ^{1}H NMR (400 MHz, $CDCl_3$) δ 7.46 (d, J = 9 Hz, 3H), 7.31-7.21 (m, 1H), 7.16 (dd, J = 8;1 Hz, 1H), 7.12-7.03(m, 1H), 6.67 (d, J = 8 Hz, 2H), 2.99(s, 6H), 2.50 (s, 3H). ^{13}C NMR (100 MHz, $CDCl_3$) δ 149.8, 140.9, 132.7, 131.8, 127.9, 124.2, 124.1, 122.3, 111.8, 97.2, 40.2, 15.1.

Synthesis of (4-(3-iodobenzo[b]thiophen-2-yl)-N,N-dimethyllaniline (4)

N,N-dimethyl-4-((2-(methylthio)phenyl)ethinyl)aniline (3) (1 equiv.) in dichloromethane (30 mL) was added molecular iodide (2 equiv.) at room temperature. After 2 hours, reaction mixture was washed with saturated $Na_2S_2O_3$ and extracted with dichloromethane (3 X 20 mL). The combine organic phase was dried with $MgSO_4$, filtrated and concantrated under reduced pressure. The residue purified by using flash column chromatography on silica gel Hexane/Ethyl acetate (100:1) to give (4-(3-iodobenzo[b]thiophen-2-yl)-N,N-dimethyllaniline (4) (96%). ^{1}H NMR (400 MHz, $CDCl_3$) δ 7.81 (dd, J = 8; 0.5 Hz, 1H), 7.76(d, J = 8 Hz, 1H), 7.63(d, J = 8 Hz, 2H), 7.47-7.43 (m, 1H), 6.82(d, J = 8 Hz, 2H), 3.01(s, 6H). ^{13}C NMR (100 MHz, $CDCl_3$) δ 161.2, 150.6, 142.9, 142.1, 138.6, 130.8, 125.86, 125.2, 124.9, 121.9, 111.8, 76.7, 40.2.

2.2. Electrochemical measurements

Electrochemical measurements were performed using 1 M KOH + 1 M Glucose solution, using cyclic voltammetry (CV), chronoamperometry (CA) and electrochemical impedance spectroscopy (EIS) methods. CV measurements were carried in the potential range of -0.6-0.8 V, scanning speed of 50 mV/s. In order to increase the electrochemical activity of the catalyst, Pd metal was deposited on the benzothiophene derivative by electrodeposition method. Palladium metal was deposited on organic structure with CV in 0.1 mM K_2PdCI_4 + 0.1 M H_2SO_4 + 0.2 mM HCl solution at 10 mV/s scan rate. CA measurements were applied at potentials of -0.4, -0.2, 0, 0.2 and 0.4 V to determine the stability of the catalysts in 1000 s. The resistance of the catalyst to glucose electrooxidation was determined by EIS measurements at different values ranging from -0.6 to 0.4 V.

3.Results and discussion

3.1. Synthesis

The Sonogashira coupling reaction is an important reaction in organic chemistry that allows Pd-catalyzed formation of new carbon-carbon bonds between primary alkynes and halogenated aromatic structures [18]. In the first step of the study, a new carbon-carbon bond was established with the Sonagashira coupling reaction with 4-ethinyl-N,N-dimethylaniline catalyzed by 2 iodothioanisole Pd and N,N-dimethyl-4-((2-(methylthio)phenyl)ethinyl)aniline with 89%

yield. (3) synthesized. In the next step, (4-(3-iodobenzo[b]thiophen-2-yl)-N,N-dimethyllaniline (4) was synthesized in a high yield of 96% by electrophilic cyclization reaction(Fıgure 1).

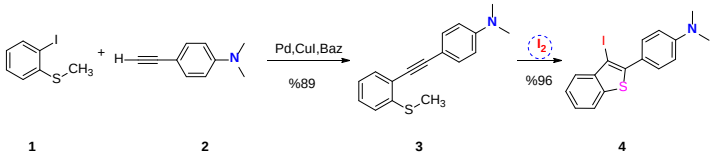

Fıgure 1. Synthesis of 4-(3-iodobenzo[b]thiophen-2-yl)-N,N-dimethyllaniline

3.2.Characterization Results

Figure 2 indicates the SEM-EDX and mapping analysis obtained to examine the surface structure and morphology of the **4** catalyst. As can be seen from the SEM images, it was observed that agglomeration did not occur and a homogeneous distribution occurred. Mapping and EDX analyses demonstrate that C (red), F (blue), O (yellow), and Pd (purple) elements are formed. These results show that the electrochemically Pd coating on the organic material has taken place. The electrochemical characterization results are evidence that the changed activity after Pd coating is due to the Pd atoms formed on the surface.

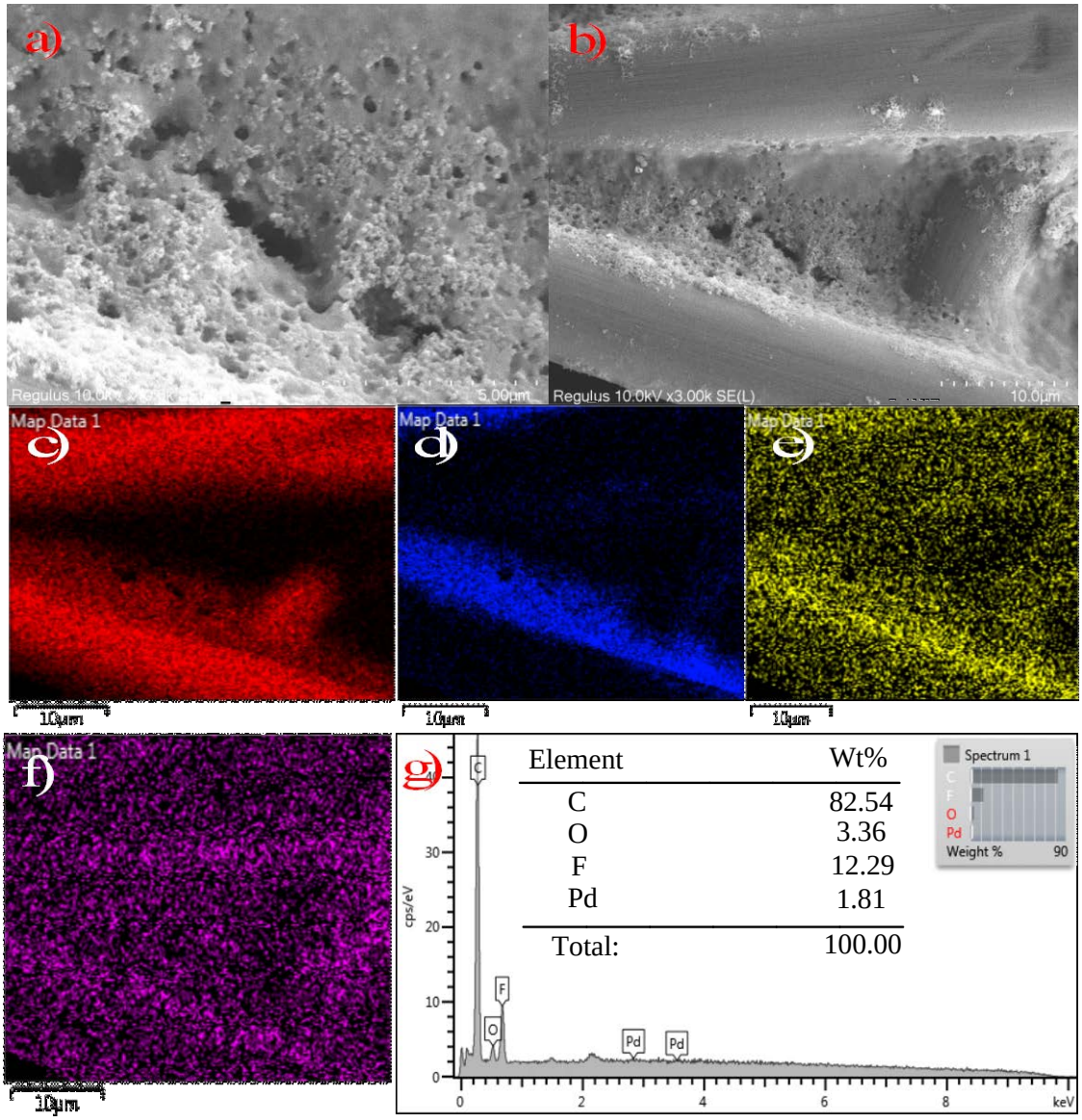

Figure 2. *SEM (a, b)-EDX (g) and mapping (C (c), F (d), O (e), and Pd (f)) of **4** catalyst.*

3.3. Electrochemical results

Glucose electrooxidation activities of **4** and **Pd@4** organic-based catalysts were investigated by CV measurements in 1 M KOH + 1 M $C_6H_{12}O_6$ solution. The CV analyses of the organic-based catalysts in the potential range of -0.6 ~ 0.8 V were presented in Figure 3. Although glucose is a high-energy fuel, it is difficult to break down, so no oxidation peak was observed in the glucose electrooxidation results of the organic catalyst. [19]. When the organic catalyst was doped with active metal such as Pd, the oxidation peak was observed as can be seen in Figure 3b. According to the EDX analysis (Figure 2g) results, it was observed that Pd metal was doped with organic material, albeit in a small amount. Therefore, the glucose oxidation peak current density occurring at a potential of 0.0 V (Figure 3b) was obtained as approximately 0.17 mA/cm^2.

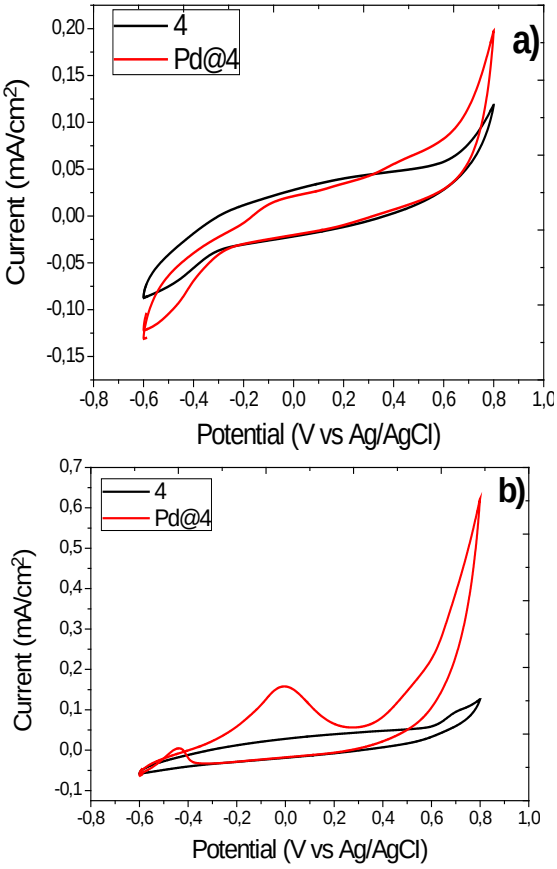

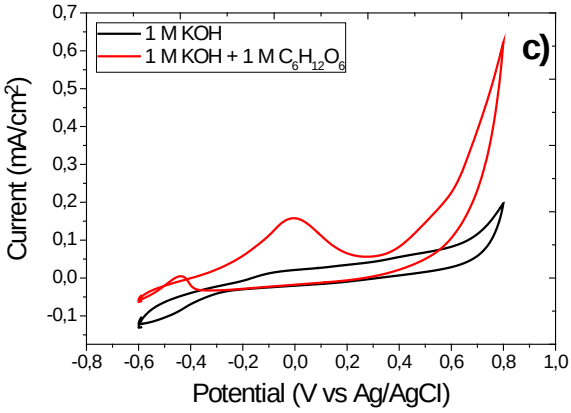

Figure 3. *CV analyses of **4** and **Pd@4** organic-based catalysts at a scan rate of 50 mV/s **a)** 1 M KOH, **b)** 1 M KOH + 1 M $C_6H_{12}O_6$, and c) comparison of Pd@4 organic-based catalyst in 1 M KOH and 1 M KOH + 1 M $C_6H_{12}O_6$ solutions.*

Figure 4 demonstrates the CA curves of organic-based catalysts. Firstly, CA curves of **Pd@4** organic-based catalyst at different potentials (-0.4 V to 0.4 V) were obtained (Figure 4a). The best stability was 0.4 V potential after 1000 s. As can be seen from Figure 4b, **Pd@4** organic-based catalyst exhibited the best catalytic activity and stability compared to the **4**, as in CV results.

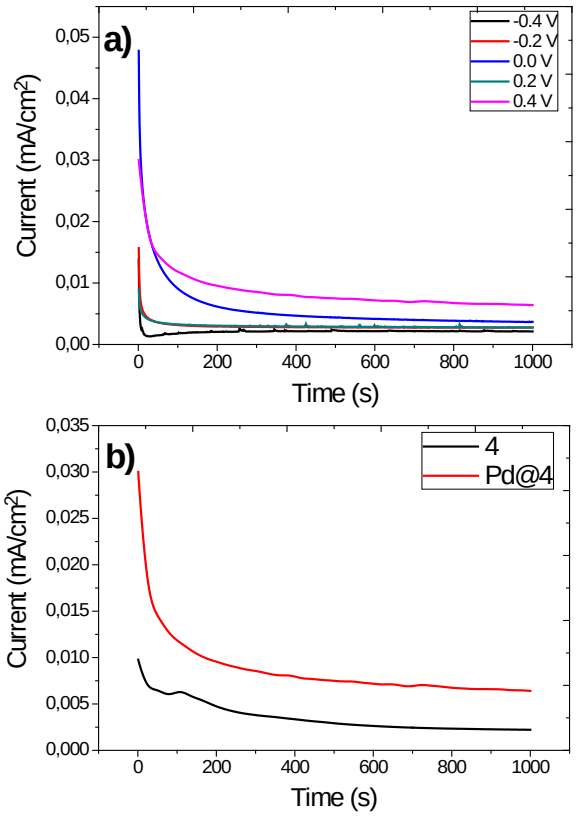

Figure 4. *CA curves of **a) Pd@4** organic-based catalyst at different potentials and **b)** comparison of organic-based catalysts at 0.4 V potential in 1 M KOH + 1 M $C_6H_{12}O_6$ solution.*

Nyquist plots obtained from EIS analysis were realized to investigate the electrochemical resistance of organic-based catalysts. In Nyquist diagrams, as the diameter of the semicircle decreases, the charge transfer resistance decreases and therefore the electrocatalytic activity increases. [20-21] Nyquist plots performed in 1 M KOH + 1 M $C_6H_{12}O_6$ solution was given in Figure 5(a, b). Nyquist plots were first obtained with **Pd@4** organic-based catalyst at different potentials (Figure 5a). As in the CA analysis, it showed the best electrochemical resistance of 0.4 V potential. The **Pd@4** organic-based catalyst exhibited the best resistance compared to the **4** at 0.4 V potential (Figure 8b).

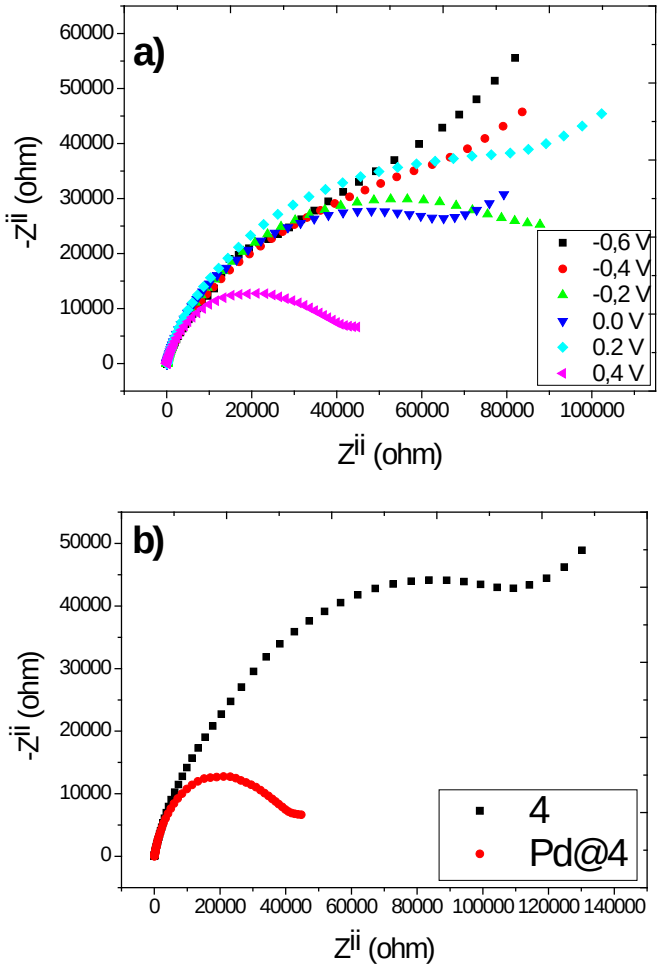

Figure 5. *Nyguist plots of* ***a) Pd@4*** *organic-based catalyst at different potentials and* ***b)*** *comparison of organic-based catalysts at 0.4 V potential in 1 M KOH + 1 M* $C_6H_{12}O_6$ *solution.*

4. Conclusion

In this study, (4-(3-iodobenzo[b]thiophen-2-yl)-N,N-dimethyllaniline (4) catalyst was synthesized via Sonogashira coupling reaction and electrophilic cyclization reactions. Then, the anode catalyst performance for glucose electrooxidation was investigated. The electrocatalytic activities of the organic catalyst were investigated by CV, CA and EIS measurements in 1 M KOH + 0.5 M $C_6H_{12}O_6$ solution. Interestingly, electrochemical depositing on organic catalyst by Pd metal increased the specific activity, and it was calculated as 0.61 mA/cm^2. The SEM-EDX results of Pd@4 confirmed the successful deposition of Pd metal on the organic catalyst. Consequently, Pd@4 catalyst will be used as an electrocatalyst with high specific activity and stability and low charge transfer resistance.

Acknowledgments

Eskisehir Osmangazi University Scientific Research Projects Commission (BAP Project No: FOA-2021-2203) supported this study.

References

[1]. Erdem, K.O.Ç. and Kadir, K., 2015. Enerji Kaynakları–Yenilenebilir Enerji Durumu. *Mühendis ve Makina*, *56*(668), pp.36-47.

[2]. Oğulata, R. 2007. "Potential of Renewable Energies in Turkey," Energy Engineering, vol. 133 (1), p. 63-68.

[3]. Park, M., Lee, T. and Kim, B.S., 2013. Covalent functionalization based heteroatom doped graphene nanosheet as a metal-free electrocatalyst for oxygen reduction reaction. *Nanoscale*, *5*(24), pp.12255-12260.

[4]. Clarke, T.M. and Durrant, J.R., 2010. Charge photogeneration in organic solar cells. *Chemical reviews*, *110*(11), pp.6736-6767.

[5]. Kivrak, H., Can, M., Duru, H. and Sahin, O., 2014. Methanol electrooxidation study on mesoporous silica supported Pt–Co direct methanol fuel cell anode. *International Journal of Chemical Reactor Engineering*, *12*(1), pp.369-375.

[6]. Er, O.F., Caglar, A. and Kivrak, H., 2020. Enhanced electrochemical glucose oxidation in alkaline solution over indium decorated carbon supported palladium nanoparticles. Materials Chemistry and Physics, 254, p.123318.

[7]. Feng, G., Kuang, Y., Li, P., Han, N., Sun, M., Zhang, G. and Sun, X., 2017. Single crystalline ultrathin nickel–cobalt alloy nanosheets array for direct hydrazine fuel cells. *Advanced Science*, *4*(3), p.1600179.

[8]. Yao, S., Li, G., Liu, C. and Xing, W., 2015. Enhanced catalytic performance of carbon supported palladium nanoparticles by in-situ synthesis for formic acid electrooxidation. *Journal of Power Sources*, *284*, pp.355-360.

[9]. Arico, A.S., Antonucci, P.L., Modica, E., Baglio, V., Kim, H. and Antonucci, V., 2002. Effect of Pt □Ru alloy composition on high-temperature methanol electro-oxidation. *Electrochimica Acta*, *47*(22-23), pp.3723-3732.

[10]. Rapoport, B.I., Kedzierski, J.T. and Sarpeshkar, R., 2012. A glucose fuel cell for implantable brain–machine interfaces. *PloS one*, *7*(6), p.e38436.

[11]. Tao, B., Miao, F. and Chu, P.K., 2012. Preparation and characterization of a novel nickel–palladium electrode supported by silicon nanowires for direct glucose fuel cell. *Electrochimica acta*, *65*, pp.149-152.

[12]. Song, B. Y., Li, Y. S., He, Y. L., Cheng, Z. D., 2014. Anode structure design for the highperformance anion-exchange membrane direct glucose fuel cell. Energy Procedia, 61: 2118-2122.

[13]. Chai, D., Wang, W., Wang, F., Kang, Y., Yang, Y. and Lei, Z., 2016. A facile precipitation procedure for synthesis of binary Sn-Co oxide promoting Pd catalyst towards glucose electrooxidation. *Electrochimica Acta*, *189*, pp.295-302.

[14]. Yan, L., Brouzgou, A., Meng, Y., Xiao, M., Tsiakaras, P. and Song, S., 2014. Efficient and poison-tolerant PdxAuy/C binary electrocatalysts for glucose electrooxidation in alkaline medium. *Applied Catalysis B: Environmental*, *150*, pp.268-274.

[15]. Basu D, Basu S. Synthesis and characterization of PteAu/C catalyst for glucose electro-oxidation for the application in direct glucose fuel cell. Int J Hydrogen Energy 2011;36:14923-9.

[16]. Cho CH, Neuenswander B, Lushington GH, Larock RC. Solution-phase parallel synthesis of a multi-substituted benzo b thiophene library. J Combin Chem 2009;11:900-6.

[17]. Ozok, O., Kavak, E., Er, O.F., Kivrak, H. and Kivrak, A., 2020. Novel benzothiophene based catalyst with enhanced activity for glucose electrooxidation. *International Journal of Hydrogen Energy*, *45*(53), pp.28706-28715.

[18]. Wang, D. and Gao, S., 2014. Sonogashira coupling in natural product synthesis. *Organic Chemistry Frontiers*, *1*(5), pp.556-566.

[19]. Ozok-Arici, O., Kaya, S., Caglar, A., Kivrak, H. and Kivrak, A., 2022. Glucose Electrooxidation Study on 3-iodo-2-(aryl/alkyl) benzo [b] thiophene Organic Catalyst. *Journal of Electronic Materials*, *51*(4), pp.1653-1662.

[20]. Qu, W., Wang, Z., Sui, X. and Gu, D., 2014. An efficient antimony doped tin oxide and carbon nanotubes hybrid support of Pd catalyst for formic acid electrooxidation. *international journal of hydrogen energy*, *39*(11), pp.5678-5688

[21]. Karuppasamy, L., Chen, C.Y., Anandan, S. and Wu, J.J., 2018. Sonochemical fabrication of reduced graphene oxide supported Au nano dendrites for ethanol electrooxidation in alkaline medium. *Catalysis Today*, *307*, pp.308-317.

MANAS Journal of Engineering
ISSN 1694-7398 — e-ISSN 1694-7398

Volume 11, Issue 2, (2023) Pages 223-228
https://doi.org/10.51354/mjen.1361003

On approximating fixed points of a new class of generalized nonexpansive mappings in uniformly convex hyperbolic space

Nazli Kadioglu Karaca[1]

[1] Department of Mathematics, Faculty of Science, Atatürk University, Erzurum, Turkey, nazli.kadioglu@atauni.edu.tr, ORCID: 0000-0002-6308-5879

ABSTRACT

In this paper, we introduce the definition of a new class of generalized nonexpansive mappings in hyperbolic space. Additionally, we construct the rewritten version of the Mann iteration process in hyperbolic space. Then, using the iterative procedure we established, we prove convergence theorems for $a-b-$generalized nonexpansive mappings in a uniformly convex hyperbolic space. Lastly, we offer a numerical example to illustrate our findings.

ARTICLE INFO

Research article

Received: 15.09.2023
Accepted: 13.12.2023

Keywords: Fixed point, generalized nonexpansive mappings, uniformly convex hyperbolic space

**Corresponding author*

1. Introduction

In order to solve practical issues in mathematics, physics, engineering, and game theory, fixed point theory is a useful area of study. Analytical solutions of fixed point problems are challenging, requiring iterative solutions. Although academics create a variety of strategies, the development on effective algorithms is still underway.

In the field of nonlinear analysis, the fixed point theory is crucial. The Picard iteration, as defined by $\varkappa_{n+1} = \Upsilon\varkappa_n$, $\forall n \in \mathbb{N}$., is one of the well-known iterative procedures. To approximate to fixed points of contraction mappings, this iteration approach has been utilized. When using nonexpansive mappings rather than contraction mappings, the Picard iterative method is unable to approach fixed points. Numerous writers have investigated new iteration processes and mapping classes in this context for the purpose of approximating fixed points.

For the class of nonexpansive self-mappings on a closed and bounded subset of a uniformly convex Banach space, Browder [6] demonstrated the existence of a fixed point. After Browder's result, researchers have developed iterative procedures to approximate fixed points in nonexpansive and nonlinear mappings, with research focusing on faster and more efficient techniques. Studies have been conducted in uniformly convex Banach spaces and CAT(0) spaces.(see [1], [7], [20], [22], [23] and the references therein)

Suzuki [19] established a new class of nonexpansive mappings and demonstrated several fixed point theorems for them. Many researchers have contributed to the literature by generalizing Suzuki's generalized non-expansive mapping (see [3], [4], [16]). More recently, Adeyemi et al. [2] introduced the generalized nonexpansive mappings and in uniformly convex hyperbolic space, they demonstrated approaching the fixed point of these mappings.

Along with the nonlinear mappings, the significance that the spaces play in the study of fixed point theory is also quite important, including Hilbert and Banach spaces. Banach spaces have convex structures, making it easy to exist fixed points. Metric spaces lack this structure, making it necessary to introduce convex structures into them. By examining the fixed points for nonexpansive mappings in convex metric spaces, Takahashi [21] was the pioneer in developing the idea of convex metric space.

Since then, many convex structures have been introduced onto metric spaces in a number of different attempts. As a result of these studies, many fixed point theorems have been obtained by applying well-known fixed point iteration processes to hyperbolic spaces (see [9], [10], [13], [17]). Hyperbolic spaces have a convex structure, with the convex structure introduced by Kohlenbach [13] being more general.

In this work, we introduce a new class of generalized nonexpansive mappings in hyperbolic space. Also, we constitute the form in hyperbolic space of the well known Mann iteration process. Then, we prove strong and Δ-convergence results for these mappings in a uniformly convex hyperbolic space using our introduced iterative process.

2. PRELIMINARIES

Firstly, Takahashi [21] proposed the idea of convex metric space in 1970 as follows:

A mapping $W : \mathfrak{S}\times\mathfrak{S}\times[0,1] \longrightarrow \mathfrak{S}$ is a convex structure in $\mathfrak{S}$ if

$$\hbar(\mathfrak{q}, W(\varkappa,\mu,\eth)) \leq (1-\eth)\hbar(\mathfrak{q},\varkappa) + \eth\hbar(\mathfrak{q},\mu),$$

for all $\varkappa$,calμ,$calfrakq\in$ $\mathfrak{S}$ and $\eth \in [0,1]$. A metric space $(\mathfrak{S},\hbar)$ together with a convex structure W defined on it is called a convex metric space. A subset $\mathcal{M}$ of a convex metric space $\mathfrak{S}$ is convex if calW($\varkappa$,calμ,$\eth$) $\in \mathcal{M}$ for all $\varkappa$,cal$\mu\in$ $\mathcal{M}$ and $\eth \in [0,1]$.

Afterwards, this idea was greatly expanded upon by numerous authors. In Kohlenbach's hyperbolic space [13], one of these convex structures is present. There are various interpretations of hyperbolic space in the literature.

A hyperbolic space $(\mathfrak{S},\hbar,W)$ (see [13]) is a metric space $(\mathfrak{S},\hbar)$ together with a mapping $W : \mathfrak{S}\times\mathfrak{S}\times[0,1] \longrightarrow \mathfrak{S}$ satisfying

(W1) $\hbar(z, W(\varkappa,\text{cal}\mu,\eth)) \leq (1-\eth)\hbar(z,\varkappa) + \eth\hbar(z,\text{cal}\mu)$,

(W2) $\hbar(W(\varkappa,\text{cal}\mu,\eth_1), W(\varkappa,\text{cal}\mu,\eth_2)) = |\eth_1-\eth_2|\,\hbar(\varkappa,\text{cal}\mu)$,

(W3) $W(\varkappa,\text{cal}\mu,\eth) = W(\text{cal}\mu,\varkappa,(1-\eth))$,

(W4) $\hbar(W(\varkappa,z,\eth), W(\text{cal}\mu,\text{W},\eth)) \leq (1-\eth)\hbar(\varkappa,\text{cal}\mu)+\eth\hbar(z,W)$,

for all $\varkappa$,calμ,z,W$\in$ $\mathfrak{S}$ and $\eth,\eth_1,\eth_2 \in [0,1]$.

A hyperbolic space $(\mathfrak{S},\hbar,W)$ is said to be uniformly convex [18] if for all calfrakq,$\varkappa$,cal$\mu\in$ $\mathfrak{S}$, $r>0$ and $\varepsilon \in (0,2]$, there exists a $\delta \in (0,1]$ such that $\hbar\left(z, W\left(\varkappa,\mu,\frac{1}{2}\right),\mathfrak{q}\right) \leq (1-\delta)r$ whenever $\hbar(\varkappa,\text{calfrakq}) \leq r$, $\hbar(\text{cal}\mu,calfrakq)\leq r$ and $\hbar(\varkappa,\text{cal}\mu)\geq \varepsilon r$.

A mapping $\eta : (0,\infty)\times(0,2] \longrightarrow (0,1]$ providing such $\delta = \eta(r,\varepsilon)$ for given $r>0$ and $\varepsilon \in (0,2]$ is called modulus of uniform convexity. We call η monotone if it decreases with r (for a fixed ε).

We now compile some fundamental definitions of asymptotic centers and radiuses.

Let $\mathfrak{S}$ be a hyperbolic space and $\{\varkappa_n\}$ be a bounded sequence in $\mathfrak{S}$. For $\varkappa \in \mathfrak{S}$, define a continuous functional $r(.,\{\varkappa_n\}) : \mathfrak{S} \longrightarrow [0,\infty)$ by

$$r(\varkappa,\{\varkappa_n\}) = \lim_{n\longrightarrow\infty}\sup\hbar(\varkappa,\varkappa_n).$$

The asymptotic radius $r(\{\varkappa_n\})$ of $\{\varkappa_n\}$ is given by

$$r(\{\varkappa_n\}) = \inf\{r(\varkappa,\{\varkappa_n\}) : \varkappa \in \mathcal{X}\}.$$

The asymptotic radius $r_{\mathcal{M}}(\{\varkappa_n\})$ of $\{\varkappa_n\}$ with respect to a subset $\mathcal{M}$ of $\mathfrak{S}$ is given by

$$r_{\mathcal{M}}(\{\varkappa_n\}) = \inf\{r(\varkappa,\{\varkappa_n\}) : \varkappa \in \mathcal{M}\}.$$

The asymptotic center $A(\{\varkappa_n\})$ of $\{\varkappa_n\}$ is the set

$$A(\{\varkappa_n\}) = \{\varkappa \in \mathcal{X} : r(\varkappa,\{\varkappa_n\}) = r(\{\varkappa_n\})\}.$$

The asymptotic center $A_{\mathcal{M}}(\{\varkappa_n\})$ of $\{\varkappa_n\}$ with respect to a subset $\mathcal{M}$ of $\mathfrak{S}$ is the set

$$A(\{\varkappa_n\}) = \{\varkappa \in \mathcal{X} : r(\varkappa,\{\varkappa_n\}) = r_{\mathcal{M}}(\{\varkappa_n\})\}.$$

Lim [15] proceeded by thinking about how Δ-convergence was defined in a metric space in 1976, and Dhompongsa and Panyanak [8] have studied its analogue in CAT(0) spaces. Khan et al. resumed their examination of Δ-convergence in the overall structure of hyperbolic spaces in [11].

Now, we recall the notion of Δ-convergent.

[12]A sequence $\{\varkappa_n\}$ in $\mathfrak{S}$ is said to be Δ-convergent to $\varkappa \in \mathfrak{S}$, if, for every subsequence $\{\mathfrak{k}_n\}$ of $\{\varkappa_n\}$, $\varkappa$ is the unique asymptotic center of $\{\mathfrak{k}_n\}$. In this case, $\varkappa$ is called as Δ-limit of $\{\varkappa_n\}$ and we write $\Delta-\lim_{n\longrightarrow\infty}\varkappa_n = \varkappa$.

The generalized nonexpansive mapping in uniformly convex hyperbolic space was first developed in 2021 by Adeyemi et al. [2] as follows: Let $\mathcal{M}$ be a nonempty subset of a hyperbolic space $\mathfrak{S}$. A mapping $\Upsilon : \mathcal{M} \longrightarrow \mathcal{M}$ is called generalized nonexpansive mapping if there exist $\alpha,\beta,\gamma \in [0,1)$, with $\gamma+\beta<1$ such that for all $\varkappa$,$calu \in \mathcal{M}$,

$$(1-\alpha)\hbar(\Upsilon\varkappa,\varkappa) \leq \hbar(\varkappa,\mu)$$
$$\Longrightarrow \hbar(\Upsilon\varkappa,\Upsilon\mu) \leq$$
$$\beta\hbar(\mu,\Upsilon\varkappa) + \gamma\hbar(\varkappa,\Upsilon\mu) + [1-(\gamma+\beta)]\,\hbar(\varkappa,\mu).$$

We will require the following outcomes for the follow-up:

[14]Let $(\mathfrak{S},\hbar,W)$ be a complete uniformly convex hyperbolic space with monotone modulus of uniform convexity η. Then every bounded sequence $\{\varkappa_n\}$ in $\mathfrak{S}$ has a unique

asymptotic center with respect to any nonempty closed convex subset $\mathcal{M}$ of $\mathfrak{S}$.

[11]Let $(\mathfrak{S}, \hbar, W)$ be a uniformly convex hyperbolic space with monotone modulus of uniform convexity η. Let $\varkappa \in \mathfrak{S}$ and $\{\alpha_n\}$ be a sequence in $[a, b]$ for some $a, b \in (0, 1)$. If $\{\varkappa_n\}$ and $\{\mu_n\}$ are sequences in $\mathfrak{S}$ such that

$$\lim_{n\longrightarrow\infty} \sup \hbar(\varkappa_n, \varkappa) \leq r, \quad \lim_{n\longrightarrow\infty} \sup \hbar(\mu_n, \varkappa) \leq r,$$

$$\lim_{n\longrightarrow\infty} \hbar(W(\varkappa_n, \mu_n, \alpha_n), \varkappa) = r$$

for some $r \geq 0$, then

$$\lim_{n\longrightarrow\infty} \hbar(\varkappa_n, \mu_n) = 0.$$

3. MAIN RESULTS

In the context of uniformly convex hyperbolic space, we develop a new class of generalized nonexpansive mapping and establish the version in hyperbolic space of the Mann iteration process. Also, we give Δ-convergence and strong convergence results for these mappings we introduced in uniformly convex hyperbolic space using the new form of the Mann iteration process.

Let $\mathcal{M}$ be a nonempty subset of a hyperbolic pace $\mathfrak{S}$. A mapping $\Upsilon : \mathcal{M} \longrightarrow \mathcal{M}$ is called $a - b-$generalized nonexpansive mapping if there exist $a, b \in [0, \frac{1}{2})$ and $\alpha \in [0, 1)$ with $2a + 2b < 1$ such that for all $\varkappa$,cal$\mu \in \mathcal{M}$,

$$(1 - \alpha)\hbar(\Upsilon\varkappa, \varkappa) \leq \hbar(\varkappa, \mu)$$

$$\Longrightarrow \hbar(\Upsilon\varkappa, \Upsilon\mu) \leq a\left[\hbar(\mu, \Upsilon\varkappa) + \hbar(\varkappa, \Upsilon\mu)\right]$$

$$+b\left[\hbar(\varkappa, \Upsilon\varkappa) + \hbar(\mu, \Upsilon\mu)\right] + \left[1 - (2a + 2b)\right]\hbar(\varkappa, \mu).$$

The Mann iteration process has been extensively studied for approximating fixed points of nonexpansive mappings. With Υ being a self-mapping on a subset of a Banach space, the Mann iteration process is defined as follows:

$$\begin{cases} \varkappa_1 \in \mathcal{M} \\ \varkappa_{n+1} = (1 - \alpha_n)\varkappa_n + \alpha_n \Upsilon\varkappa_n, \ n \geq 1, \end{cases} \tag{0}$$

where $\{\alpha_n\}$ is real sequences in $[0, 1]$.

A conversion of the Mann iteration process (0) from Banach space to hyperbolic space is seen in the iteration process that follows:

$$\begin{aligned} \varkappa_1 &\in \mathcal{M}, \\ \varkappa_{n+1} &= W(\varkappa_n, \Upsilon\varkappa_n, \alpha_n), \ n \geq 1. \end{aligned} \tag{1}$$

Assume that $\mathcal{M}$ is a nonempty subset of a metric space $(\mathfrak{S}, \hbar)$. Then Υ, a self-mapping on $\mathcal{M}$, is nonexpansive if $\hbar(\Upsilon\varkappa, \Upsilon$cal$\mu) \leq \hbar(\varkappa$,cal$\mu) for all \varkappa$,cal$\mu \in \mathcal{M}$. From this point forward, the term F will refer to the collection of all common fixed points for nonexpansive mappings on $\mathcal{M}$.

Within this part, for nonexpansive mappings in uniformly convex hyperbolic spaces, we demonstrate a few convergence theorems.

We start by outlining the crucial lemmas below.

Let $\mathcal{M}$ be a nonempty, closed and convex subset of a hyperbolic space $\mathfrak{S}$ and Υ be an $a - b-$generalized nonexpansive self mappings on $\mathcal{M}$ with $F \neq \emptyset$. Then for the sequence $\{\varkappa_n\}$ defined in (1), we have $\lim_{n\longrightarrow\infty} \hbar(\varkappa_n, \varpi)$ exists for each $\varpi \in F$.

Proof For any $\varpi \in F$, it follows from (1) that

$$\begin{aligned} \hbar(\varkappa_{n+1}, \varpi) &= \hbar(W(\varkappa_n, \Upsilon\varkappa_n, \alpha_n), \varpi) \\ &\leq (1 - \alpha_n)\hbar(\varkappa_n, \varpi) + \alpha_n\hbar(\Upsilon\varkappa_n, \varpi) \\ &\leq (1 - \alpha_n)\hbar(\varkappa_n, \varpi) \\ &+\alpha_n a\left[\hbar(\varpi, \Upsilon\varkappa_n) + \hbar(\varkappa_n, \Upsilon\varpi)\right] \\ &+\alpha_n b\left[\hbar(\varkappa_n, \Upsilon\varkappa_n) + \hbar(\varpi, \Upsilon\varpi)\right] \\ &+\alpha_n\left[1 - (2a + 2b)\right]\hbar(\varkappa_n, \varpi) \\ &\leq \left[1 - \alpha_n(a + b)\right]\hbar(\varkappa_n, \varpi) \\ &+\alpha_n(a + b)\hbar(\varpi, \Upsilon\varkappa_n). \end{aligned}$$

and

$$\begin{aligned} \hbar(\varpi, \Upsilon\varkappa_n) &= \hbar(\Upsilon\varpi, \Upsilon\varkappa_n) \\ &\leq a\left[\hbar(\varkappa_n, \Upsilon\varpi) + \hbar(\varpi, \Upsilon\varkappa_n)\right] \\ &+b\left[\hbar(\varpi, \Upsilon\varpi) + \hbar(\varkappa_n, \Upsilon\varkappa_n)\right] \\ &+\left[1 - (2a + 2b)\right]\hbar(\varpi, \varkappa_n) \\ &\Longrightarrow \left[1 - (a + b)\right]\hbar(\varpi, \Upsilon\varkappa_n) \\ &\leq \left[1 - (a + b)\right]\hbar(\varpi, \varkappa_n) \\ &\Longrightarrow \hbar(\varpi, \Upsilon\varkappa_n) \leq \hbar(\varpi, \varkappa_n) \end{aligned}$$

Writing (3) in (3), we have

$$\begin{aligned} \hbar(\varkappa_{n+1}, \varpi) &\leq \left[1 - \alpha_n(a + b)\right]\hbar(\varkappa_n, \varpi) \\ &+\alpha_n(a + b)\hbar(\varpi, \varkappa_n) \\ &= \hbar(\varkappa_n, \varpi). \end{aligned}$$

Hence $\lim_{n\longrightarrow\infty} \hbar(\varkappa_n, \varpi)$ exists for each $\varpi \in F$. □

Let us consider a subset $\mathcal{M}$ of a uniformly convex hyperbolic space $\mathfrak{S}$ with monotone modulus of uniform convexity η . Let the set $\mathcal{M}$ be a nonempty, closed and convex and Υ be an $a - b-$generalized nonexpansive self mappings on $\mathcal{M}$ with $F \neq \emptyset$. Assume that the sequence $\{\varkappa_n\}$ is defined by (1). Then

$$\lim_{n\longrightarrow\infty} \hbar(\varkappa_n, \Upsilon\varkappa_n) = 0.$$

Proof Let $\varpi \in F$. By Lemma 3, it follows that $\lim_{n\longrightarrow\infty} \hbar(\varkappa_n, \varpi)$ exists. We may assume that

$$\lim_{n\longrightarrow\infty} \hbar(\varkappa_n, \varpi) = r.$$

(i) Let $r = 0$. By (3), we have

$$\hbar(\varkappa_n, \Upsilon\varkappa_n) \leq \hbar(\varkappa_n, \varpi) + \hbar(\varpi, \Upsilon\varkappa_n) \leq 2\hbar(\varkappa_n, \varpi).$$

Taking limit for $n \longrightarrow \infty$, we obtain $\lim_{n\longrightarrow\infty} \hbar(\varkappa_n, \Upsilon\varkappa_n) = 0$.

(ii) Let $r > 0$. By (3), we get

$$\lim_{n\longrightarrow\infty} \sup \hbar(\Upsilon\varkappa_n, \varpi) \leq \lim_{n\longrightarrow\infty} \sup \hbar(\varkappa_n, \varpi) = r$$

and since

$$\lim_{n\longrightarrow\infty} \hbar(\varkappa_{n+1}, \varpi) = \lim_{n\longrightarrow\infty} \hbar(W(\varkappa_n, \Upsilon\varkappa_n, \alpha_n), \varpi) = r,$$

thus, from Lemma 2, we conclude that

$$\lim_{n\longrightarrow\infty} \hbar(\varkappa_n, \Upsilon\varkappa_n) = 0.$$

□

We now demonstrate the result about the Δ-convergence of the iteration process specified by (1) in a uniformly convex hyperbolic space.

Let $\mathcal{M}$, $\mathfrak{S}$, Υ and $\{\varkappa_n\}$ be the same as in Lemma 3. Then the sequence $\{\varkappa_n\}$ Δ-converges to a point in F.

Proof From proof of Lemma 3, it is easily seen that the sequence $\{\varkappa_n\}$ is bounded. According to Lemma 2, $\{\varkappa_n\}$ has a unique asymptotic center, which is $A_{\mathcal{M}}(\{\varkappa_n\}) = \{\varkappa\}$. Suppose that $\{\mathfrak{k}_n\}$ is any subsequence of $\{\varkappa_n\}$ such that $A_{\mathcal{M}}(\{\mathfrak{k}_n\}) = \{\mathfrak{k}\}$. By Lemma 3, we have

$$\lim_{n\longrightarrow\infty} \hbar(\mathfrak{q}_n, \Upsilon\mathfrak{q}_n) = 0. \tag{1}$$

We claim that $calfrakq \in F$. So, we calculate

$$\begin{aligned}
\hbar(\Upsilon\mathfrak{q}, \mathfrak{q}_n) &= \hbar(\Upsilon\mathfrak{q}, \Upsilon\mathfrak{q}_n) + \hbar(\Upsilon\mathfrak{q}_n, \mathfrak{q}_n) \\
&\leq a\left[\hbar(\mathfrak{q}_n, \Upsilon\mathfrak{q}) + \hbar(\mathfrak{q}, \Upsilon\mathfrak{q}_n)\right] \\
&\quad + b\left[\hbar(\mathfrak{q}, \Upsilon\mathfrak{q}) + \hbar(\mathfrak{q}_n, \Upsilon\mathfrak{q}_n)\right] \\
&\quad + \left[1 - (2a + 2b)\right]\hbar(\mathfrak{q}, \mathfrak{q}_n) + \hbar(\Upsilon\mathfrak{q}_n, \mathfrak{q}_n) \\
&\leq a\left[\hbar(\mathfrak{q}_n, \Upsilon\mathfrak{q}) + \hbar(\mathfrak{q}, \mathfrak{q}_n) + \hbar(\mathfrak{q}_n, \Upsilon\mathfrak{q}_n)\right] \\
&\quad + b\left[\hbar(\mathfrak{q}, \mathfrak{q}_n) + \hbar(\mathfrak{q}_n, \Upsilon\mathfrak{q}) + \hbar(\mathfrak{q}_n, \Upsilon\mathfrak{q}_n)\right] \\
&\quad + \left[1 - (2a + 2b)\right]\hbar(\mathfrak{q}, \mathfrak{q}_n) + \hbar(\Upsilon\mathfrak{q}_n, \mathfrak{q}_n) \\
\Longrightarrow \hbar(\Upsilon\mathfrak{q}, \mathfrak{q}_n) &\leq \hbar(\mathfrak{q}, \mathfrak{q}_n) + \left[\frac{1 + a + b}{1 - (a + b)}\right]\hbar(\Upsilon\mathfrak{q}_n, \mathfrak{q}_n).
\end{aligned}$$

Taking lim sup on both sides of the last inequality and using (1), we obtain

$$\begin{aligned}
\lim_{n\longrightarrow\infty} \sup \hbar(\Upsilon\mathfrak{q}, \mathfrak{q}_n) &\leq \lim_{n\longrightarrow\infty} \sup \hbar(\mathfrak{q}, \mathfrak{q}_n) \\
&\Longrightarrow r(\Upsilon\mathfrak{q}, \{\mathfrak{q}_n\}) \leq r(\mathfrak{q}, \{\mathfrak{q}_n\}).
\end{aligned}$$

The fact that the asymptotic center is unique suggests that $\Upsilon calfrakq$=$calfrakq$. This means that $calfrakq \in F$. Since $\lim_{n\longrightarrow\infty} \hbar(\varkappa_n, calfrakq)$ exists, and taking into account the uniqueness of the asymptotic center, we get

$$\begin{aligned}
\lim_{n\longrightarrow\infty} \sup \hbar(\mathfrak{q}_n, \mathfrak{q}) &< \lim_{n\longrightarrow\infty} \sup \hbar(\mathfrak{q}_n, \varkappa) \\
&\leq \lim_{n\longrightarrow\infty} \sup \hbar(\varkappa_n, \varkappa) \\
&< \lim_{n\longrightarrow\infty} \sup \hbar(\varkappa_n, \mathfrak{q}) = \lim_{n\longrightarrow\infty} \sup \hbar(\mathfrak{q}_n, \mathfrak{q})
\end{aligned}$$

which is a contradiction. Hence $\varkappa = calfrakq$. Thus $A(\{\mathfrak{k}_n\}) = \{\mathfrak{k}\}$ for all subsequences $\{\mathfrak{k}_n\}$ of $\{\varkappa_n\}$, that is, $\{\varkappa_n\}$ Δ-converges to $\varkappa \in F$. □

Let $\mathcal{M}$ be a subset of a metric space $\mathfrak{S}$. A sequence $\{\varkappa_n\}$ in $\mathfrak{S}$ is called as Fejér monotone with respect to $\mathcal{M}$. if $\hbar(\varkappa_{n+1}, \varpi) \leq \hbar(\varkappa_n, \varpi)$ for all $\varpi \in \mathcal{M}$ and $n \in \mathbb{N}$.

The following result is required for the sake of proving the main theorem:

[5]Let $(\mathfrak{S}, \hbar)$ be a complete metric space and $\mathcal{M}$ be a nonempty closed subset of $\mathfrak{S}$. Consider the sequence $\{\varkappa_n\}$ in $\mathcal{M}$ and suppose that $\{\varkappa_n\}$ is Fejér monotone with respect to $\mathcal{M}$. Then $\{\varkappa_n\}$ converges to some $\varpi \in \mathcal{M}$ if and only if $\lim_{n\longrightarrow\infty} \hbar(\varkappa_n, \mathcal{M}) = 0$.

Following that, we establish the strong convergence for the iteration process defined by (1).

Let $\mathcal{M}, \mathfrak{S}, \Upsilon$ and $\{\varkappa_n\}$ be the same as in Lemma 3. Then $\{\varkappa_n\}$ converges strongly to some $\varpi \in F$ if and only if $\liminf_{n\longrightarrow\infty} \hbar(\varkappa_n, F) = 0$ where $\hbar(\varkappa, F) = \inf\{\hbar(\varkappa, \varpi) : \varpi \in F\}$.

Proof If $\{\varkappa_n\}$ converges to $\varpi \in F$, then $\lim_{n\longrightarrow\infty} \hbar(\varkappa_n, \varpi) = 0$. Since $0 \leq \hbar(\varkappa_n, F) \leq \hbar(\varkappa_n, \varpi)$, we have $\liminf_{n\longrightarrow\infty} \hbar(\varkappa_n, F) = 0$.

On the contrary, presume that $\liminf_{n\longrightarrow\infty} \hbar(\varkappa_n, F) = 0$. As a result of Lemma 3 that $\lim_{n\longrightarrow\infty} \hbar(\varkappa_n, F)$ exists. Thus by hypothesis, $\lim_{n\longrightarrow\infty} \hbar(\varkappa_n, F) = 0$. From Lemma 3, it is said that $\{\varkappa_n\}$ is Fejér monotone with respect to F. Therefore, Lemma 3 indicate that $\{\varkappa_n\}$ converges strongly to a point ϖ in F. □

In Theorem 3, the condition $\limsup_{n\longrightarrow\infty} \hbar(\varkappa_n, F) = 0$ can be used in place of the condition $\liminf_{n\longrightarrow\infty} \hbar(\varkappa_n, F) = 0$.

Let $\mathfrak{S} = \mathbb{R}$ with metric defined by $\hbar(\varkappa, \mu) = |\varkappa - \mu|$ and $\mathcal{M} = \left[-\frac{1}{3}, \frac{1}{3}\right]$. Choose a mapping $\Upsilon : \mathcal{M} \longrightarrow \mathcal{M}$ as

$$\Upsilon\varkappa = \begin{cases} \frac{1-x}{2}, & \text{if } \varkappa \neq \frac{1}{3}, \\ 0, & \text{if } \varkappa = \frac{1}{3}. \end{cases}$$

Selecting $a = \frac{1}{6}$ and $b = \frac{1}{6}$ and for $\alpha \in [0, 1)$, then Υ is an $a - b-$generalized nonexpansive mapping. To prove that, we consider three different cases as follows:

Case 1 For $\varkappa = \frac{1}{3}$ and $\mu = \frac{1}{3}$, since $\hbar(\Upsilon\varkappa, \Upsilon\mu) = |\Upsilon\varkappa - \mp\mu| = 0$, we have

$$a\left[\hbar(\mu, \Upsilon\varkappa) + \hbar(\varkappa, \Upsilon\mu)\right] + b\left[\hbar(\varkappa, \Upsilon\varkappa) + \hbar(\mu, \Upsilon\mu)\right] + \left[1 - (2a + 2b)\right]\hbar(\varkappa, \mu) \geq 0 = \hbar(\Upsilon\varkappa, \Upsilon\mu).$$

Case 2 For $\varkappa = \frac{1}{3}$ and $\mu \neq \frac{1}{3}$, we have $\hbar(\Upsilon\varkappa, \Upsilon\mu) = \frac{1}{2}|\mu - 1|$ and

$$a\left[\hbar(\mu, \Upsilon\varkappa) + \hbar(\varkappa, \Upsilon\mu)\right] + b\left[\hbar(\varkappa, \Upsilon\varkappa) + \hbar(\mu, \Upsilon\mu)\right] + \left[1 - (2a + 2b)\right]\hbar(\varkappa, \mu)$$
$$= \frac{1}{6}\left[|\mu| + \left|\frac{1}{3} - \frac{1-\mu}{2}\right|\right] + \frac{1}{6}\left[\frac{1}{3} + \left|\mu - \frac{1-\mu}{2}\right|\right] + \left[1 - (\frac{1}{3} + \frac{1}{3})\right]\left|\frac{1}{3} - \mu\right| \geq \frac{1}{6}|\mu| + \frac{7}{36}|3\mu - 1|$$
$$> \frac{1}{2}|\mu - 1| = \hbar(\Upsilon\varkappa, \Upsilon\mu).$$

Case 3 For $\varkappa \neq \frac{1}{3}$ and $\mu \neq \frac{1}{3}$, we have $\hbar(\Upsilon\varkappa, \Upsilon\mu) = |\Upsilon\varkappa - \mp\mu| = \left|\frac{1-x}{2} - \frac{1-\mu}{2}\right| = \frac{1}{2}|\varkappa - \mu|$ and

$$a\left[\hbar(\mu, \Upsilon\varkappa) + \hbar(\varkappa, \Upsilon\mu)\right] + b\left[\hbar(\varkappa, \Upsilon\varkappa) + \hbar(\mu, \Upsilon\mu)\right] + \left[1 - (2a + 2b)\right]\hbar(\varkappa, \mu)$$
$$= \frac{1}{6}\left[\left|\mu - \frac{1-x}{2}\right| + \left|x - \frac{1-\mu}{2}\right|\right] + \frac{1}{6}\left[\left|x - \frac{1-x}{2}\right| + \left|\mu - \frac{1-\mu}{2}\right|\right] + \left[1 - (\frac{1}{3} + \frac{1}{3})\right]|x - \mu|$$
$$= \frac{1}{12}\left[|2\mu + \varkappa - 1| + |2\varkappa + \mu - 1|\right] + \frac{1}{12}\left[|3x - 1| + |3\mu - 1|\right] + \frac{1}{3}|x - \mu| \geq \frac{1}{12}|\mu - x|$$
$$+ \frac{1}{12}|3\varkappa - 3\mu| + \frac{1}{3}|x - \mu| = \frac{2}{3}|x - \mu|$$
$$\geq \frac{1}{2}|\varkappa - \mu| = \hbar(\Upsilon\varkappa, \Upsilon\mu).$$

In the all above cases we have $\hbar(\Upsilon\varkappa, \Upsilon\mu) \leq a\left[\hbar(\mu, \Upsilon\varkappa) + \hbar(\varkappa, \Upsilon\mu)\right] + b\left[\hbar(\varkappa, \Upsilon\varkappa) + \hbar(\mu, \Upsilon\mu)\right] + \left[1 - (2a + 2b)\right]\hbar(\varkappa, \mu)$, therefore Υ become an $a - b-$generalized nonexpansive mapping.

Now, we show that iteration process (1) converges strongly and Δ-converges to fixed point $\varpi = \frac{1}{3}$.

Choosing $\alpha_n = \frac{n}{2n+3}$ for all $n \geq 1$, the hypotheses of Lemma 3 are verified. Since the conditions of Theorem 3 and Theorem3, iteration process (1) converges strongly and Δ-converges to fixed point $\varpi = \frac{1}{3}$.

In this study, firstly, a new class of generalized nonexpansive mapping called $a - b-$generalized nonexpansive mapping has been introduced in hyperbolic space. Additionally, we construct the form in hyperbolic space of the Mann iteration process, which is well-known in the literature. Finally, we prove convergence theorems for $a - b-$generalized nonexpansive mappins in a uniformly convex hyperbolic space using the modified form of the Mann iteration process.

The author thanks the editor and the reviewers for their helpful comments and suggestions.

References

[1] Abbas, M., Nazir, T., A new faster iteration process applied to constrained minimizationand feasibility problems, Matematicki Vesnik, 66(2) (2014), 223–234.

[2] Adeyemi, T. A., Akutsah, F., Mebawondu, A. A., Adewole, M. O., and Narain, O. K., The existence of a solution of the nonlinear integral equation via the fixed point approach, Adv. Math. Sci. J., 10 (2021), 2977–2998.

[3] Ali, J., Ali, F., Kumar, P.: Approximation of fixed points for Suzuki's generalized non-expansive mappings. Mathematics. 7(6), 522 (2019)

[4] Aoyama, K., Kohsaka, F.: Fixed point theorem for α-nonexpansive mappings in Banach spaces. Nonlinear Anal. 74(13), 4387–4391 (2011)

[5] Bauschke, H. H. and Combettes, P. L., Convex analysis and monotone operator theory in Hilbert spaces, Springer, New York, 2011

[6] Browder, F. E., Nonexpansive nonlinear operators in a Banach space, Proc. Nat. Acad. Sci. USA.,54 (1965), 1041–1044.

[7] Chuadchawna, P., Farajzadeh, A., Kaewcharoen, A., Fixed-point approximation of generalized nonexpansive mappings via generalized M-iteration in hyperbolic spaces, Int. J. Math. Sci., 2020 (2020), 1-8.

[8] Dhompongsa, S. and Panyanak, B., On 4-convergence theorems in CAT(0) spaces, Comput. Math. Appl., 56 (2008), No. 10, 2572–2579

[9] Goebel, K. and Kirk, W. A., Iteration processes for nonexpansive mappings, in Singh, S. P., Thomeier, S. and Watson, B., (Eds), Topological Methods in Nonlinear Functional Analysis, Contemp. Math., vol. 21, Am. Math. Soc., Providence, 1983, 115–123

[10] Goebel, K. and Reich, S., Uniform convexity, hyperbolic geometry and nonexpansive mappings, Marcel Dekker, New York, 1984

[11] Khan, A. R., Fukhar-ud-din, H. and Khan, M. A. A., An implicit algorithm for two finite families of nonexpansive maps in hyperbolic spaces, Fixed Point Theory Appl., 2012, (2012), No. 54, 1–12

[12] Kirk, W. A., Panyanak, B., A concept of convergence in geodesic spaces, Nonlinear Anal. Theory Methods Appl., Ser. A, Theory Methods, 68 (12) (2008), 3689–3696.

[13] Kohlenbach, U., Some logical metatheorems with applications in functional analysis, Trans. Am. Math. Soc., 357 (2005), No. 1, 89–128

[14] Leustean, L., Nonexpansive iterations in uniformly convex W-hyperbolic spaces, in: Leizarowitz, A., Mordukhovich, B. S., Shafrir, I. and Zaslavski, A. (Eds), Nonlinear Analysis and Optimization I: Nonlinear Analysis, Contemp. Math., vol. 513, Am. Math. Soc., 2010, 193–209

[15] Lim, T. C., Remarks on some fixed point theorems, Proc. Am. Math. Soc., 60 (1976), No. 1, 179–182

[16] Pandey, R., Pant, R., Rakocevic, V., Shukla, R.,: Approximating fixed points of a general class of nonexpansive mappings in Banach spaces with applications. Results Math. 74(1), Article No. 7 (2019)

[17] Reich, S. and Shafrir, I., Nonexpansive iterations in hyperbolic spaces, Nonlinear Anal., 15 (1990), No. 6, 537–558

[18] Shimizu, T. and Takahashi, W., Fixed points of multivalued mappings in certain convex metric spaces, Topol. Methods Nonlinear Anal., 8 (1996), No. 1, 197–203

[19] Suzuki, T., Fixed point theorems and convergence theorems for some generalized nonexpansive mappings, J. Math. Anal. Appl. 340 (2008), no. 2, 1088–1095.

[20] Sahin, A. and Basarir, M., "Some convergence results for nonexpansive mappings in uniformly convex hyperbolic spaces," Creat. Math. Inform., vol. 26, no. 3, pp. 331–338, 2017.

[21] Takahashi, W., A convexity in metric spaces and nonexpansive mappings, Kodai Math. Semin. Rep., 22, (1970), No. 2, 142–149

[22] Uddin, I. and Imdad, M., On certain convergence of S-iteration scheme in CAT(0) spaces, Kuwait J. Sci., 42 (2015), No. 2, 93–106

[23] Ullah, K., Ahmad, J., & Sen, M. D. L. (2020). On generalized nonexpansive maps in Banach spaces. Computation, 8(3), 61.

MANAS Journal of Engineering
ISSN 1694-7398 | e-ISSN 1694-7398

Volume 11, Issue 2, (2023) Pages 229-234
https://doi.org/10.51354/mjen.1369636

Extracting book titles from book recommendation videos using a deep learning approach

Bartu Sarımehmetoğlu[1,*], Hamit Erdem[2]

[1] Başkent University, Institute of Science, Department of Electrical and Electronics Engineering, Ankara/Turkiye
bartusari96@gmail.com, ORCID: 0000-0002-4778-0580
[2] Başkent University, Institute of Science, Department of Electrical and Electronics Engineering, Ankara/Turkiye
herdem@baskent.edu.tr, ORCID: 0000-0003-1704-1581

ABSTRACT

Extracting text from images and videos is an emerging field of research with a wide range of applications, including video search, video editing, and translation. Nowadays, book promotion videos in different languages are shared on social media and especially on YouTube. In this study; It is recommended to take book titles through book promotion videos. The developed system takes video as input and separates the names of the books. The viewer can select the desired book by clicking on the detected book titles and watch the relevant part of the video. This application result in time saving by the viewer. In order to achieve this application, a deep learning-based system was developed to retrieve the names of books from videos. YOLO-based method was used in the study. Different YOLO algorithms were used in the study, and YOLOv5 was found to be more successful. This study contributes to the field of text extraction and video analysis by developing a deep learning-based approach to extract book titles from book promotion videos.

ARTICLE INFO

Research article

Received: 1.10.2023
Accepted: 21.11.2023

Keywords:
Book promotion videos,
book titles,
deep learning,
YOLOv5,
time saving

*Corresponding author

1. Introduction

With the rapid development of visual media, obtaining different data from visual image and video media is increasing. Part of the work in this field is to obtain texts in the form of text from videos and images. Text information obtained from the environment can be used in areas such as image searching, mobile robot applications, instant translation, and industrial automation [1]. In the texts obtained from the video and image; players' names, venue names, warning signs, advertising signs, traffic-related explanations and other important information can be extracted [2]. Text extraction from images involves three main steps: detection, localization, and recognition. These steps can be performed individually or end-to-end. In recent studies, deep learning methods are also used in extracting text from images along with other methods [3,4,5]. Automatically extracting book titles from book trailers can help viewers find books they are interested in more quickly and easily. This can be achieved using deep learning methods. Similar studies have been conducted on determining the book title from the book cover or video. Histogram method was used in the study conducted by In Seop Na [6]. In this study, the pictures of 100 books were investigated, and the name of the book was found by extracting meaning from the book cover. In another study, images of book covers were used as input in a similar manner [7]. Matlab software was used in the relevant study. As in other fields, deep learning method has been applied to extract the book title [8]. In the study, a dataset consisting of 10 books was used for the "Optical Character Recognition (OCR)" application. In recent studies [9], the image matching method was applied. 1400 images obtained from 200 books were used in the study.

In this study, a YOLO (You Only Look Once) based method, one of the deep learning methods, was used. The developed software takes the video promotional video as input and quickly lists the names of the books in the promotional video under the video. The viewer can select the book they are interested in and watch only the relevant part of the video. This allows them to use their time efficiently without having to watch the entire video. This process aims to highlight the important content of the video and eliminate the need for users to scan or watch long videos.

Social media is now a popular platform for video book promotions in many different languages. The person who is interested in the subject has to watch the entire video without knowing how many books and which books are in these videos. In this study, it writes the names of the introduced books at the bottom of the video as an option. The process performed is a deep learning-based text extraction process from the video. The user can watch only the relevant part of

the video by clicking on the name of the book that he is interested in. This saves time instead of watching the entire video. To perform the process, text extraction from video based on YOLOv4, YOLOv5 and YOLOv7 was performed and the success of the process was tested according to standard success criteria.

2. Problem definition and related work

Nowadays, video book promotions are widely carried out on social platforms in many different languages. Images taken from 4 different videos, as examples of these videos, are given in Fig. 1. These videos are used to convey the content and features of the books to the viewers. In these videos, the presenter briefly introduces approximately 5 to 10 books in approximately 25-30 minutes. For viewers, it is important to save time by being able to see which books are in these videos without watching the entire video and automatically going to the book they want to watch. Because, by using deep learning methods, studies such as extracting important information from video book trailers and automatically summarizing these videos can be done. Thus, viewers can reach the books they are interested in faster, make book selection easier, save time and improve their book reading experience.

Figure 1. *Images taken from 4 different book promotion videos on YouTube [10]*

Automatic summarization of video book trailers can enable viewers to access the books they are interested in faster, make book selection easier, and improve their book reading experience. Deep learning is a powerful tool for automatically summarizing video book trailers. Deep learning methods make sense of the content of videos using image processing, natural language processing and machine learning techniques. These techniques are used to detect objects and events in the video, analyze speech and text, and summarize the content of the video using this information. Some previous studies have proposed a method that uses image processing techniques to detect objects and events in video [11]. These studies produce summaries that summarize key scenes or conversations in the video. Some other studies have used natural language processing techniques to analyze speech and text in video. These studies produce video summaries that provide an overview of the content in a more general way [12]. In more complex studies; image processing, natural language processing and machine learning techniques were used together [13]. These studies produce summaries that more accurately and concisely summarize the content of the video.

2.1. Extracting text from video and image

Extracting text from images is a research field that has gained great importance today. Studies in this field offer the ability to automatically recognize and extract text in digital images and documents. This process involves a combination of image processing and optical character recognition (OCR) techniques. The process of extracting text from an image basically consists of image loading, pre-processing, character recognition and text extraction steps. Image processing techniques includes processes such as contrast enhancement, noise removal and edge detection to make text in images more distinguishable. Optical character recognition (OCR) methods recognize and extract text through steps such as character segmentation, character recognition and extraction of results. The issue of extracting text from the image is used in many application areas such as digitization of documents, research and text mining, and electronic document management. Studies carried out in this field focuses on obtaining more accurate and reliable text extraction results by using advanced algorithms, deep learning techniques and large datasets.

Deep learning techniques, which are among the methods used in text extraction from images, are an approach that can analyze complex data structures and produce high-performance results. For this reason, the use of deep learning methods in text extraction studies from videos and images is becoming increasingly common. Deep learning methods can achieve a higher success rate in extracting text from video and images than traditional methods. Therefore, deep learning methods form the basis of research in this field. For example; in the study [14], a deep learning-based system was developed to extract text from a video. This system was able to detect text in the video with an accuracy rate of over 95%. In the study [15], a deep learning-based system was developed to extract text from an image. This system was able to detect text in the image with an accuracy rate of over 98%. The development and improvement of these techniques aims to obtain more accurate and efficient text extraction results. Text extraction steps are as follows.

- Input image
- Location determination
- Verifying
- Segmentation
- Recognition
- Character sequence

3. Materials and methods

In this study, a YOLO-based study, one of the deep learning algorithms, was conducted to extract book names from the book promotional videos. These videos are collected from YouTube. The performance of the proposed system tested with unseen video during training phase. The study was carried out using Python language as software. The display card used in the study is GeForce RTX 3060.

3.1. YOLO-based image extraction

YOLO-based methods developed to obtain real-time and precise results, provide great success in the important task of extracting text from images. YOLO is a fast deep learning model that performs object detection and classification simultaneously. It divides the image into small cells and uses a customized CNN to detect objects in each cell. In this way, it can accurately identify and extract regions containing text by estimating the bounding boxes and class probabilities of objects. YOLO-based methods can improve text detection and extraction capabilities by training on a large dataset. The methods provide high accuracy, real-time performance and general applicability, making it possible to automatically process and understand text-based data.

3.2. YOLO and CNN comparison

YOLO is a fast and effective deep learning based classification method used for object detection and classification. YOLO is a CNN-based model and detects objects by analyzing the image one at a time. One of the key differences between YOLO and CNNs is that YOLO does object detection and classification in a single gateway. This makes YOLO faster and more efficient than traditional CNNs. Another important feature of YOLO is that it is based on a pre-trained CNN model. This allows YOLO to be trained with less data and perform better. Overall, YOLO is an effective method for fast and real-time object detection. By quickly and efficiently analyzing information from image data, YOLO can accurately detect and classify objects.

3.3. Training a model in YOLO

YOLO as a deep learning algorithm is an image-based object detection algorithm. It is used to detect objects YOLO provides an effective solution for fast and real-time object detection. Its basic idea is to analyze an image layer by layer and predict object bounding boxes and class probabilities. YOLO divides the image into many small cells and places a customized CNN in each cell to predict one or more objects. The predictions for each cell are object bounding boxes that start at the center of the cell and scale according to the dimensions of the cell. Along with each bounding box, probability values are also estimated for that object's possible class label. YOLO divides the image into a grid and for each grid cell, if there is an object in that cell; it estimates the object's class, coordinates and dimensions. In this way, multiple objects can be detected on a single image and these objects can be classified and positioned. YOLO can analyze an image for multiple objects simultaneously and predicts bounding box and class probabilities for each object. This gives effective results even when objects are close together or overlapping. Moreover, YOLO is an effective and fast deep learning method for real-time object detection. It performs multi-object detection by simultaneously estimating the bounding boxes and class probabilities of objects on the image. One of the biggest advantages of YOLO is that it works faster than other object detection algorithms. Various software was used in the study. This software and their role in the training system are presented in Table I.

Table I. *Software used in the proposed system*

Software Used	Its Role in the System
OpenCV	Image processing and machine learning
Torch-PyTorch	Deep learning
Open Images Dataset	Creating a data set
EasyOCR	Optical character recognition library (text detection)
CVAT	Extraction of unwanted data
Google Colab	Model training

3.4. Performance measuring functions

During the training process of proposed model, various loss functions (Box Loss, Object Loss, Class Loss, mean Average Precision) and performance criterias (Precision, Recall, F1 score) are used to evaluate the performance of the applied model. These function and metrics which are uses for similar classification are as follows.

- Box Loss: It is a loss function used in object detection problems. It is an optimization goal to improve the accuracy and precision of the model by measuring the difference between the actual and predicted bounding boxes.
- Object Loss: It is a loss function used in object detection problems. It is an objective function to optimize the model's ability to detect correct objects by evaluating the objectness of real and predicted objects.
- Class Loss: It is a loss function used in object classification problems. It is an optimization goal to improve the model's ability to predict correct classes by measuring the difference between true and predicted classes.

- mAP (mean Average Precision): It is a value used to measure the performance of object detection or object classification models. By evaluating the similarity of actual and predicted object bins, it combines the model's metrics such as precision and recall and measures overall performance.
- Precision: It is the ratio of positive examples predicted by a classification model among true positive examples. In other words, it is a metric that measures how accurately the model classifies true positives.
- Recall: It is the ratio of true positive samples among predicted positive samples. That is, it is a measure of how many the model correctly detected and how many it missed.

3.5. YOLOv5 and YOLOv7

YOLOv5 is a deep learning based learning model used for object detection. In this study, 1000 datasets of books were trained with the YOLOv5 model to detect the books and extract the titles of the detected books. The output graphic results of the training are presented in Fig. 2 and Fig. 3. YOLOv7 is the latest version of the YOLO series, YOLOv7 is specifically designed for real-time and fast object detection. This model is particularly advantageous in applications such as autonomous vehicles, security systems and object tracking. In this study, a dataset of 1000 books was trained with the YOLOv7 model. The output graphical results of the training are given in Fig. 4 and Fig. 5.

4. Results and discussion

In this study, a system was developed to automatically summarize and make book promotional videos more understandable using the YOLO algorithm. The book names in the book promotion videos were read and sorted, and then these book names were presented to the user in the form of an interface. You can get an idea about the video through this interface, and at the same time, when you click on any book on the interface, you can automatically and directly go to that book and get an idea about the book.

To evaluate the performance of the proposed system, randomly selected book promotion videos from YouTube were uploaded to the system and their performance was analyzed for different languages.

To train the model, a system compose of RTX3060 graphics card was used to meet the GPU needs of the deep learning algorithm. Each training took an average of 18 hours. 80% of the data set was used for training, 10% for testing and 10% for validation. The number of epochs is 99.

Then, different versions of CNN based YOLO algorithms (YOLO 4, YOLO 5, YOLO 7) used for training of the proposed model. A dataset of 1000 books was trained with different models under the same conditions. The system worked successfully when tested with all these versions. After training with YOLOv5 and YOLOv7 models, classification performance tested considering standard criteria. According to the results obtained, the YOLOv5 was more successful according to the precision and F1 score criteria. Additionally, the confusion matrixes related to classification results presented in Table II and III.

Table II. *Comparison of YOLOv5 and YOLOv7 models used in the study in terms of Precision, Recall and F1 Score*

Metrics	Precision $Precision = \frac{TP}{TP + FP}$	Recall $Recall = \frac{TP}{TP + FN}$	F1 Score $F_1 = 2 * \frac{precision * recall}{precision + recall}$
YOLOv5	%90	%80	%85
YOLOv7	%80	%80	%80

Table III. *Confusion matrix table for YOLOv5 and YOLOv7*

Actual Class	YOLOv5	YOLOv7
Positive	90	80
Negative	10	20

Table IV. *Comparison of YOLOv5 and YOLOv7 models used in the study as mAP_0.5 and mAP_0.5:0.95*

	mAP_0.5	mAP_0.5:0.95
YOLOv5	%87	%65
YOLOv7	%82	%62

Table V. *Comparison of YOLOv5 and YOLOv7 models used in the study in terms of Box_Loss, Obj_Loss and Class_Loss*

	Box_Loss	Obj_Loss	Class_Loss
YOLOv5	0.01	0.008	0
YOLOv7	0.03	0.011	0

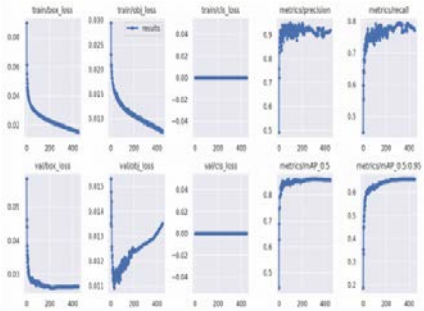

Figure 2. *YOLOv5 training results due to losses function and mAP*

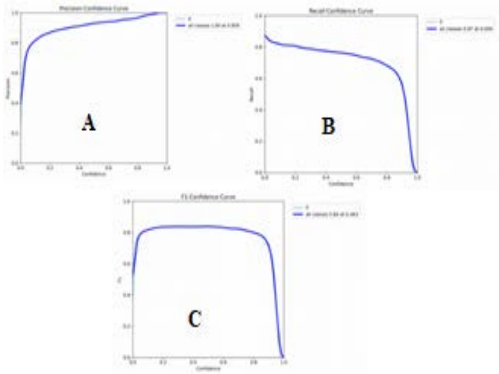

Figure 3. *YOLOv5 training results in Precision (A), Recall (B) and F1 Score (C)*

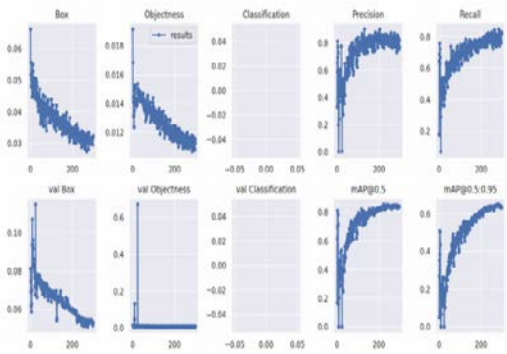

Figure 4. *YOLOv7 training results*

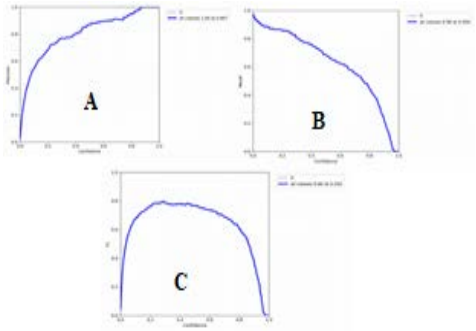

Figure 5. *YOLOv7 training results in Precision (A), Recall (B) and F1 Score (C)*

An example of the system output generated at the end of the study is shown in Fig. 6.

YOLOv5 exhibits less FN and FP error rates than YOLOv7. This means that YOLOv5 has the ability to more accurately predict true positives (TP) and true negatives (TN). This result shows that YOLOv5 is a more accurate classification model. After the training with the YOLOv5 and YOLOv7 models, the results obtained regarding these parameters are given in Table IV and Table V.

Based on the results, it can be said that the YOLOv5 model is better in terms of accuracy on the book dataset. As a final test, Table VI shows the results of the system for book promotion videos (in different languages). The results were interpreted based on the number of books found by the system in the video and the number of book names found correctly. The system managed to find books in the video with an average rate of 98%. This shows that the system is successful in detecting books. However, there is less margin of error in the system when finding book titles.

Table VI. *Performance of the system on randomly selected book promotion videos*

YouTube video address	Input videos	Detected books	Success rate	Performance of the system
https://www.youutube.com/watch?v=R2Zt-3spWFQ	14	13	%93	%100 **(English)**
https://www.youutube.com/watch?v=82vJPdsJyHU	17	16	%94	%100 **(Turkish)**
https://www.youutube.com/watch?v=_zCTZM92Ju0	10	10	%100	%100 **(Turkish)**
https://www.youutube.com/watch?v=M0qL4zzIuC8	12	12	%100	%100 **(English)**
https://www.youutube.com/watch?v=7d4s0kdQFeE	17	16	%94	%100 **(Turkish)**
https://www.youutube.com/watch?v=eojGtx9g0kg	6	6	%100	%100 **(German)**
https://www.youutube.com/watch?v=yHXuBmLAJN8	10	10	%100	%100 **(French)**
TOTAL	86	83	%97	%100

Figure 6. *Screenshot of the system (Titles of detected books). Source video from YouTube [10]*

References

[1]. He, J., Zhang, Z., Yang, W., Zhang, J., Zhang, Y., and Zhang, H. (2018). Scene Text Detection and Recognition: The Deep Learning Era. International Journal of Computer Vision, 129(7), 1641-1671.

[2]. Chen, D., Odobez, J.-M., and Bourlard, H. (2014). Text detection and recognition in images and video frames. IEEE Transactions on Pattern Analysis and Machine Intelligence, 37(3), 697-711.

[3]. Busta, M., Neumann, L., and Matas, J. (2017). Deep textspotter: an end-to-end trainable scene text localization and recognition framework. In Proceedings of the IEEE international conference on computer vision (pp. 2204-2212).

[4]. Liu, X., Meng, G., and Pan, C. (2019). Scene text detection and recognition with advances in deep learning: a survey. International Journal on Document Analysis and Recognition, 22, 143-162.

[5]. Chu, W.-S., Lin, Y.-H., & Yang, Y.-H. (2012). Title extraction from book cover images using histogram of oriented gradients and color information. International Journal of Contents, 8(4), 95-102.

[6]. Na, I. S. (2016). A Novel Scene Text Detection Method Using Histogram-Based Thresholding. IEEE Transactions on Image Processing, 25(2), 675-689.

[7]. Chen, Y., Liu, J., and Yu, K. (2018). Book Cover Image Recommendation Using Deep Learning. In Proceedings of the 2018 ACM Multimedia Conference on Multimedia Information Retrieval (MIR) (pp. 530-537).

[8]. Al-Omari, A. A., Al-Duwairi, M., and Al-Omari, K. (2020). Book Title Extraction from Book Cover Images Using Deep Learning. IEEE Transactions on Image Processing, 29(5), 2540-2551.

[9]. Akar, H. A., Al-Omari, A. A., and Al-Omari, K. (2022). Book Title Extraction from Book Cover Images Using Image Matching. IEEE Transactions on Pattern Analysis and Machine Intelligence, 44(10), 2726-2739.

[10]. https://www.youtube.com

[11]. Li, Y., Fu, X., and Wang, J. (2019). A Survey on Object Detection and Tracking in Videos. IEEE Transactions on Pattern Analysis and Machine Intelligence, 41(11), 2789-2812.

[12]. Li, Z., Zhang, K., Mei, T., and Rui, Y. (2021). A Survey on Video Summarization Techniques. IEEE Transactions on Multimedia, 23(1), 281-304.

[13]. Li, H., Wang, Y., and Wang, W. (2022). A Survey on Multimodal Machine Learning for Video Understanding. IEEE Transactions on Pattern Analysis and Machine Intelligence, 44(10), 2711-2725.

[14]. He, J., Zhang, Z., Yang, W., Zhang, J., Zhang, Y., and Zhang, H. (2022). Deep Learning for Video Text Extraction: A Survey. IEEE Transactions on Pattern Analysis and Machine Intelligence, 44(10), 2699-2710.

[15]. He, J., Zhang, Z., Yang, W., Zhang, J., Zhang, Y., and Zhang, H. (2022). Deep Learning for Text Extraction from Images: A Survey. IEEE Transactions on Pattern Analysis and Machine Intelligence, 44(10), 2684-2698.

MANAS Journal of Engineering
ISSN 1694-7398 | e-ISSN 1694-7398

Volume 11, Issue 2, (2023) Pages 235-240
https://doi.org/10.51354/mjen.1372839

A new approach for the bigeometric newton method

Numan Yalçın[1] , Ercan Çelik[2,*]

[1] Department of Electronics and Automation, Vocational School of Gumushane, Gumushane, TURKEY, numan@gumushane.edu.tr, ORCID: 0000-0002-8896-6437
[2] Department of Applied Mathematics and Informatics, Kyrgyz-Turkish Manas University, Bishkek, Kyrgyzstan, ercan.celik@manas.edu.kg, ORCID: 0000-0001-5971-7653

ABSTRACT

In this study, quadratic convergent new bigeometric Newton's method (nBGNM) was developed. For this, the basic definitions and theorems of bigeometric analysis, which is one of the non-Newtonian analysis, were used. Using the bigeometric Taylor expansion, a convergence analysis of this new method was given. Also, the new bigeometric Newton method (nBGNM) was compared in detail with the geometric (multiplicative) Newton method (GNM) and the classical Newton method (NM).

ARTICLE INFO

Research article

Received: 8.10.2023
Accepted: 6.12.2023

Keywords:
Bigeometric analysis,
Bigeometric Newton method,
Quadratic convergence,
Bigeometric Taylor expansion

*Corresponding author

1. Introduction

Solutions of nonlinear functional (algebraic, differential integral etc.) equations are very important in applied sciences and engineering. Newton's method is one of the most widely used methods in classical analysis to analyze the solutions of such equations [1-4]. This method was introduced by Newton for finding the real valued function $F:\mathbb{R}\to\mathbb{R}$ of a real variable from the equation in the form of $F(t)=0$. As is known, Newton's method is the most common method used to approximate the real root of a function. The classical Newton's method is given by

$$t_{n+1}=t_n-\frac{F(t_n)}{F'(t_n)},\quad n=0,1,2,\ldots.$$

That is, the classical Newton's method has an iterative procedure that includes the function and its derivative.
In the last quarter of the 19th century, Grossman and Katz defined non-Newtonian analysis [5]. The importance of these new analysis, in which different arithmetic operations are used, has been better understood in recent years. Especially, Bashirov et al., managed to draw the attention of researchers to multiplicative analysis by their study in 2008 [6]. Thus, researchers have shown great interest in developing the theory and application of multiplicative (geometric) analysis [7-11,12-17,18-26]. In geometric analysis, important studies of numerical analysis were made by Bilgehan, Mısırlı, Gürefe, Riza, Ozyapici, Waseem [27-33]. Unal et al. examined Newton's method and cubic convergence in geometric analysis in a study they conducted in 2017 [34].Newton method was given for multiplicative and Volterra Calculi by Ozyapici et al in 2016 [31]. In this study, the Bigeometric Newton method will be given with the help of the Bigeometric Taylor expansion. Also, the convergence of the bigeometric Newton method will be examined. Then bigeometric Newton's method will be compared with Newton's methods in classical analysis and multiplicative analysis. Therefore some basic definitions and theorems of bigeometric analysis that can be found in the studies of [35-42] will be given.

Definition 1. *(see [35-38])* Let $f:\mathbb{R}_{exp}\to\mathbb{R}_{exp}$ be a function. The bigeometric derivative of the function f is given by

$$\frac{d^{\pi}f}{dt}(t)=f^{\pi}(t)=\lim_{h\to 0}\left\{\frac{f[(1+h)\cdot t]}{f(t)}\right\}^{1/h}$$

The relationship of the bigeometric derivative with the classical derivative and the geometric derivative is given as

$$f^{\pi}(t) = \exp\left\{t \cdot \frac{f'(t)}{f(t)}\right\} = f^{*}(t)^{t}$$

Theorem 1. *(see [35-38])* Let f, g and h be bigeometric differentiable functions and $k > 0$ is an arbitrary constant then the bigeometric differentiation rules are valid as,

i) $(k.f)^{\pi}(t) = f^{\pi}(t)$,

ii) $(f+g)^{\pi}(t) = f^{\pi}(t)^{\frac{f(t)}{f(t)+g(t)}} \cdot g^{\pi}(t)^{\frac{g(t)}{f(t)+g(t)}}$,

iii) $(f \cdot g)^{\pi}(t) = f^{\pi}(t) \cdot g^{\pi}(t)$,

iv) $\left(\frac{f}{g}\right)^{\pi}(t) = \frac{f^{\pi}(t)}{g^{\pi}(t)}$,

v) $(f^{h})^{\pi}(t) = f^{\pi}(t)^{h(t)} \cdot f(t)^{t \cdot h'(t)}$,

vi) $(f \circ g)^{\pi}(t) = f^{\pi}[g(t)]^{g'(t)}$.

Theorem 2. *(see [35-38]) (Bigeometric Taylor theorem)*

Let D be an open interval and let $f: D \to \mathbb{R}_{exp}$ is $(n+1)$ times bigeometric differentiable on D. Then for any $t, t+h \in D$, there exists a number $\theta \in (0,1)$ such that

$$f(t+h) = \prod_{i=0}^{n}\left[f^{\pi(i)}(t)\right]^{\frac{\ln\left(1+\frac{h}{t}\right)^{i}}{i!}} \cdot \left[\left(f^{\pi(n+1)}(t+\theta \cdot h)\right)^{\frac{\ln\left(1+\frac{h}{t}\right)^{n+1}}{(n+1)!}}\right]$$

Definition 2. *(see [4])* If the sequence $\{t_i\}$ tends to a limit r in such a way that

$$\lim_{i\to\infty} \frac{t_{i+1} - r}{(t_i - r)^{p}} = C$$

for some $C \neq 0$ and $p \geq 1$, p is called as the order of convergence of the sequence and C is known as the asymptotic error constant.

Definition 3. *(see [3])* Let r be a root of the function $f(t)$ and suppose that t_{i+1}, t_i and t_{i-1} are three consecutive iterations closer to the root r. Then, the computational order of convergence (COC) ρ can be approximated using the formula $\rho \approx \frac{\ln|(t_{i+1}-r)/(t_i-r)|}{\ln|(t_i-r)/(t_{i-1}-r)|}$.

2. New Bigeometric Newton Method

In bigeometric calculus, Taylor expansion of function in neighboord a point t_0 can be written [42] as;

$$f(t_0+h) = \prod_{i=0}^{\infty}\left[f^{\pi(i)}(t_0)\right]^{\frac{\left[\ln\left(1+\frac{h}{t_0}\right)\right]^{i}}{i!}} \quad (1)$$

Let $t_0 + h = t$. We can write following equation using the first two terms of above equation:

$$f(t) = f(t_0) \cdot [f^{\pi}(t_0)]^{\ln\left(\frac{t}{t_0}\right)}. \quad (2)$$

If we calculate logarithm of the equation (2), we have

$$\ln f(t) = \ln f(t_0) + \ln\left(\frac{t}{t_0}\right) \cdot \ln f^{\pi}(t_0).$$

If we consider that $f(r) = 1$, we get

$$r = t_0 \cdot e^{-\frac{\ln f(t_0)}{\ln f^{\pi}(t_0)}}$$

Hence, we obtain new bigeometric Newton method as

$$t_{n+1} = t_n \cdot e^{-\frac{\ln f(t_n)}{\ln f^{\pi}(t_n)}} \quad (3)$$

Equivalent in classical analysis of iterative formula (3) is also that

$$t_{n+1} = t_n \cdot e^{-\frac{\ln f(t_n)}{t_n \cdot (\ln f)'(t_n)}}. \quad (4)$$

Remark 1. The equation (4) can be written as

$$\frac{t_{n+1}}{t_n} = e^{-\frac{\ln f(t_n)}{t_n \cdot (\ln f)'(t_n)}}. \quad (5)$$

Since right on the handle of the equation (5) is positive for each t_n, markers of t_{n+1} and t_n are been same as. This imply that markers of root of function and initial point are been same as. That is; for positive root, we must choose a positive initial point. Similarly, for negative root, we must choose a negative initial point.

3. Convergence of the method

Iteration function of the bigeometric Newton Method is

$$g(t) = t \cdot e^{-\frac{\ln f(t)}{t\cdot(\ln f)'(t)}}$$

The derivative of the function $g(t)$ is

$$g'(t) = e^{-\frac{\ln f(t)}{t\cdot(\ln f)'(t)}} - \frac{t\cdot\left[\frac{f'(t)}{f(t)}\right]^2 - \left[\frac{f'(t)}{f(t)} + t\cdot\frac{f''(t)\cdot f(t) - \left(f'(t)\right)^2}{\left(f(t)\right)^2}\right]\cdot\ln f(t)}{t^2\cdot\left[\frac{f'(t)}{f(t)}\right]^2} \cdot e^{-\frac{\ln f(t)}{t\cdot(\ln f)'(t)}} \cdot t.$$

Considering the classical Taylor expansion of order two of $g(t_n)$ neighborhood of fixed point r and $f(r) = 1$, we obtain

$$g(t_n) = g(r) + \frac{(t_n - r)^2}{2}\cdot g''(r). \quad (7)$$

If we rearrange to the equation (7), we have

$$t_{n+1} - r = \frac{(t_n - r)^2}{2}\cdot g''(r).$$

Let $e_{n+1} = t_{n+1} - r, e_n = t_n - r$. Hence,

$$e_{n+1} = \frac{(t_n - r)^2}{2}\cdot g''(r) = \frac{{e_n}^2}{2}\cdot g''(r) \quad (8)$$

is obtained. The equation (8) implies that the bigeometric Newton method is quadratically convergent.

It is clear that the number of function evaluation in per iteration for method (3) is two. According to the definition of efficiency index [4], the efficiency index of (3) is $\sqrt{2} \cong 1.414$. Hence, the efficiency index of bigeometric Newton method defined by (3) is same as the ones of the classical Newton method and multiplicative Newton method.

4. Numerical examples

In this section, the new Bigeometric Newton method (nBGNM) obtained in this work to solve some non-linear equation $f(t) = 0$, $f(t) + 1 = 1$ for bigeometric methods. Summing the number of evaluations of function f with the number of evaluations of its derivative, the number of function evaluation (NFE) in per iteration is found. The results obtained via these methods are showed in Table 1.

The results show that nBGNM converging quadratically can compete with Newton method (NM) and GNM. Besides, nBGNM method is better than other methods in some case where newton method and multiplicative newton method diverge, such as example (b), (c). Further, in certain problems such as example (a), (d) (f), (g) and (h), nBGNM gives better results compared to NM and GNM. Also if we look closely to example (h), nBGNM that is developed in this work reaches the root in one step. This is not actually an amazing result. This case originate from bigeometric calculus.

Test functions:

- **(a)** $f(t) = \ln t - \sin(t)$, geometric and bigeometric version: $f(t) = \ln t - \sin(t) + 1$
- **(b)** $f(t) = \arctan t$, geometric and bigeometric version: $f(t) = \arctan t + 1$
- **(c)** $f(t) = t^{1/3}$, geometric and bigeometric version: $f(t) = t^{1/3} + 1$
- **(d)** $f(t) = \ln t$, geometric and bigeometric version: $f(t) = \ln t + 1$
- **(e)** $f(t) = e^{t^3+7t-30} - 1$, geometric and bigeometric version: $f(t) = e^{t^3+7t-30}$
- **(f)** $f(t) = t \cdot e^t - 1$, geometric and bigeometric version: $f(t) = t \cdot e^t$
- **(g)** $f(t) = (t-1)^6 - 1$, geometric and bigeometric version: $f(t) = (t-1)^6$
- **(h)** $f(t) = 5t^6 - 1$, geometric and bigeometric version: $f(t) = 5t^6$

.

Table 1. *Comparison of iterative methods*

	n	NFE	COC	t_n
(a), $t_0 = 1.5$				
NM	5	10	1.99	2.219107148913746
GNM	5	10	1.99	2.219107148913746
nBGNM	4	8	2.03	2.219107148913746
(b), $t_0 = 3$				
NM	-	-	-	divergence
GNM	-	-	-	divergence
nBGNM	31	62	0.95	0.000000000000000
(c), $t_0 = 3$				
NM	-	-	-	divergence
GNM	-	-	-	divergence
nBGNM	12	24	0.91	0.000000000000000
(d), $t_0 = 3$				
NM	6	12	2.00	1
GNM	-	-	-	divergence
nBGNM	5	10	2.00	1
(e), $t_0 = 3$				
NM	23	46	1.99	2.374101653848877
GNM	5	10	1.99	2.374101653848877
nBGNM	5	10	1.99	2.374101653848877
(f), $t_0 = 2$				
NM	7	14	1.99	0.567143290409784
GNM	6	12	2.00	0.567143290409784
nBGNM	5	10	1.99	0.567143290409784
(g), $t_0 = 3.5$				
NM	10	20	1.99	2
GNM	7	14	2.00	2
nBGNM	5	10	2.00	2
(h), $t_0 = 2$				
NM	10	20	1.99	0.764724491331730
GNM	8	16	1.99	0.764724491331730
nBGNM	1	2	ND	0.764724491331730

NM- Newton method
GNM- Geometric Newton method
nBGNM- New Bigeometric Newton method
ND- Not defined

n- Number of iterations
NFE- Number of functional evaluations
COC- Computational order of convergence

5. Conclusion

In this study, bigeometric Newton method is given as an an alternative to the classical Newton method with the help of bigeometric Taylor expansion. In addition, the quadratic convergence of the method is shown.

In the test functions given in this study, it has been seen that the bigeometric Newton Method is a better convergent method than the multiplicative Newton method [17] and the classical Newton method.

References

[1]. Mcbride, A. (1982). V. Hutson and J. S. Pym Applications of Functional Analysis and Operator Theory (Mathematics in Science and Engineering, Volume 146, Academic Press, London, 1980), xii 390 pp. Proceedings of the Edinburgh Mathematical Society, 25(3), 280-281.

[2]. Kreyszig, E. (1991). Introductory functional analysis with applications (Vol. 17). John Wiley & Sons.

[3]. Weerakoon, S., & Fernando, T. (2000). A variant of Newton's method with accelerated third-order convergence. Applied mathematics letters, 13(8), 87-93.

[4]. Wait, R. (1979). The numerical solution of algebraic equations. John Wiley & Sons.

[5]. Grossman M, Katz R. Non-Newtonian Calculus. Pigeon Cove, MA, USA: Lee Press, 1972.

[6]. Bashirov, A. E., Kurpınar, E. M., & Özyapıcı, A. (2008). Multiplicative calculus and its applications. Journal of mathematical analysis and applications, 337(1), 36-48.

[7]. Aniszewska, D. (2007). Multiplicative runge–kutta methods. Nonlinear Dynamics, 50(1-2), 265-272.

[8]. Bashirov, A. E., & Bashirova, G. (2011). Dynamics of literary texts and diffusion.

[9]. Bashirov, A. E., Mısırlı, E., Tandoğdu, Y., & Özyapıcı, A. (2011). On modeling with multiplicative differential equations. Applied Mathematics-A Journal of Chinese Universities, 26, 425-438.

[10]. Bashirov, A. E., & Mustafa, R. İ. Z. A. (2011). On complex multiplicative differentiation. TWMS Journal of applied and engineering mathematics, 1(1), 75-85

[11]. Bashirov, A. E., & Riza, M. (2013). On complex multiplicative integration. arXiv preprint arXiv:1307.8293.

[12]. Córdova-Lepe, F. (2006). The multiplicative derivative as a measure of elasticity in economics. TEMAT-Theaeteto Atheniensi Mathematica, 2(3).

[13]. Filip, D. A., & Piatecki, C. (2014). A non-Newtonian examination of the theory of exogenous economic growth.

[14]. Florack, L., & van Assen, H. (2012). Multiplicative calculus in biomedical image analysis. Journal of Mathematical Imaging and Vision, 42, 64-75.

[15]. Mısırlı, E., & Özyapici, A. (2009). Exponential approximations on multiplicative calculus. In Proc. Jangjeon Math. Soc (Vol. 12, No. 2, pp. 227-236).

[16]. Stanley, D. (1999). A multiplicative calculus. Problems, Resources, and Issues in Mathematics Undergraduate Studies, 9(4), 310-326.

[17]. Uzer, A. (2010). Multiplicative type complex calculus as an alternative to the classical calculus. Computers & Mathematics with Applications, 60(10), 2725-2737.

[18]. Yalcin, N., Celik, E., & Gökdoğan, A. (2016). Multiplicative Laplace transform and its applications. Optik, 127(20), 9984-9995.

[19]. Yalçın, N., & Çelik, E. (2018). The solution of multiplicative non-homogeneous linear differential equations. J. Appl. Math. Comput, 2(1), 27-36.

[20]. Yalcin, N., & Celik, E. (2018). Solution of multiplicative homogeneous linear differential equations with constant exponentials. New Trends in Mathematical Sciences, 6(2), 58-67.

[21]. Yalçın, N., & Çelik, E. Çarpımsal Cauchy-Euler ve Legendre Diferansiyel Denklemi. Gümüşhane Üniversitesi Fen Bilimleri Dergisi, 9(3), 373-382.

[22]. Yalçın, N. (2021). The solutions of multiplicative Hermite differential equation and multiplicative Hermite polynomials. Rendiconti del Circolo Matematico di Palermo Series 2, 70, 9-21.

[23]. Yalçın, N., & Dedeturk, M. (2021). Solutions of multiplicative ordinary differential equations via the multiplicative differential transform method. Aims Mathematics, 6(4), 3393-3409.

[24]. Yalçın, N., & Dedeturk, M., Solutions of Multiplicative Linear Differential Equations via the Multiplicative Power Series Method. Sigma Journal of Engineering and Natural Sciences. (In press)

[25]. Bal, A., Yalçın, N., & Dedetürk, M. Solutions of Multiplicative İntegral Equations via The Multiplicative Power Series Method. Politeknik Dergisi, 1-1.

[26]. Yalcin, N. (2022). Multiplicative Chebyshev differential equations and multiplicative Chebyshev polynomials. Thermal Science, 26(Spec. issue 2), 785-799.

[27]. Bilgehan, B. (2015). Efficient approximation for linear and non-linear signal representation. IET Signal Processing, 9(3), 260-266.

[28]. Özyapıcı, A., Riza, M., Bilgehan, B., & Bashirov, A. E. (2014). On multiplicative and Volterra minimization methods. Numerical Algorithms, 67, 623-636.

[29]. Ozyapici, A., & Bilgehan, B. (2016). Finite product representation via multiplicative calculus and its applications to exponential signal processing. Numerical Algorithms, 71, 475-489.

[30]. Misirli, E., & Gurefe, Y. (2011). Multiplicative adams bashforth–moulton methods. Numerical Algorithms, 57, 425-439.

[31]. Özyapıcı, A., Sensoy, Z. B., & Karanfiller, T. (2016). Effective root-finding methods for nonlinear equations based on multiplicative calculi. Journal of Mathematics, 2016.

[32]. Riza, M., Özyapici, A., & Mısırlı, E. (2009). Multiplicative finite difference methods. Quarterly of Applied Mathematics, 67(4), 745-754.

[33]. Waseem, M., Noor, M. A., Shah, F. A., & Noor, K. I. (2018). An efficient technique to solve nonlinear equations using multiplicative calculus. Turkish Journal of Mathematics, 42(2), 679-691.

[34]. Unal, E., Cumhur, I., & Gokdogan, A. Multiplicative Newton's Methods with Cubic Convergence. New Trends in Mathematical Sciences, 5(3), 299-307.

[35]. Grossman, M. (1983). Bigeometric calculus: a system with a scale-free derivative. Archimedes Foundation.

[36]. Riza, M., & EminaĞA, B. (2014). Bigeometric Calculus and Runge Kutta Method. arXiv preprint arXiv:1402.2877.

[37]. Riza, M., & Eminagaı, B. (2014). Bigeometric calculus—a modelling tool. Preprint.

[38]. Boruah, K., & Hazarika, B. (2016). Bigeometric Calculus and its applications. arXiv preprint arXiv:1608.08088.

[39]. Boruah, K., & Hazarika, B. (2018). Bigeometric integral calculus. TWMS Journal of Applied and Engineering Mathematics, 8(2), 374-385.

[40]. Boruah, K., Hazarika, B., & Bashirov, A. E. (2021). Solvability of bigeometric differential equations by numerical methods. Boletim da Sociedade Paranaense de Matematica, 39(2), 203-222.

[41]. Boruah, K., & Hazarika, B. (2021). Some basic properties of bigeometric calculus and its applications in numerical analysis. Afrika Matematika, 32(1-2), 211-227.

[42]. Eminağa, B. (2015). Bigeometric Taylor Theorem and its Application to the Numerical Solution of Bigeometric Differential Equations.

MANAS Journal of Engineering
ISSN 1694-7398 | e-ISSN 1694-7398

Volume 11, Issue 2, (2023) Pages 241-251
https://doi.org/10.51354/mjen.137954

A study on the admissibility of fractional singular systems with variable and constant delays

Abdullah Yiğit

Mesut ÖZATA Anatolian High School, Van, Turkey, a-yigit63@hotmail.com, ORCID: 0000-0002-0099-3095

ABSTRACT

This paper deals with fractional singular systems with mixed delays and several admissibility criteria are obtained by using Lyapunov-Krasovskii functionals, model transformation, useful lemmas, zero equations and other well-known inequalities. Finally, some numerical examples are given with graps to verify and justify the admissibility of practical systems by using our proposed methods.

ARTICLE INFO

Research article

Received:22.10.2023
Accepted: 6.12.2023

Keywords:
Admissibility,
fractional neutral
singular system,
matrix inequality,
numerical illustration,
stability,
zero equation

1. Introduction

The concept of stability, widely used in applied sciences such as mathematics, physics, engineering, and medicine, was developed by Soviet mathematician A.M. Lyapunov in the early 1900s (see [13]). This field, which continues to expand and attract researchers, has become a broad application area for time-delayed and non-delayed systems (or equations). Numerous exciting studies have been conducted on this topic, which has been addressed by many researchers, and sufficient conditions for stability have been established. Alkhazzan et al., in article [1], discussed a new class of nonlinear fractional stochastic differential equations with fractional integrals and discussed existence, uniqueness, continuity of solutions and Ulam-Hyers stability with the help of Banach contraction theorem. They supported their work with an example. Singular and non-singular fractional systems have been studied for many types of stability, such as asymptotic stability (see [2,3,4,11,12,16,22,23,24]) and Razumikhin stability [8,17]. Using the Lyapunov-Krasovskii functional approach, the stability of fractional nonlinear Caputo-Volterra integral equations was studied in article [9]. In article [15], Tunç and Tunç investigated the qualitative behavior of the solutions of Caputo Proportional derivatives of delayed integro-differential equations. In article [19], by using Lyapunov-krasovskii functional, some sufficient conditions to guarantee robust stability and asymptotic stability for indeterminate fractional singular systems with neutral and time-varying delays in terms of the linear matrix inequality were proved. For the existence and uniqueness of solutions in singular systems, the system under consideration must have the properties of impulse-free and regular. For this reason, the authors in article [19] proved that the system they discussed in the first stage has these two properties and then has asymptotic stability and robust stability. By providing these three properties simultaneously, it was proved that the system discussed in article [19] has asymptotic admissibility and robust admissibility. Moreover, the Lyapunov stability of fractional neural networks with Riemann-Liouville delay was studied in [25]. Stability and admissibility in singular and non-singular systems with non-fractional delay have also been discussed (see [5,6,18]). In addition to these studies, there are many books that researchers can benefit from. Examples include (see [7,20,21]) for singular systems and (see [10,14]) for fractional differential equations.

This study, motivated by the above discussion and article [4] and references there in, is investigated the admissibility of a certain type of delay neutral fractional singular systems by the help of Lyapunov functionals, zero equations, model transformations and other some well-known inequalities.

Some numerical examples are presented to demonstrate the applicability of the proved results.

2. Preliminaries

In this paper motivated by the above discussion and article [4] and references there in, we define a fractional neutral singular system with constant and variable delays and nonlinear perturbation as:

$$ {}_{to}D_t^q[Sx(t)+Ax(t-\tau)] = -Bx(t)+Rx(t-\sigma)+E\int_{t-\sigma}^{t} x(s)ds + Tx(t-\sigma(t))+G(x(t-\sigma(t)), \quad (1) $$

$$ x(t)=\vartheta(t), t\in[-\kappa,0], \kappa>0, \kappa\in\Re, $$

for $q\in(0,1]$, the system state $x(t)\in\Re^n$, $A,B,R,E,T\in\Re^{n\times n}$ are symmetric positive definite system matrices, the matrix $S\in\Re^{n\times n}$ is singular and satisfied $rankS=r\le n, n\ge 1$, with $\|A\|<1$, the time variable delay $\sigma(t)$ is assumed to satisfy $0\le\sigma(t)\le\sigma$ and $\dot{\sigma}(t)\le\mu$, the constant delays τ,σ are real positive numbers and $\vartheta\in C([-\kappa,0];\Re^n)$ with $\kappa=\max\{\tau,\sigma\}$. The nonlinear perturbation parameter $G(.)$ satisfying

$$ G^{\mathrm{T}}(x(t))G(x(t))\le a^2x^{\mathrm{T}}(t)x(t), \quad (2) $$

$$ G^{\mathrm{T}}(x(t-\sigma(t)))G(x(t-\sigma(t)))\le b^2x^{\mathrm{T}}(t-\sigma(t))x(t-\sigma(t)), \quad (3) $$

where a,b given any numbers.

Before moving on to the details of our study, we would like to remind of some useful definitions and lemmas that should be known.

Definition 2.1 ([4]). The Riemann-Liouville fractional integral and the derivation are defined as

$$ {}_{to}D_t^{-q}x(t)=\frac{1}{\Gamma(q)}\int_{t_0}^{t}(t-s)^{q-1}x(s)ds,\ (q>0), $$

$$ {}_{to}D_t^{q}x(t)=\frac{1}{\Gamma(n-q)}\frac{d^n}{dt^n}\int_{t_0}^{t}\frac{x(s)}{(t-s)^{q+1-n}}ds,\ (n-1\le q<n). $$

Lemma 2.1 ([4]). For $x(t)\in\Re^n$ and $p>q>0$, then

$$ {}_{to}D_t^{q}({}_{to}D_t^{-p}x(t))={}_{to}D_t^{q-p}x(t). $$

Lemma 2.2 ([4]). Let $x(t)\in\Re^n$, be a vector of a differentiable function. For positive semi-definite matrix $\mathrm{N}\in\Re^{n\times n}$ and $\forall q\in(0,1),\ \forall t\ge t_0$, then

$$ {}_{to}D_t^{q}(x^{\mathrm{T}}(t)\mathrm{N}x(t))\le 2x^{\mathrm{T}}(t)\mathrm{N}\,{}_{to}D_t^{q}x(t) $$

is satisfied.

3. Admissibility

We obtain sufficient conditions for the admissibility properties of the systems discussed in this section. We prove the regular, impulse-free, and stable states accepted as admissibility conditions in the first theorem. In the remaining four corollaries, we show that only the new systems defined by constructing new Lyapunov-Krasovskii functionals are stable, since regular and impulse-free states can be represented in a similar way. Therefore, we prove five sufficient conditions stating that these systems guarantee admissibility.

If we define a new operator like $\Omega(t)=Sx(t)+Ax(t-\tau)$, then the system (1) can be rewritten as in the form below:

$$ {}_{to}D_t^{q}\Omega(t) = -Bx(t)+Rx(t-\sigma)+E\int_{t-\sigma}^{t}x(s)ds + Tx(t-\sigma(t))+G(x(t-\sigma(t)). \quad (4) $$

Theorem 3.1. We suppose that the following hypothesis is met:

(H1) Let a,b be any numbers and $\tau>0,\sigma>0$, if there are symmetric matrices

$$ K_k=K_k^{\mathrm{T}}>0,(k=1,...,7), $$

$W_i=\mathrm{W}_i^{\mathrm{T}}>0,(i=1,4,5)$, and any suitable dimensions matrices $W_i\ (i=2,3)$ such that the following relationship is satisfied:

$$\Theta=\begin{bmatrix}\Theta_{11} & \Theta_{12} & \Theta_{13} & K_1R & K_1T & K_1 & K_1E & 0\\ * & \Theta_{22} & \Theta_{23} & W_5R & W_5T & W_5 & W_5E & \Theta_{28}\\ * & * & \Theta_{33} & 0 & 0 & 0 & 0 & 0\\ * & * & * & -K_3 & 0 & 0 & 0 & RW_4^{\mathrm{T}}R\\ * & * & * & * & \Theta_{55} & 0 & 0 & TW_4^{\mathrm{T}}R\\ * & * & * & * & * & \Theta_{66} & 0 & W_4^{\mathrm{T}}R\\ * & * & * & * & * & * & -K_7 & E^{\mathrm{T}}W_4^{\mathrm{T}}R\\ * & * & * & * & * & * & * & \Theta_{88}\end{bmatrix}<0, \quad (5)$$

where

$$\Theta_{11}=-W_1-W_1^{\mathrm{T}},\ \Theta_{12}=-K_1B+W_1S-W_2^{\mathrm{T}},$$
$$\Theta_{13}=W_1A-W_3^{\mathrm{T}},$$
$$\Theta_{22}=W_2S+S^{\mathrm{T}}W_2^{\mathrm{T}}-W_5B-BW_5^{\mathrm{T}}+K_2+K_3+\tau K_4+K_5+a^2K_6+\sigma^2K_7,$$
$$\Theta_{23}=W_2A+S^{\mathrm{T}}W_3^{\mathrm{T}},\ \Theta_{28}=-BW_4^{\mathrm{T}}R-W_5,$$
$$\Theta_{33}=W_3A+A^{\mathrm{T}}W_3^{\mathrm{T}}-K_2,$$
$$\Theta_{55}=-(1-\mu)K_5+\varepsilon b^2\mathrm{I},$$
$$\Theta_{66}=-(1-\mu)K_6-\varepsilon\mathrm{I},\ \Theta_{88}=-RW_4-W_4^{\mathrm{T}}R.$$

where ε is a positive number and I is identity matrix with appropriate dimension.

Then the zero solution of system (1) is admissible.

Proof. The proof of Theorem 3.1 is divided into two steps. The first step deals with the properties impulse free and regularity. The second step is related to the stability property. Firstly, we can write from (5) that

$$\Theta_{22}=W_2S+S^{\mathrm{T}}W_2^{\mathrm{T}}-W_5B-BW_5^{\mathrm{T}}+K_2+K_3+\tau K_4+K_5+a^2K_6+\sigma^2K_7<0.$$

Since

$$W_2S+S^{\mathrm{T}}W_2^{\mathrm{T}}+K_2+K_3+\tau K_4+K_5+a^2K_6+\sigma^2K_7>0,$$

we can write

$$\nabla=-W_5B-BW_5<0. \quad (6)$$

Because of W_5, B positive definite symmetric matrices and $rankS=r\le n, n\ge 1,$ there exist two regular matrices U and L such that

$$\bar{S}=USL=\begin{bmatrix}I_r & 0\\ 0 & 0\end{bmatrix},\ \bar{B}=UBL=\begin{bmatrix}\bar{B}_1 & \bar{B}_2\\ \bar{B}_3 & \bar{B}_4\end{bmatrix},\ \bar{W}_5=U^{-T}W_5U^{-1}=\begin{bmatrix}\bar{W}_{51} & \bar{W}_{52}\\ \bar{W}_{53} & \bar{W}_{54}\end{bmatrix}.$$

Pre- and post- multiplying (6) by L^T and L respectively, then we obtain

$$\bar{\nabla}=L^T\nabla L=-\bar{W}_5\bar{B}-\bar{B}\bar{W}_5=\begin{bmatrix}\bar{\nabla}_1 & \bar{\nabla}_2\\ \bar{\nabla}_3 & \bar{\nabla}_4\end{bmatrix}<0,$$

here, $\bar{\nabla}_4=-\bar{W}_{54}\bar{B}_4-\bar{B}_4\bar{W}_{54}$. Because of $\bar{\nabla}_1,\bar{\nabla}_2$ and $\bar{\nabla}_3$ are unrelated to the discussion in proof. , their real expressions are omitted here. From here, we obtain $-\bar{W}_{54}\bar{B}_4-\bar{B}_4\bar{W}_{54}<0.$ Therefore, $\bar{B}_4$ is regular. From this reason, the pair (S,B) is regular and impulse free (see [21]). According to Dai [7] and Q. Wu et al., [19] the system (1) is regular and impulse free.

Secondly, we prove that the system (1) is stable. For symmetric matrices $K_k=K_k^{\mathrm{T}}>0,(k=1,...,7),$ $W_i=\mathrm{W_i^T}>0,(i=1,4,5)$ and any suitable dimensions matrices W_i $(i=2,3).$ Let us define a new positive definite functional as:

$$V(t)={}_{to}D_t^{q-1}(\Omega^{\mathrm{T}}(t)K_1\Omega(t))+\int_{t-\tau}^{t}x^{\mathrm{T}}(s)K_2x(s)ds+\int_{t-\sigma}^{t}x^{\mathrm{T}}(s)K_3x(s)ds$$
$$+\int_{t-\tau}^{t}(\tau-t+s)x^{\mathrm{T}}(s)K_4x(s)ds+\int_{t-\sigma(t)}^{t}x^{\mathrm{T}}(s)K_5x(s)ds$$
$$+\int_{t-\sigma(t)}^{t}G^{\mathrm{T}}(x(s))K_6G(x(s))ds+\sigma\int_{-\sigma t+\beta}^{0}\int_{t}^{t}x^{\mathrm{T}}(\xi)K_7x(\xi)d\xi d\eta. \quad (7)$$

In view of the fact that Lemma 2.1, Lemma 2.2 and Jhensen inequality Lemma (see [18]), by the time-derivative of $V(t)$ on the solution of system (1), we can get the following inequality as:

$$\dot{V}(t,x)\le 2\Omega^{\mathrm{T}}(t)K_1({}_{to}D_t^q\Omega(t))+x^{\mathrm{T}}(t)K_2x(t)-x^{\mathrm{T}}(t-\tau)K_2x(t-\tau)$$

$$
\begin{aligned}
&+x^{\mathrm{T}}(t)K_3x(t)-x^{\mathrm{T}}(t-\sigma)K_3x(t-\sigma)+\varpi x^{\mathrm{T}}(t)K_4x(t)\\
&+x^{\mathrm{T}}(t)K_5x(t)-(1-\dot{\sigma}(t))x^{\mathrm{T}}(t-\sigma(t))K_5x(t-\sigma(t))\\
&+G^{\mathrm{T}}(x(t))K_6G(x(t))-(1-\dot{\sigma}(t))G^{\mathrm{T}}(x(t-\sigma(t)))K_6G(x(t-\sigma(t)))\\
&+\sigma^2x(t)K_7x(t)-\sigma\int_{t-\sigma}^{t}x^{\mathrm{T}}(s)K_7x(s)ds\\
&\le 2\Omega^{\mathrm{T}}(t)K_1[-Bx(t)+Rx(t-\sigma)+E\int_{t-\sigma}^{t}x(s)ds+Tx(t-\sigma(t))+G(x(t-\sigma(t)))]\\
&+2\Omega^{\mathrm{T}}(t)W_1[-\Omega(t)+Sx(t)+Ax(t-\tau)]+x^{\mathrm{T}}(t)K_2x(t)\\
&+2x^{\mathrm{T}}(t)W_2[-\Omega(t)+Sx(t)+Ax(t-\tau)]-x^{\mathrm{T}}(t-\tau)K_2x(t-\tau)\\
&+2x^{\mathrm{T}}(t-\tau)W_3[-\Omega(t)+Sx(t)+Ax(t-\tau)]+x^{\mathrm{T}}(t)K_3x(t)\\
&-x^{\mathrm{T}}(t-\sigma)K_3x(t-\sigma)+\varpi x^{\mathrm{T}}(t)K_4x(t)+x^{\mathrm{T}}(t)K_5x(t)\\
&-(1-\mu)x^{\mathrm{T}}(t-\sigma(t))K_5x(t-\sigma(t))+a^2x^{\mathrm{T}}(t)K_6x(t)\\
&-(1-\mu)G^{\mathrm{T}}(x(t-\sigma(t)))K_6G(x(t-\sigma(t)))+\sigma^2x(t)K_7x(t)\\
&-\left(\int_{t-\sigma}^{t}x(s)ds\right)^{\mathrm{T}}K_7\left(\int_{t-\sigma}^{t}x(s)ds\right).
\end{aligned}
\tag{8}
$$

We noting that

$$
0=-{}_{t_0}D_t^{g}\Omega(t)-Bx(t)+Rx(t-\sigma)+E\int_{t-\sigma}^{t}x(s)ds+Tx(t-\sigma(t))+G(x(t-\sigma(t))).
$$

From here, we can obtain

$$
\begin{aligned}
0=&2_{t_0}D_t^{g}\Omega^{\mathrm{T}}(t)BW_4(-{}_{t_0}D_t^{g}\Omega(t)-Bx(t)+Rx(t-\sigma)+E\int_{t-\sigma}^{t}x(s)ds+Tx(t-\sigma(t))+G(x(t-\sigma(t))))\\
&+2x^{\mathrm{T}}(t)W_5(-{}_{t_0}D_t^{g}\Omega(t)-Bx(t)+Rx(t-\sigma)+E\int_{t-\sigma}^{t}x(s)ds+Tx(t-\sigma(t))+G(x(t-\sigma(t)))).
\end{aligned}
\tag{9}
$$

Additionally, from the nonlinear parameter $G(.)$ condition given with (3), we get

$$
0\le \varepsilon b^2x^{\mathrm{T}}(t-\sigma(t))x(t-\sigma(t))-\varepsilon G^{\mathrm{T}}(x(t-\sigma(t)))G(x(t-\sigma(t))).
\tag{10}
$$

where $\varepsilon>0.$

Combining (8)-(10), we can have the below inequality as:

$$
\dot{V}(t,x)\le \chi^{\mathrm{T}}(t)\Theta\chi(t),
$$

here the matrix Θ is defined with (5) and

$$
\chi^{\mathrm{T}}(t)=[\Omega^{\mathrm{T}}(t)\quad x^{\mathrm{T}}(t)\quad x^{\mathrm{T}}(t-\tau)\quad x^{\mathrm{T}}(t-\sigma)\quad x^{\mathrm{T}}(t-\sigma(t))\quad G^{\mathrm{T}}(x(t-\sigma(t)))\quad \int_{t-\sigma}^{t}x(s)ds\quad ({}_{t_0}D_t^{g}\Omega(t))^{\mathrm{T}}].
$$

Because of matrix inequality (5) and impulse free and regularity criteria are satisfied and $\chi^{\mathrm{T}}(t)\neq 0,$ then the neutral fractional singular system (1) is admissible. □

Further, we define the following fractional neutral singular system (1) with $E\int_{t-\sigma}^{t}x(s)ds=0,$

$$
\begin{aligned}
&{}_{t_0}D_t^{g}[Sx(t)+Ax(t-\tau)]=-Bx(t)+Rx(t-\sigma)+Tx(t-\sigma(t))+G(x(t-\sigma(t))),\\
&x(t)=\vartheta(t),t\in[-\kappa,0],\kappa>0,\kappa\in\Re,
\end{aligned}
\tag{11}
$$

for $q\in(0,1]$, the system state $x(t)\in\Re^n$, $A,B,R,T\in\Re^{n\times n}$ are symmetric positive definite system matrices, the matrix $S\in\Re^{n\times n}$ is singular and satisfied $rankS=r\le n, n\ge 1,$ with $\|A\|<1,$ the time variable delay $\sigma(t)$ is assumed to satisfy $0\le\sigma(t)\le\sigma$ and $\dot{\sigma}(t)\le\mu,$ the constant delays τ,σ are real positive numbers and $\vartheta\in C([-\kappa,0];\Re^n)$ with $\kappa=\max\{\tau,\sigma\}$ and the nonlinear perturbation parameter $G(.)$ satisfying

$$
G^{\mathrm{T}}(x(t))G(x(t))\le a^2x^{\mathrm{T}}(t)x(t),
$$

$$
G^{\mathrm{T}}(x(t-\sigma(t)))G(x(t-\sigma(t)))\le b^2x^{\mathrm{T}}(t-\sigma(t))x(t-\sigma(t)),
$$

where a,b are given any numbers.

Corollary 3.1. We suppose that the following hypothesis is met:

(H2) Let a,b be any numbers and $\tau>0,\sigma>0,$ if there are symmetric matrices $K_k=K_k{}^{\mathrm{T}}>0,(k=1,...,6),$ $W_i=\mathrm{W_i^T}>0,(i=1,4,5)$ and any suitable dimensions matrices W_i $(i=2,3)$ such that the following relationship is satisfied:

$$
\begin{bmatrix}
\Lambda_{11} & \Lambda_{12} & \Lambda_{13} & K_1R & K_1T & K_1 & 0\\
* & \Lambda_{22} & \Lambda_{23} & W_5R & W_5T & W_5 & \Lambda_{27}\\
* & * & \Lambda_{33} & 0 & 0 & 0 & 0\\
* & * & * & -K_3 & 0 & 0 & RW_4^{\mathrm{T}}R\\
* & * & * & * & \Lambda_{55} & 0 & TW_4^{\mathrm{T}}R\\
* & * & * & * & * & \Lambda_{66} & W_4^{\mathrm{T}}R\\
* & * & * & * & * & * & \Lambda_{77}
\end{bmatrix}<0,
\tag{12}
$$

where

$\Lambda_{11} = -W_1 - W_1^{\mathrm{T}}$, $\Lambda_{12} = -K_1 B + W_1 S - W_2^{\mathrm{T}}$, $\Lambda_{13} = W_1 A - W_3^{\mathrm{T}}$,
$\Lambda_{22} = W_2 S + S^{\mathrm{T}} W_2^{\mathrm{T}} - W_5 B - B W_5^{\mathrm{T}} + K_2 + K_3 + \tau K_4 + K_5 + a^2 K$
$\Lambda_{23} = W_2 A + S^{\mathrm{T}} W_3^{\mathrm{T}}$, $\Lambda_{27} = -B W_4^{\mathrm{T}} R - W_5$,
$\Lambda_{33} = W_3 A + A^{\mathrm{T}} W_3^{\mathrm{T}} - K_2$,
$\Lambda_{55} = -(1-\mu) K_5 + \varepsilon b^2 \mathrm{I}$,
$\Lambda_{66} = -(1-\mu) K_6 - \varepsilon \mathrm{I}$,
$\Lambda_{77} = -R W_4 - W_4^{\mathrm{T}} R$.

where ε is a positive number and I is identity matrix with appropriate dimension.

Then the zero solution of system (11) is admissible.

Proof. For symmetric matrices $K_k = K_k^{\mathrm{T}} > 0, (k = 1,...,6)$, $W_i = \mathrm{W_i^T} > 0, (i = 1,4,5)$ and any suitable dimensions matrices W_i $(i = 2,3)$. Let us define a new positive definite functional as:

$$V(t) = {}_{to}D_t^{q-1}(\Omega^{\mathrm{T}}(t) K_1 \Omega(t)) + \int_{t-\tau}^{t} x^{\mathrm{T}}(s) K_2 x(s) ds + \int_{t-\sigma}^{t} x^{\mathrm{T}}(s) K_3 x(s) ds + \int_{t-\tau}^{t} (\tau - t + s) x^{\mathrm{T}}(s) K_4 x(s) ds + \int_{t-\sigma(t)}^{t} x^{\mathrm{T}}(s) K_5 x(s) ds + \int_{t-\sigma(t)}^{t} G^{\mathrm{T}}(x(s)) K_6 G(x(s)) ds.$$

In view of Theorem 3.1, we show that the admissibility condition (12) of system given with (11). □

Additionally, we define the following fractional neutral singular system (1) with $E\int_{t-\sigma}^{t} x(s) ds = 0$ and $G(x(t-\sigma(t))) = 0$,

$$ {}_{to}D_t^{q}[Sx(t) + Ax(t-\tau)] = -Bx(t) + Rx(t-\sigma) + Tx(t-\sigma(t)), \quad (13)$$
$$x(t) = \vartheta(t), t \in [-\kappa, 0], \kappa > 0, \kappa \in \Re,$$

for $q \in (0,1]$, the system state $x(t) \in \Re^n$, $A, B, R, T \in \Re^{n \times n}$ are symmetric positive definite system matrices, the matrix $S \in \Re^{n \times n}$ is singular and satisfied $rankS = r \le n, n \ge 1$, with $\| A \| < 1$, the time variable delay $\sigma(t)$ is assumed to satisfy $0 \le \sigma(t) \le \sigma$ and $\dot{\sigma}(t) \le \mu$, the constant delays τ, σ are real positive numbers and $\vartheta \in C([-\kappa, 0]; \Re^n)$ with $\kappa = \max\{\tau, \sigma\}$.

Corollary 3.2. We suppose that the following hypothesis is met:

(H3) Let $\tau > 0, \sigma > 0$ be numbers, if there are symmetric matrices $K_k = K_k^{\mathrm{T}} > 0, (k = 1,...,5)$, $W_i = \mathrm{W_i^T} > 0, (i = 1,4,5)$ and any suitable matrices W_i $(i = 2,3)$ such that the following relationship is satisfied:

$$\begin{bmatrix} \Psi_{11} & \Psi_{12} & \Psi_{13} & K_1 R & K_1 T & 0 \\ * & \Psi_{22} & \Psi_{23} & W_5 R & W_5 T & \Psi_{26} \\ * & * & \Psi_{33} & 0 & 0 & 0 \\ * & * & * & -K_3 & 0 & R W_4 R \\ * & * & * & * & \Psi_{55} & T W_4 R \\ * & * & * & * & * & \Psi_{66} \end{bmatrix} < 0, \quad (14)$$

Where

$\Psi_{11} = -W_1 - W_1^{\mathrm{T}}$, $\Psi_{12} = -K_1 B + W_1 S - W_2^{\mathrm{T}}$, $\Psi_{13} = W_1 A - W_3^{\mathrm{T}}$,
$\Psi_{22} = W_2 S + S^{\mathrm{T}} W_2^{\mathrm{T}} - W_5 B - B W_5^{\mathrm{T}} + K_2 + K_3 + \tau K_4 + K_5$,
$\Psi_{23} = W_2 A + S^{\mathrm{T}} W_3^{\mathrm{T}}$, $\Psi_{26} = -B W_4^{\mathrm{T}} R - W_5$,
$\Psi_{33} = W_3 A + A^{\mathrm{T}} W_3^{\mathrm{T}} - K_2$,
$\Psi_{55} = -(1-\mu) K_5$, $\Psi_{66} = -R W_4 - W_4^{\mathrm{T}} R$.

Then, the zero solution of system (13) is admissible.

Proof. For symmetric matrices $K_k = K_k^{\mathrm{T}} > 0, (k = 1,...,5)$, $W_i = \mathrm{W_i^T} > 0, (i = 1,4,5)$, and any suitable dimensions matrices W_i $(i = 2,3)$. Let us define a new positive definite functional as:

$$V(t) = {}_{to}D_t^{q-1}(\Omega^{\mathrm{T}}(t) K_1 \Omega(t)) + \int_{t-\tau}^{t} x^{\mathrm{T}}(s) K_2 x(s) ds + \int_{t-\sigma}^{t} x^{\mathrm{T}}(s) K_3 x(s) ds + \int_{t-\tau}^{t} (\tau - t + s) x^{\mathrm{T}}(s) K_4 x(s) ds + \int_{t-\sigma(t)}^{t} x^{\mathrm{T}}(s) K_5 x(s) ds.$$

In view of Theorem 3.1, we show that the admissibility condition (14) of system given with (13). □

Next, we define the following fractional neutral singular system (1) with $E\int_{t-\sigma}^{t} x(s)ds = 0,\ Tx(t-\sigma(t)) = 0$ and $G(x(t-\sigma(t))) = 0,$

$$ {}_{to}D_t^q[Sx(t) + Ax(t-\tau)] = -Bx(t) + Rx(t-\sigma), \qquad (15)$$
$$ x(t) = \vartheta(t), t \in [-\kappa, 0], \kappa > 0, \kappa \in \Re, $$

for $q \in (0,1]$, the system state $x(t) \in \Re^n$, $A, B, R \in \Re^{n\times n}$ are symmetric positive definite system matrices, the matrix $S \in \Re^{n\times n}$ is singular and satisfied $rankS = r \le n, n \ge 1,$ with $\| A \| < 1,$ the constant delays τ, σ are real positive numbers and $\vartheta \in C([-\kappa, 0]; \Re^n)$ with $\kappa = \max\{\tau, \sigma\}.$

Corollary 3.3. We suppose that the following hypothesis is met:

(H4) Let $\tau > 0, \sigma > 0$ be numbers, if there are symmetric matrices $K_k = K_k^{\mathrm{T}} > 0, (k = 1,...,4),$ $W_i = \mathrm{W}_i^{\mathrm{T}} > 0, (i = 1,4,5),$ and any suitable dimensions matrices W_i $(i = 2,3)$ such that the following relationship is satisfied:

$$\begin{bmatrix} \Delta_{11} & \Delta_{12} & \Delta_{13} & K_1R & 0 \\ * & \Delta_{22} & \Delta_{23} & W_5R & \Delta_{25} \\ * & * & \Delta_{33} & 0 & 0 \\ * & * & * & -K_3 & BW_4^{\mathrm{T}}R \\ * & * & * & * & \Delta_{55} \end{bmatrix} < 0, \qquad (16)$$

where

$$\Delta_{11} = -W_1 - W_1^{\mathrm{T}},\ \Delta_{12} = -K_1B + W_1S - W_2^{\mathrm{T}},\ \Delta_{13} = W_1A - W_3^{\mathrm{T}},$$
$$\Delta_{22} = W_2S + S^{\mathrm{T}}W_2^{\mathrm{T}} - W_5B - BW_5^{\mathrm{T}} + K_2 + K_3 + \tau K_4,$$
$$\Delta_{23} = W_2A + S^{\mathrm{T}}W_3^{\mathrm{T}},\ \Delta_{25} = -BW_4^{\mathrm{T}}R - W_5,$$
$$\Delta_{33} = W_3A + A^{\mathrm{T}}W_3^{\mathrm{T}} - K_2,\ \Delta_{55} = -RW_4 - W_4^{\mathrm{T}}R.$$

Then the system (15) is admissible.

Proof. For symmetric matrices $K_k = K_k^{\mathrm{T}} > 0, (k = 1,...,4),$ $W_i = \mathrm{W}_i^{\mathrm{T}} > 0, (i = 1,4,5),$ and any suitable dimensions matrices W_i $(i = 2,3).$ Let us define a new positive definite functional as:

$$V(t) = {}_{to}D_t^{q-1}(\Omega^{\mathrm{T}}(t)K_1\Omega(t)) + \int_{t-\tau}^{t} x^{\mathrm{T}}(s)K_2x(s)ds + \int_{t-\sigma}^{t} x^{\mathrm{T}}(s)K_3x(s)ds + \int_{t-\tau}^{t} (\tau - t + s)x^{\mathrm{T}}(s)K_4x(s)ds.$$

In view of Theorem 3.1, we show that the admissibility condition (16) of system given with (15). □

Next, we define the following fractional neutral singular system (1) with $E\int_{t-\sigma}^{t} x(s)ds = 0,\quad Tx(t-\sigma(t)) = 0,$ $G(x(t-\sigma(t))) = 0$ and $\sigma = \tau,$

$$ {}_{to}D_t^q[Sx(t) + Ax(t-\tau)] = -Bx(t) + Rx(t-\tau), \qquad (17)$$
$$ x(t) = \vartheta(t), t \in [-\kappa, 0], \kappa > 0, \kappa \in \Re, $$

for $q \in (0,1]$, the system state $x(t) \in \Re^n$, $A, B, R \in \Re^{n\times n}$ are symmetric positive definite system matrices, the matrix $S \in \Re^{n\times n}$ is singular and satisfied $rankS = r \le n, n \ge 1,$ with $\| A \| < 1,$ the constant delay τ is real positive number and $\vartheta \in C([-\kappa, 0]; \Re^n).$

Corollary 3.4. We suppose that the following hypothesis is met:

(H5) Let $\tau > 0$ be number, if there are symmetric matrices $K_k = K_k^{\mathrm{T}} > 0, (k = 1,2,3),$ $W_i = \mathrm{W}_i^{\mathrm{T}} > 0, (i = 1,4,5)$ and any suitable dimensions matrices W_i $(i = 2,3)$ such that the following relationship is satisfied:

$$\begin{bmatrix} \Pi_{11} & \Pi_{12} & \Pi_{13} & 0 \\ * & \Pi_{22} & \Pi_{23} & \Pi_{24} \\ * & * & \Pi_{33} & 0 \\ * & * & * & \Pi_{44} \end{bmatrix} < 0, \qquad (18)$$

where

$$\Pi_{11} = -W_1 - W_1^T,\ \Pi_{12} = -K_1B + W_1S - W_2^T,\ \Pi_{13} = W_1A - W_3^T + K_1R,$$
$$\Pi_{22} = W_2S + S^TW_2^T - W_5B - BW_5^T + K_2 + \tau K_3,$$
$$\Pi_{23} = W_2A + S^TW_3^T,\ \Pi_{24} = -BW_4^TR - W_5,$$
$$\Pi_{33} = W_3A + A^TW_3^T - K_2,\ \Pi_{44} = -RW_4 - W_4^TR.$$

Then the system (17) is admissible.

Proof. For symmetric matrices $K_k = K_k^T > 0, (k = 1,2,3)$, $W_i = W_i^T > 0, (i = 1,4,5)$ and any suitable dimensions matrices W_i $(i = 2,3)$. Let us define a new positive definite functional as:

$$V(t) = {}_{t_0}D_t^{q-1}(\Omega^T(t)K_1\Omega(t)) + \int_{t-\tau}^{t} x^T(s)K_2x(s)ds + \int_{t-\tau}^{t}(\tau - t + s)x^T(s)K_3x(s)ds.$$

In view of Theorem 3.1, we show that the admissibility condition (18) of system given with (17). □

Remark 3.1. As mentioned in the first section, which is introduction; this study was mainly inspired by some studies cited references. However, since the systems discussed in this study are singular, it is a new study different from some of the studies cited in the references (see [4,11,18,22]) mentioned in the references, and it is clear that it is more difficult to achieve the goal. To overcome this difficulty, we benefited suitable Lyapunov-Krasovskii functionals and zero equations. Moreover, the Lyapunov-Krasovskii functionals used in the Study are new and obviously more comprehensive than their counterparts used in the literature (see [4,6,11,18,19,22]).

4. Numerical applications

In this section, we bring to the attention of the readers some examples, with their annotated solutions and graphics, showing that the theoretically sufficient conditions obtained in the previous section are applicable in practice. When the solutions of these examples are examined, it is clearly seen that the zero solutions of the systems in question are stable after a certain time interval. In addition, each example is support with the corresponding simulation result obtained with the help of MATLAB-Simulink.

Example 4.1. We define a fractional nonlinear neutral singular system as:

$${}_{t_0}D_t^q[Sx(t) + Ax(t-\tau)] = -Bx(t) + Rx(t-\sigma) + E\int_{t-\sigma}^{t} x(s)ds + Tx(t-\sigma(t)) + G(x(t-\sigma(t)), \quad (19)$$

for

$$q \in (0,1], x(t) = [x_1(t) \quad x_2(t)]^T,$$
$$G(x(t-\sigma(t))) = [\sin(x_1(t-\sigma(t)) \quad 1-\cos(x_2(t-\sigma(t)))]^T.$$

Solving the inequality (5), with the help of MATLAB software, when

$$S = \begin{bmatrix} 1 & 0 \\ 0 & 0 \end{bmatrix}, B = \begin{bmatrix} 25 & 0 \\ 0 & 26 \end{bmatrix}, R = \begin{bmatrix} 0.43 & 0 \\ 0 & 0.1225 \end{bmatrix},$$
$$A = \begin{bmatrix} 0.28 & 0 \\ 0 & 0.1725 \end{bmatrix}, E = \begin{bmatrix} 0.015 & 0 \\ 0 & 0.02 \end{bmatrix}, T = \begin{bmatrix} 0.02 & 0 \\ 0 & 0.01 \end{bmatrix},$$

we have a set of parameters that provides admissibility of the system (19) that

$$a = 0.002,$$
$$b = 0.005,$$
$$\tau = 0.2,$$
$$0 \le \sigma(t) = 0.25 + 0.25\sin t \le 0.5 = \sigma,$$
$$\dot{\sigma}(t) = 0.25\cos t \le 0.25 = \mu < 1,$$
$$\varepsilon = 1$$

as follows:

$$W_1 = \begin{bmatrix} 6{,}95 & 0 \\ 0 & 17.5 \end{bmatrix}, W_2 = \begin{bmatrix} -7.98 & 0 \\ 0 & -0.02 \end{bmatrix}, W_3 = \begin{bmatrix} -2 & 0 \\ 0 & -3 \end{bmatrix},$$
$$W_4 = \begin{bmatrix} 0.02 & 0 \\ 0 & 0.2802 \end{bmatrix}, W_5 = \begin{bmatrix} 0.1028 & 0 \\ 0 & 0.878 \end{bmatrix}, K_1 = \begin{bmatrix} 0.1 & 0 \\ 0 & 0.00035 \end{bmatrix},$$
$$K_2 = \begin{bmatrix} 0.15 & 0 \\ 0 & 0.00012 \end{bmatrix}, K_3 = \begin{bmatrix} 0.0065 & 0 \\ 0 & 0.0008 \end{bmatrix}, K_4 = \begin{bmatrix} 0.0005 & 0 \\ 0 & 0.0001 \end{bmatrix},$$
$$K_5 = \begin{bmatrix} 0.01 & 0 \\ 0 & 0.00012 \end{bmatrix}, K_6 = \begin{bmatrix} 0.03 & 0 \\ 0 & 8 \end{bmatrix}, K_7 = \begin{bmatrix} 0.01 & 0 \\ 0 & 0.001 \end{bmatrix}.$$

It is clear that all conditions of admissibility criteria for system (19) are satisfied. Therefore, the system (19) is admissible. Also, the graph showing the orbital behavior of the system (19) is as follows.

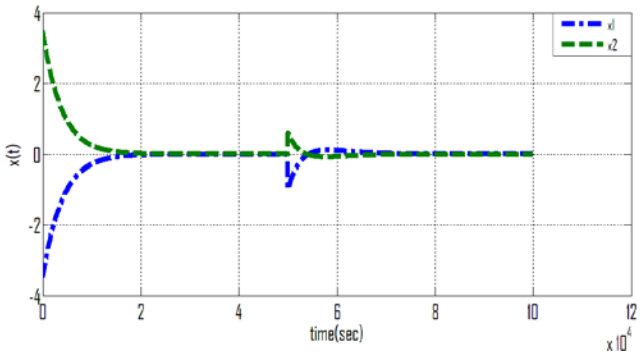

Figure 1. *Orbital behavior of the system (19).*

Example 4.2. We define a fractional nonlinear neutral singular system as:

$$ {}_{t_0}D_t^q[Sx(t)+Ax(t-\tau)] = -Bx(t)+Rx(t-\sigma)+Tx(t-\sigma(t))+G(x(t-\sigma(t))), \quad (20)$$

for $q \in (0,1]$, $x(t) = [x_1(t) \quad x_2(t) \quad x_3(t)]^T$,

$$G(x(t-\sigma(t))) = [\sin(x_1(t-\sigma(t))) \quad \sin(x_1(t-\sigma(t))) + x_2(t-\sigma(t))) \quad \sin(x_2(t-\sigma(t)))]^T.$$

Solving the inequality (12), with the help of MATLAB software, when

$$S = \begin{bmatrix} 1 & 0 & 0 \\ 0 & 1 & 0 \\ 0 & 0 & 0 \end{bmatrix}, B = \begin{bmatrix} 25 & 0 & 0 \\ 0 & 15 & 0 \\ 0 & 0 & 26 \end{bmatrix}, R = \begin{bmatrix} 0.43 & 0 & 0 \\ 0 & 0.44 & 0 \\ 0 & 0 & 0.1225 \end{bmatrix},$$

$$A = \begin{bmatrix} 0.28 & 0 & 0 \\ 0 & 0.25 & 0 \\ 0 & 0 & 0.1725 \end{bmatrix}, T = \begin{bmatrix} 0.02 & 0 & 0 \\ 0 & 0.03 & 0 \\ 0 & 0 & 0.01 \end{bmatrix},$$

we have a set of parameters that provides admissibility of the system (20) that $a = 0.002$, $b = 0.005$, $\tau = 0.2$, $0 \le \sigma(t) = 0.25 + 0.25\sin t \le 0.5 = \sigma$, $\dot{\sigma}(t) = 0.25\cos t \le 0.25 = \mu < 1$, $\varepsilon = 1$ as follows:

$$W_1 = \begin{bmatrix} 6.95 & 0 & 0 \\ 0 & 6.98 & 0 \\ 0 & 0 & 17.5 \end{bmatrix}, W_2 = \begin{bmatrix} -7.98 & 0 & 0 \\ 0 & -8 & 0 \\ 0 & 0 & -0.02 \end{bmatrix}, W_3 = \begin{bmatrix} -2 & 0 & 0 \\ 0 & -0.095 & 0 \\ 0 & 0 & -3 \end{bmatrix},$$

$$W_4 = \begin{bmatrix} 0.02 & 0 & 0 \\ 0 & 0.03 & 0 \\ 0 & 0 & 0.2802 \end{bmatrix}, W_5 = \begin{bmatrix} 0.1028 & 0 & 0 \\ 0 & 0.15 & 0 \\ 0 & 0 & 0.878 \end{bmatrix}, K_1 = \begin{bmatrix} 0.1 & 0 & 0 \\ 0 & 0.14 & 0 \\ 0 & 0 & 0.00035 \end{bmatrix},$$

$$K_2 = \begin{bmatrix} 0.15 & 0 & 0 \\ 0 & 0.36 & 0 \\ 0 & 0 & 0.00012 \end{bmatrix}, K_3 = \begin{bmatrix} 0.0065 & 0 & 0 \\ 0 & 0.0063 & 0 \\ 0 & 0 & 0.0008 \end{bmatrix}, K_4 = \begin{bmatrix} 0.0005 & 0 & 0 \\ 0 & 0.0008 & 0 \\ 0 & 0 & 0.0001 \end{bmatrix},$$

$$K_5 = \begin{bmatrix} 0.01 & 0 & 0 \\ 0 & 0.015 & 0 \\ 0 & 0 & 0.00012 \end{bmatrix}, K_6 = \begin{bmatrix} 0.03 & 0 & 0 \\ 0 & 0.05 & 0 \\ 0 & 0 & 8 \end{bmatrix}.$$

It is clear that all conditions of admissibility criteria for system (20) are satisfied. Therefore, the system (20) is admissible. Also, the graph showing the orbital behavior of the system (20) is as follows.

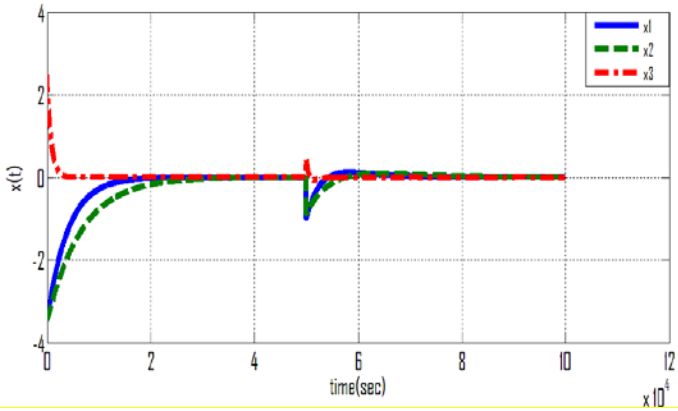

Figure 2. *Orbital behavior of the system (20).*

Example 4.3. We define a fractional neutral singular system as:

$$ {}_{t_0}D_t^q[Sx(t)+Ax(t-\tau)] = -Bx(t)+Rx(t-\sigma)+Tx(t-\sigma(t)), \quad (21)$$

for $q \in (0,1]$, $x(t) = [x_1(t) \quad x_2(t) \quad x_3(t) \quad x_4(t)]^T$,

Solving the inequality (14), with the help of MATLAB software, when

$$S = \begin{bmatrix} 1 & 0 & 0 & 0 \\ 0 & 1 & 0 & 0 \\ 0 & 0 & 1 & 0 \\ 0 & 0 & 0 & 0 \end{bmatrix}, B = \begin{bmatrix} 25 & 0 & 0 & 0 \\ 0 & 15 & 0 & 0 \\ 0 & 0 & 8 & 0 \\ 0 & 0 & 0 & 26 \end{bmatrix}, R = \begin{bmatrix} 0.43 & 0 & 0 & 0 \\ 0 & 0.44 & 0 & 0 \\ 0 & 0 & 0.45 & 0 \\ 0 & 0 & 0 & 0.1225 \end{bmatrix},$$

$$A = \begin{bmatrix} 0.28 & 0 & 0 & 0 \\ 0 & 0.25 & 0 & 0 \\ 0 & 0 & 0.02 & 0 \\ 0 & 0 & 0 & 0.1725 \end{bmatrix}, T = \begin{bmatrix} 0.02 & 0 & 0 & 0 \\ 0 & 0.03 & 0 & 0 \\ 0 & 0 & 0.025 & 0 \\ 0 & 0 & 0 & 0.01 \end{bmatrix},$$

we have a set of parameters that provides admissibility of the system (21) that

$\tau = 0.2,\ 0 \le \sigma(t) = 0.25 + 0.25\sin t \le 0.5 = \sigma,\ \dot{\sigma}(t) = 0.25\cos t \le 0.25 = \mu < 1$

as follows:

$$W_1 = \begin{bmatrix} 6.95 & 0 & 0 & 0 \\ 0 & 6.98 & 0 & 0 \\ 0 & 0 & 7 & 0 \\ 0 & 0 & 0 & 17.5 \end{bmatrix}, W_2 = \begin{bmatrix} -7.98 & 0 & 0 & 0 \\ 0 & -8 & 0 & 0 \\ 0 & 0 & -7.8 & 0 \\ 0 & 0 & 0 & -0.02 \end{bmatrix}, W_3 = \begin{bmatrix} -2 & 0 & 0 & 0 \\ 0 & -0.095 & 0 & 0 \\ 0 & 0 & 0.85 & 0 \\ 0 & 0 & 0 & -3 \end{bmatrix}$$

$$W_4 = \begin{bmatrix} 0.02 & 0 & 0 & 0 \\ 0 & 0.03 & 0 & 0 \\ 0 & 0 & 0.025 & 0 \\ 0 & 0 & 0 & 0.2802 \end{bmatrix}, W_5 = \begin{bmatrix} 0.1028 & 0 & 0 & 0 \\ 0 & 0.15 & 0 & 0 \\ 0 & 0 & 0.14 & 0 \\ 0 & 0 & 0 & 0.878 \end{bmatrix}, K_1 = \begin{bmatrix} 0.1 & 0 & 0 & 0 \\ 0 & 0.14 & 0 & 0 \\ 0 & 0 & 0.18 & 0 \\ 0 & 0 & 0 & 0.00035 \end{bmatrix},$$

$$K_2 = \begin{bmatrix} 0.15 & 0 & 0 & 0 \\ 0 & 0.36 & 0 & 0 \\ 0 & 0 & 0.28 & 0 \\ 0 & 0 & 0 & 0.00012 \end{bmatrix}, K_3 = \begin{bmatrix} 0.0065 & 0 & 0 & 0 \\ 0 & 0.0063 & 0 & 0 \\ 0 & 0 & 0.006 & 0 \\ 0 & 0 & 0 & 0.0008 \end{bmatrix},$$

$$K_4 = \begin{bmatrix} 0.0005 & 0 & 0 & 0 \\ 0 & 0.0008 & 0 & 0 \\ 0 & 0 & 0.0006 & 0 \\ 0 & 0 & 0 & 0.0001 \end{bmatrix}, K_5 = \begin{bmatrix} 0.01 & 0 & 0 & 0 \\ 0 & 0.015 & 0 & 0 \\ 0 & 0 & 0.025 & 0 \\ 0 & 0 & 0 & 0.00012 \end{bmatrix}.$$

It is clear that all conditions of admissibility criteria for system (21) are satisfied. Therefore, the system (21) is admissible. Also, the graph showing the orbital behavior of the system (21) is as follows.

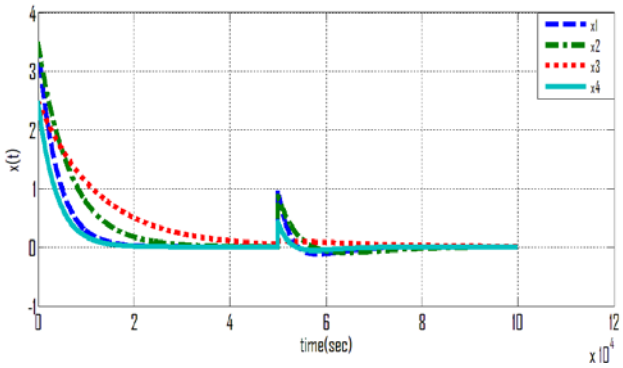

Figure 3. *Orbital behavior of the system (21).*

Example 4.4. We define a fractional neutral singular system as:

$$_{to}D_t^q[Sx(t) + Ax(t-\tau)] = -Bx(t) + Rx(t-\sigma), \qquad (22)$$

for

$$q \in (0,1],\ x(t) = \begin{bmatrix} x_1(t) & x_2(t) & x_3(t) & x_4(t) & x_5(t) \end{bmatrix}^T,$$

Solving the inequality (16), with the help of MATLAB software, when $S = diag(1,1,1,1,0)$,

$$B = diag(25,15,8,10,26),\ R = diag(0.43,0.44,0.45,,0.48,0.1225),$$
$$A = diag(0.28,0.25,0.02,0.03,0.1725),$$

we have a set of parameters that provides admissibility of the system (22) that $\tau = 0.2,\ \sigma = 0.5$ as follows:

$$W_1 = diag(6.95,6.98,7,6.5,17.5),$$
$$W_2 = diag(-7.98,-8,-7.8,-8.02,-0.02),$$
$$W_3 = diag(-2,-0.095,0.85,0.5,-3),$$

$$W_4 = diag(0.02,0.03,0.025,0.028,0.2802),$$
$$W_5 = diag(0.1028,0.15,0.14,0.2,0.878),$$

$$K_1 = diag(0.1,0.14,0.18,0.23,0.00035),$$
$$K_2 = diag(0.15,0.36,0.28,0.18,0.00012),$$

$$K_3 = diag(0.0065,0.0063,0.006,0.008,0.0008),$$
$$K_4 = diag(0.0005,0.0008,0.0006,0.0012,0.0001).$$

It is clear that all conditions of admissibility criteria for system (22) are satisfied. Therefore, the system (22) is admissible. Also, the graph showing the orbital behavior of the system (22) is as follows.

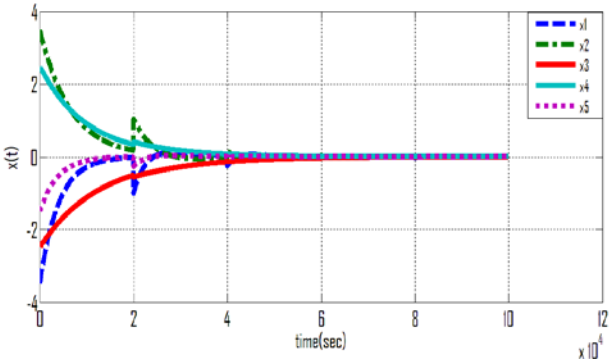

Figure 4. *Orbital behavior of the system (22).*

Example 4.5. We define a fractional neutral singular system as:

$$ {}_{to}D_t^q[Sx(t)+Ax(t-\tau)] = -Bx(t)+Rx(t-\tau), \quad (23)$$

for

$$q \in (0,1], x(t) = \begin{bmatrix} x_1(t) & x_2(t) & x_3(t) & x_4(t) & x_5(t) & x_6(t) \end{bmatrix}^T,$$

Solving the inequality (18), with the help of MATLAB software, when $S = diag(1,1,1,1,1,0)$,

$$B = diag(25,15,8,10,12,26),$$
$$R = diag(0.43,0.44,0.45,,0.48,0.5,0.1225),$$
$$A = diag(0.28,0.25,0.02,0.03,0.04,0.1725),$$

we have a set of parameters that provides admissibility of the system (23) that $\tau = 0.2$ as follows:

$$W_1 = diag(6.95,6.98,7,6.5,6.8,17.5),$$
$$W_2 = diag(-7.98,-8,-7.8,-8.02,-8.05,-0.02),$$
$$W_3 = diag(-2,-0.095,0.85,0.5,0.75,-3),$$
$$W_4 = diag(0.02,0.03,0.025,0.028,0.035,0.2802),$$
$$W_5 = diag(0.1028,0.15,0.14,0.2,0.18,0.878),$$
$$K_1 = diag(0.1,0.14,0.18,0.23,0.25,0.00035),$$
$$K_2 = diag(0.15,0.36,0.28,0.18,0.23,0.00012),$$
$$K_3 = diag(0.0065,0.0008,0.006,0.0012,,00009,0.0001).$$

It is clear that all conditions of admissibility criteria for system (23) are satisfied. Therefore, the system (23) is admissible. Also, the graph showing the orbital behavior of the system (23) is as follows.

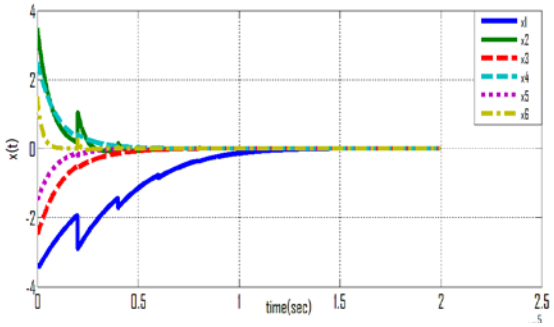

Figure 5. *Orbital behavior of the system (23).*

5. Conclusions

In this paper, we proposed new delay-dependent criteria for the admissibility of linear and nonlinear fractional singular systems with variable and constant delays. We used some useful lemmas and Lyapunov-Krasovskii functionals to obtain these proposed criteria. The numerical examples we present with graps at the end of the paper reveal the advantages and applicability of our results.

References

[1]. Alkhazzan A., Wang J., Tunç C., Ding X., Yuan Z., Nie, Y., "On Existence and Continuity Results of Solution for Multi-time Scale Fractional Stochastic Differential Equation'', *Qual. Theory Dyn. Syst.*, **22**, 49, (2023), 1-23. https://doi.org/10.1007/s12346-023-00750-x

[2]. Altun Y., "A new approach on the stability of fractional singular systems with time-varying delay'', MANAS Journal of Engineering, 8(1),(2020), 59-67.

[3]. Altun, Y., Tunc, C., On the asymptotic stability of a nonlinear fractional-order system with multiple variable delays. Applications and Applied Mathematics: An International Journal (AAM), 15(1), (2020), 458-468.

[4]. Chartbupapan C., Bagdasar O., Mukdasai K., "A Novel Delay-Dependent Asymptotic Stability Conditions for Differential and Riemann-Liouville Fractional Differential Neutral Systems with Constant Delays and Nonlinear Perturbation", Mathematics, 8, (2020), 1-10.

[5]. Chen W., Gao F., She J., Xia W., "Further results on delay-dependent stability for neutral singular systems via state decompsition method'', Chaos, Solitons and Fract., 141, (2020),110408.

[6]. Chen W., Gao F., 'New results on stability analysis for a kind of neutral singular systems with mixed delays'', Eur. J. Control 53, (2020), 59-67.

[7]. Dai L., "Singular control systems'', Lecture Notes in Control and Information Sciences, 118. Springer-Verlag, Berlin, 1989.

[8]. Graef JR., Tunç C., Şevli H., "Razumikhin qualitative analyses of Volterra integro-fractional delay differential equation with Caputo derivatives'', Commun. Nonlinear Sci. Numer. Simul.,103, (2021), 12 pp.

[9]. Hristova S., Tunç C., "Stability of nonlinear Volterra integro-differential equations with Caputo fractional derivative and bounded delays'', Electron. J. Differential Equations, 30, (2019), 1-11.

[10]. Kilbas AA., Srivastava HM., Trujillo JJ., "Theory and Application of Fractional Differential Equations'', Elsevier, New York, USA, 2006.

[11]. Korkmaz E., Ozdemir A., "Asymptotical Stability of Riemann-Liouville Fractional Neutral Systems with Multiple Time-varying Delays'', Applications and Applied Mathematics: An International Journal (AAM), 17, (2022) , Iss. 1, Article 7.

[12]. Liu S., Zhou XF., Li X., Jiang W., "Asymptotical stability of Riemann–Liouville fractional singular systems with multiple time-varying delays'', Appl. Math. Lett., 65, (2017), 32–39.

[13]. Lyapunov AM., "The General Problem of the Stability of Motion'', Üniv. Kharkov, PhD thesis, 1892.

[14]. Podlubny I., "Fractional Differential Equations'', Academic Press., New York, USA, 1999.

[15]. Tunç C., Tunç O., "Solution estimates to Caputo proportional fractional derivative delay integro – differential equations'', Rev. Real Acad. Cienc. Exactas Fis. Nat. Ser. A-Mat. 2023, 117, 12. [CrossRef]

[16]. Tunç C., "An application of Lyapunov functions to properties of solutions of a Caputo perturbed fractional differential system '', Int. J. Math. Comput. Sci., 17(2), (2022), 537-550.

[17]. Tunç O., Korkmaz E., "New Results on the Qualitative Analysis of Solutions of Vides by the Lyapunov-Razumikhin Technique '', Ukr Math J, 74, (2023), 1764-1779.

[18]. Tunç C., Yiğit A., "On the asymptotic stability of solutions of nonlinear delay differential equations'', Journal of Mathematical Sciences, 261(2), (2022), 337–352.

[19]. Wu Q., Song Q., Hu B., Zhao Z., Liu Y., Alsaadi FE., "Robust stability of uncertain fractional order singular systems with neutral and time-varying delays'', *Neurocomputing*, 41, (2020),145-152.

[20]. Wu ZG., Su H., Shi P., Chu J., "Analysis and synthesis of singular systems with time-delays'', Springer-Verlag, Berlin, 2013.

[21]. Xu S., Lam J., "Robust control and filtering of singular systems'', Lecture Notes in Control and Information Sciences, 332. Springer-Verlag, Berlin, 2006.

[22]. Yang W., Alsaedi A., Hayat T., Fardoun H.M., "Asymptotical stability analysis of Riemann-Liouville q-fractional neutral systems with mixed delays'', Math Meth Appl Sci, 42, (2019), 4876–4888.

[23]. Yiğit A., Tunç C., "Asymptotical stability of nonlinear fractional neutral systems with unbounded delay'', Applied Analysis and Optimization, 7(1), (2023), 63-77.

[24]. Yiğit A., Sivasundaram S., Tunç C., "Stability for fractional order delay singular systems'', Nonlinear studies (NS), 29(3), (2022), 865-879.

[25]. Zhang H., Ye R., Cao J., Ahmed A., Li X., Wan Y., "Lyapunov functional approach to stability analysis of Riemann–Liouville fractional neural networks with time-varying delays. Asian J. Control, 20(5), (2018), 1938–1951.

MANAS Journal of Engineering
ISSN 1694-7398 | e-ISSN 1694-7398

Volume 11, Issue 2, (2023) Pages 252-260
https://doi.org/10.51354/mjen.1217103

A new application for reading optical form with standard scanner by using image processing techniques

Fatih Taha Özcan[1], Ayşe Eldem[2,*]

[1] IT Department, Karamanoglu Mehmetbey University, Karaman, Turkey, fozcan@kmu.edu.tr, ORCID: 0000-0002-9012-0473

[2] Department of Computer Engineering, Karamanoglu Mehmetbey University, Karaman, Turkey, ayseeldem@kmu.edu.tr, ORCID: 0000-0002-5561-1568

ABSTRACT

Multiple choice exams appear as the most common method used to measure student success in education systems in Turkey and around the world. Evaluation of multiple choice exams is usually done by optical form reading systems using expensive optical forms and optical scanners. The most important reason for using optical form reading systems is to reduce the error rate to zero in the evaluation process. In this study, an alternative system is proposed for the evaluation of multiple choice exams. The designed system is a web-based software with high accuracy on evaluating that contains optical form design module, session planning module and evaluation module. The form in which the designed template will be printed on A4 paper instead of a special optical form and the system in which standard scanners will be used instead of the optical scanner, uses the image processing algorithms in the OpenCV library in the evaluation process which is an intermediate library developed in C#. The proposed system is coded to run in parallel to speed up the evaluation process. In order to determine the performance of the proposed system, the optical forms filled by 208 students studying at Karamanoğlu Mehmetbey University, Department of Computer Engineering were evaluated. The accuracy rate of the system has been determined as 99.97%. It has been determined that 1 optical evaluation time, calculated by dividing the total time obtained by running in parallel, by the number of evaluated optical forms, varies between 1.7 seconds and 15 seconds, depending on the scanning resolution.

ARTICLE INFO

Research article

Received: 9.12.2022
Accepted: 14.02.2023

Keywords:
image preprocessing techniques, multiple choice exam, optical form reading, segmentation, thresholding

**Corresponding author*

1. Introduction

The education system is considered as a purposeful process. The process of observing a quality and showing the observation data with numbers is defined as measurement, and the process of extracting a meaning from the measured values is defined as evaluation. One of the most important processes of the education system is the measurement and evaluation phase, which includes measuring how well the information given is understood, that is, determining the extent to which the objectives have been achieved. Evaluation reveals the performance of the entire education system, including the educator. Accurate calculation of the performance of the education system is very important in terms of determining the operational and non-operational aspects of the system and perfecting the education system[1].

Multiple choice tests are used both on a large scale and on a local scale in our country. In our education system, large-scale tests were started to be applied by ÖSYM, which was established in 1974, to centralize the exams made by faculties as a result of the increase in applications to universities [2]. With the widespread use of central multiple-choice exams, multiple-choice exams have started to be held at the local scale so that students who are in the preparation stage for these exams can adapt to the exam system. The most important reason why multiple-choice exams have become so widespread is that since it is easy to answer questions in these exams, they allow more comprehensive measurement due to the fact that more questions are asked. In addition, features such as obtaining statistics on the basis of questions in multiple-choice exams provide detailed information to the educator. Since participants are charged for centrally held multiple-choice exams, it facilitates the use of optical reading systems necessary for the reading and evaluation of these exams. Educators who want to prepare their students for national multiple-choice exams generally do not have the

opportunity to demand money for the exam they have prepared themselves. Therefore, educators usually evaluate multiple-choice exams manually. Manual multiple-choice exam evaluation is prone to errors; moreover, it takes a long time to transfer the data obtained to the computer environment to get detailed statistics, which is one of the most important features of multiple-choice exams.

The aim of this study is to develop a web-based optical form evaluation system for optical forms scanned with devices such as scanners or mobile phones, which are often in the hands of the institution or educator today, instead of purchasing an optical reader required for the evaluation of multiple-choice exams and using equipment that is costly in technical maintenance. The main purpose is to reduce the cost required for the evaluation of multiple choice exams. Since the system proposed in this study includes the answer sheet design, it will allow the use of standard A4 paper. In addition, since the proposed system has a module such as creating a session plan, it will also minimize cheating, which is the biggest problem of multiple choice exams.

Information about previous studies on optical form reading is given detailed.

Nguyen et al., in their published article, worked on the evaluation with high reliability and efficiency of answer sheets scanned with a digital camera by using image processing algorithms. Nguyen et al. tested the system they designed with 10000 questions and achieved an accuracy rate of 99.74% [3]. Aydemir worked on optical form reading in his master's thesis. Aydemir tested the system he designed with 28360 questions answered by 742 students in the foreign language exam and determined the accuracy rate of the developed system as 99.94% [4]. Al-Marakeby tried to find the evaluation results by processing the exam result images scanned using a digital camera with parallel processes thanks to the multi-core processor in his published article. Finally, classifier algorithms were preferred to determine whether the box was checked or not. As a result of the tests carried out with 200 multiple choice optical forms and 24000 question answers using different light, form angle originating from scanning, the success of the system was revealed as 99.8% [5]. Fisteus et al. have worked on a low-cost and portable computer vision-based system called "Eyegrade" for multiple choice exams in their article. In order to measure the performance of the system called "Eyegrade", the results of 233 students were evaluated and they measured that system made wrong assessment on 9 students paper and revealed the success rate as 96.1% [6]. In his article Sattayakawee studied a system for the evaluation of multiple choice exams with grid type answer sheets used in Thailand. In the tests made with 300 exam papers and 16500 questions, the accuracy rate of the proposed system was measured as 99.91% [7]. In their article, Şenol and Fidan designed an exam system that evaluates the optical forms scanned with a web camera developed in C# language in order to read the optical forms used in multiple choice test systems and to provide more detailed and valuable information to the educators by making statistical analyzes. In order to measure the performance of the designed system, the answer sheets of 221 students were scanned with a web camera and errors were detected in 7 answer sheets and the performance of the system was calculated as 96.83% [8]. Patel et al., in their article published in 2015, worked on a mobile application based system they named “CheckIt”. Patel et al. tried the "CheckIt" system with 310 quizzes and tests questions and achieved a success rate of 97.48% [9]. In the article they published, Hasan and Kareem worked on a system to be used in the evaluation of multiple choice exams. Hasan and Kareem determined the accuracy rate of the artificial neural network algorithms based system as 99.96% in the test they performed with 800 answer sheets and 58000 questions [10]. Yüksel et al. have worked on a mobile application-based optical form evaluation system in the article they published. The highest success of the system was measured as 99.7% in the tests made with 1000 questions on 20 answer sheets [11]. Gyamfi and Missah worked on the optical form evaluation system they proposed for multiple choice exams in their published articles. As a result of the tests, it was revealed that the system using unsupervised learning on the basis of pixels has better performance [12]. Loke et al. proposed a new method for optical form recognition in their published paper. In the first category, 6000 questions were filled and tested by people who were not trained on how to mark, and the accuracy rate of the proposed method was measured as 99.97%. In tests with printing and scanning errors, the accuracy rate of the proposed method was measured as 99.3% [13]. Küçükkara and Tümer worked on the reading and evaluation of answer sheets for multiple choice exams in their published articles. They tested the proposed system with 105750 answer sheets in three exams attended by 35250 students in Konya and calculated the accuracy rate as 99.76%[14]. Espitia et al., in the article they published, worked on the evaluation of the answer sheets of exams such as the university entrance exam or graduation exam in Colombia using image processing algorithms. The system designed by Espitia et al. was tested with 64940 answer sheets and it was found that it achieved an accuracy rate of 99.70% [15]. In the article they published, Afifi and Hussain studied classification-based algorithms for multiple choice exams. In their tests using MATLAB, they used different classification algorithms and were able to achieve the maximum accuracy rate of 99.78% by using the CNN classification algorithm [16]. Ha and Thu studied on optical form reading using MATLAB in the article they published. They measured the success rate of the developed system as 100% in their tests using 170 optical forms [17].

In this study, a system called "Multiple Choice Examination System" is proposed instead of costly optical form reading systems, in which the optical form designed by using the system can be printed on A4 paper and standard scanners are used instead of optical scanners. The designed system is

separated from previous studies by consisting of modules such as creating a seating plan, designing optical form and evaluating optical form.

In this article, the image processing steps used during optical form evaluation are explained in the second part. The application and evaluation steps are explained in detail in the third section, and the performance of the system is explained in the fourth section.

2. Material and Method

The system proposed in this study consists of a three-stage structure. The first stage consists of making the definitions including the optical form design, the second stage is the session plan and the printing of the optical forms customized according to the student and the examination, the third stage consists of scanning the marked optical forms and performing the evaluation process after uploading scanned optical forms to the system. Evaluation phase of optical forms consists of grayscale conversion, Gaussian smoothing filter, morphological opening process, thresholding and conversion to binary image, edge detection, contour extraction, and Hough circle transform, which are explained in detail below.

2.1. Convert to Grayscale

In colored images, each pixel is represented by 24-bit data. During image processing, instead of using the color values of 3 different colors in an image, a grayscale image consisting of values between 0 and 255, where a pixel can be expressed with 8-bit data without losing detail, is used. Thus, the size of the optical form image file is reduced to one third.

2.2. Gaussian Smoothing Filter

Using the Gauss function to blur the image, reduce detail and noise is called a Gaussian smoothing filter. Gaussian smoothing filter can be defined as two-dimensional convolution in general. The Gaussian smoothing filter can be expressed by the function shown in Equation (1) [18].

$$G(x) = \frac{1}{(2\pi\sigma^2)^{N/2}} e^{-(x-\mu)^2/(2\sigma^2)} \quad (1)$$

In Equation (1), "G" refers to Gaussian probability density function, "σ" refers to standard deviation of Gaussian noise, "e" refers to base of natural logarithm, "N" refers to the size of the image, "x" refers to grayscale value and "μ" refers to the mean value of Gaussian noise.

2.3. Morphological Opening

It is obtained by applying a dilation process after an erosion process. It is used to get rid of noise while preserving the properties of large shapes. Equation (2) shows the function of the morphological expansion operation.

$$\boldsymbol{A \circ B = (A \Theta B) \oplus B} \quad (2)$$

In Equation (2); "A" refers to image to open and "B" refers to the structural element that determines the shape of the opening process.

2.4. Thresholding and Conversion to Binary

Thresholding, which is one of the most basic segmentation methods, is the process of separating the objects in the image from the background of the image. The image input, which is given as grayscale, is returned as a binary image. Basically, it is aimed to change the pixels below the determined threshold value in grayscale images to black pixels, i.e. 0, and to change the pixels to white, i.e. 255, higher than the threshold value. Thresholding is also used to remove noise in the image. Here, the success of the thresholding depends on the determined threshold value. Basically, the Otsu thresholding algorithm returns a single threshold value to minimize the within-class variance and maximize the variance between classes. Equation (3) shows the variance function between classes.

$$\boldsymbol{\sigma_\omega^2(t) = \omega_0(t)\sigma_0^2(t) + \omega_1(t)\sigma_1^2(t)} \quad (3)$$

In Equation (3); "σ_w" refers to within-class variance, "*t*" refers to threshold value, weights "ω_0" and "ω_1" refer to probabilities of two classes separated by "*t*" threshold, "σ_0" and "σ_1" refer to the variance of the two classes separated by the *t* threshold.

2.5. Canny Edge Detection

Canny edge detection method is one of the most common methods used to find the edges of objects and shapes in an image. In this method, two threshold values are given as parameters. The method generally consists of 5 steps. Table 1 shows pseudocodes of the Canny edge detection algorithm.

Table 1. *Canny edge detection pseudocode*

Start:
Apply noise reduction with Gaussian Blur
Refine edge with non-maximum suppression
Perform pixel continuity test using double threshold value and detect strong, weak and irrelevant pixels
Convert weak pixels to strong pixels by examining neighboring pixels by edge tracking with hysteresis.
End:

2.6. Contour Extraction

Contour extraction can be defined as finding a closed curve that seamlessly connects pixels of the same color and intensity by grouping them together. Commonly contours are objects found in an image.

2.7. Hough Circle Transform

The Hough transform was found by Paul Hough in 1962 to determine whether mathematically expressible shapes exist on the picture, and if so, its location and angle. The method works with simple bit voting logic. Dana H. Ballard made improvements in 1981 for the detection of objects more general to the algorithm[19]. During the Hough transform circle detection, the functions shown in Equations (4), (5) and (6) are used.

$$\boldsymbol{r^2 = (x - a)^2 + (y - b)^2} \quad (4)$$

$$\boldsymbol{a = x - r \times \cos(\theta)} \quad (5)$$

$$\boldsymbol{b = y - r \times \sin(\theta)} \quad (6)$$

In Equations (4), (5) and (6); "r" refers to radius of the circle, "a" refers to coordinate of the center of the circle on the x-axis "b" refers to Coordinate of the center of the circle on the y-axis, "θ" refers to angle between (0.2π), "x" refers to coordinate of the image point on the x-axis and "y" refers to coordinate of the image point on the y-axis.

2.8. Parallel Programming

Parallel programming, the foundation of which was laid by John Cocke and Daniel Slotnick in 1958 with a computer design called SOLOMON, refers to the completion of a large and time-consuming computation in a shorter time on multiple processors simultaneously [20]. It is predicted that the size of the optical form image files to be evaluated within the scope of this study will increase as the scanning resolutions increase and the evaluation process will take longer. Therefore, in this study, parallel programming structure is used to reduce the evaluation time.

3. Application

In order to create a multiple-choice exam system, first of all, pages were designed to carry out the definition processes to be made before the exam. In these pages; user operations, unit operations, exam definition procedures, exam correct answers procedures, student procedures to take the exam, classroom procedures, session planning processes and the design of the optical form to be used in the exam are carried out. The design of these pages is shown in Figure 1.

Figure 2 shows the evaluation workflow of the system. Image file containing optical form data respectively is subjected to image processing algorithms like grayscale conversion, application of Gaussian smoothing filter to reduce noise, applying morphological opening to remove black pixel distortions, thresholding and binary level transform, angular correction, contour extraction, QR code extraction and Hough circle transform. To decide whether the option is checked, the largest square that will fit inside the circle is found, and the option is considered checked if at least 50% of the square's area is ticked.

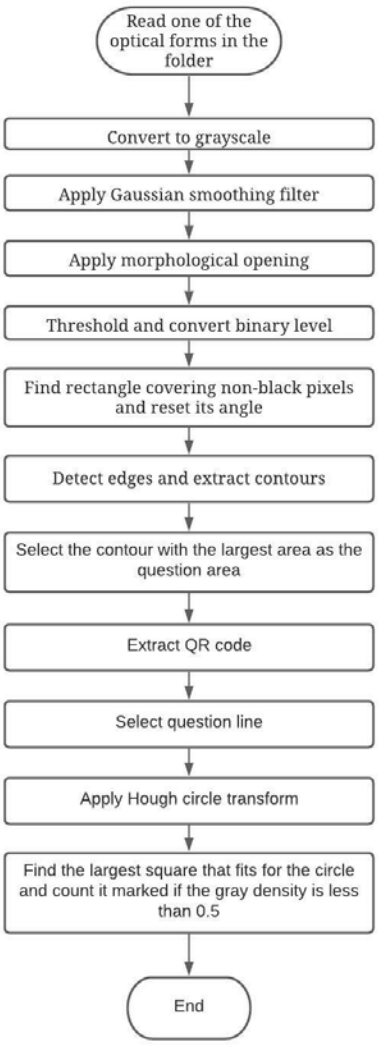

Figure 2. *Evaluation workflow*

The results obtained when the techniques mentioned are applied to the optical form are shown in Figure 3. After the aforementioned pre-processing steps, QR code extraction was performed as seen in Figure 4. According to the location of the QR code found, it is decided whether the image is inverted and, if necessary, the image is rotated 180 degrees again.

.

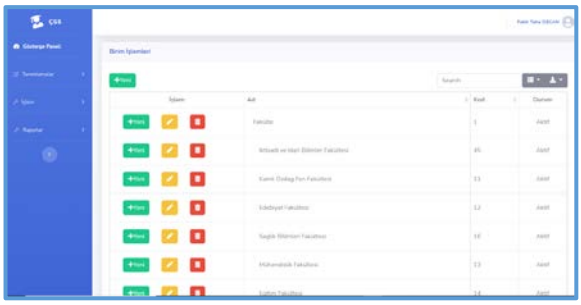

(a) Unit operations page

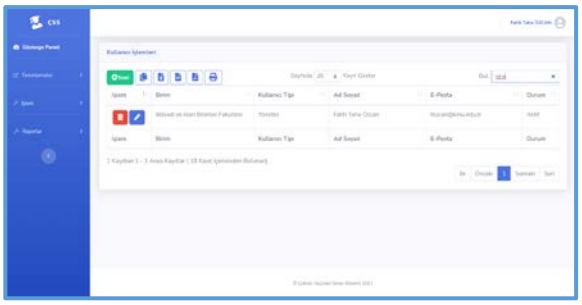

(b) User operations page

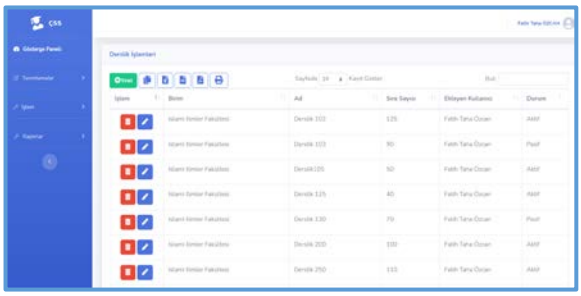

(c) Classroom operations page

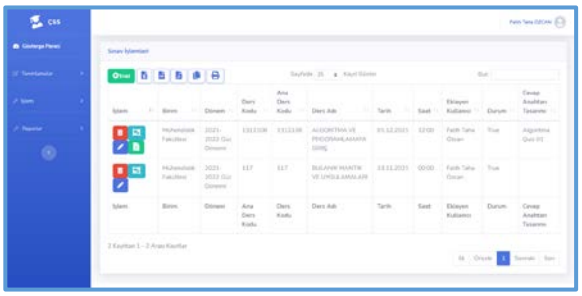

(d) Exam operations page

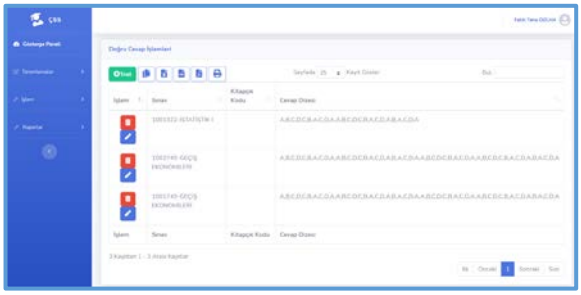

(e) Correct answer operations page

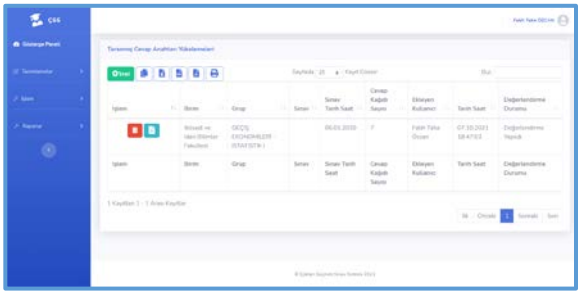

(f) Scanned optical form operations page

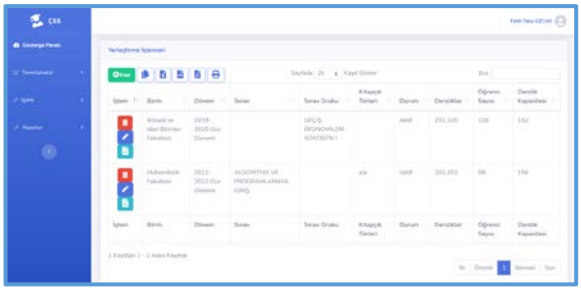

(g) Session planning operations page

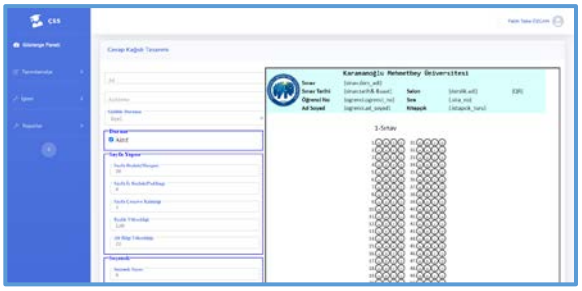

(h) Optical form design page

Figure 1. *Interface of the system*

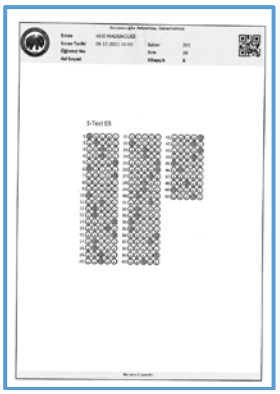

(a) Colored image is converted to grayscale image for reducing the memory space of the file.

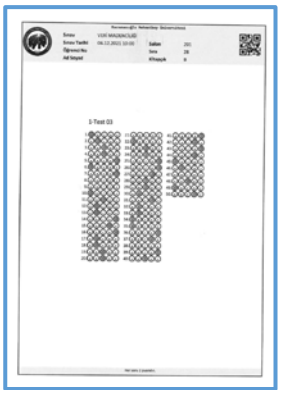

(b) Gaussian filter is applied to reduce noise.

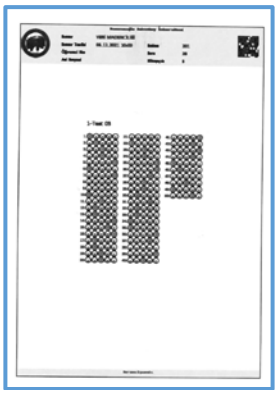

(c) Morphological opening is applied to remove the breaks in the black pixels.

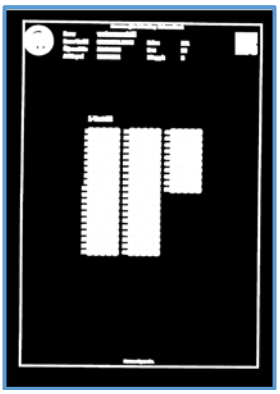

(d) Thresholding is applied to reduce noise and the image is converted to binary image. Since image processing algorithms generally perceive black pixels as background, black and white pixels are switched.

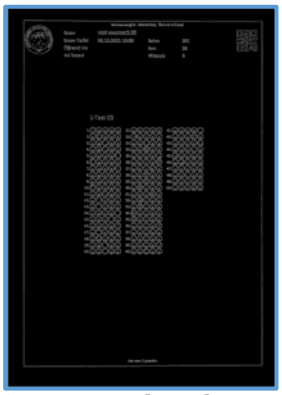

(e) Canny edge detection algorithm is applied to detect the edges in the image.

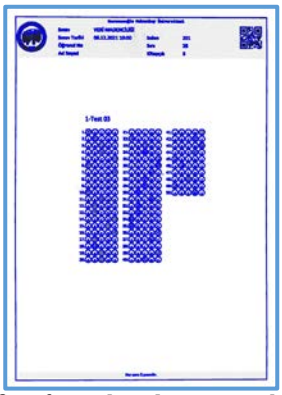

(f) After edge detection, the contours in the image are searched and the rectangular contour with the largest area is selected as the response area.

(g) The image translation algorithm is applied to reset the angle of the selected rectangle.

Figure 3. *Evaluation detailed steps*

Figure 4. *QR code check*

Question evaluation steps were applied as shown in Figure 5.

(a) The question line is determined with the help of the previously calculated scale.

(b) The circles in the found question line are determined using the Hough circle transform algorithm.

(c) The largest square to fit inside the detected circles is calculated and for each option, the gray color intensity in this selected square is proportioned to 255. If the ratio is less than 0.5, the option is considered marked.

Figure 5. *Question evaluation stages*

After evaluating all the questions, the correct answers are marked in green, the wrong answers in red, the correct answers in the wrong or empty options are marked in blue, and the invalid answers are marked in purple. An orange line is used for blank questions and a purple cross for invalid questions. The resulting markings are shown in Figure 6.

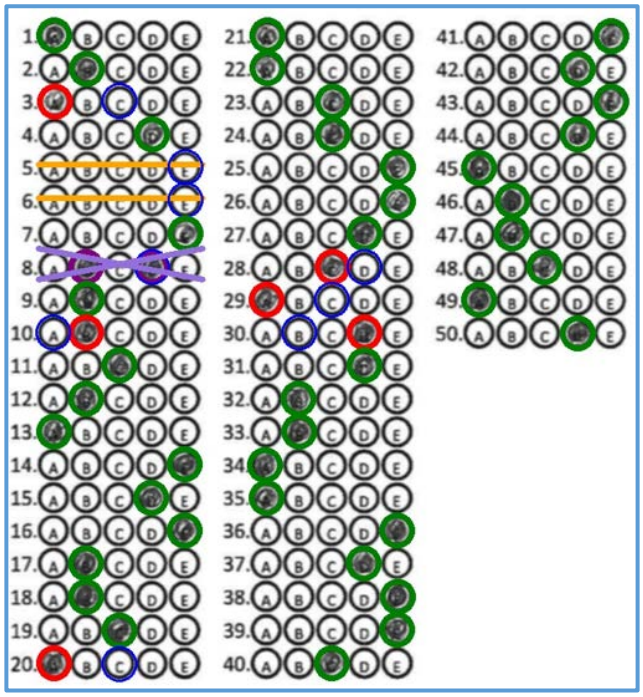

Figure 6. *Answer sheet marked by the system*

4. Result and Discussion

In order to measure the accuracy and performance of the designed system, the evaluation of 5785 questions in 208 optical forms in 3 different exams of the students studying at the Computer Engineering Department of Karamanoğlu Mehmetbey University was made at 3 different scanner resolution levels. As a result of these tests, the accuracy rate of the web-based optical form reading system was measured as 99.9%. In Figure 7, 3 different optical form designs used in exams are shown. The system designed in the study was tested

with questions with 4 or 5 options, different columns and questions.

In Table 2, the test results are shown in detail on the basis of scanning resolution. Since the evaluation period of the system is an important indicator in terms of performance, the tests were carried out both in parallel and in series. During the tests, the time taken to evaluate one optical form is between 2.8 seconds and 1.8 seconds when scanned at 200 DPI resolution, between 8.3 seconds and 5.8 seconds when scanned at 300 DPI resolution, and between 16 seconds and 10.9 seconds when scanned at 600 DPI resolution. In Table 3, the time performance of the system is shown in detail on the basis of scanning resolution.

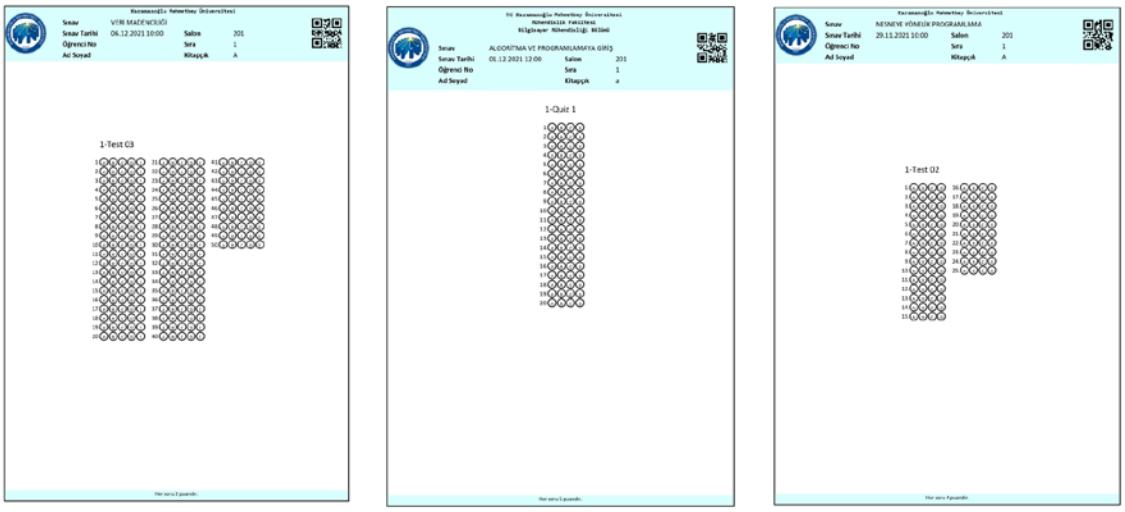

Figure 7. *Optical form designs used in exams*

Table 2. *The accuracy performance of the system*

		Number of Optical Forms Uploaded	Percentage of Errorless Optical Forms	Number of Questions	Percentage of Questions Read Correctly	Number of Options	Percentage of Correctly Evaluated Options
DPI	200	208	96.63%	5785	99.88%	25140	99.97%
	300	208	93.75%	5785	99.74%	25140	99.94%
	600	208	87.98%	5785	99.46%	25140	99.88%

Table 3. *Time performance of the system*

	Number of Optical Forms Evaluated	1 Optical Form Evaluation Time (Second)	1 Optical Form Evaluation Time (Seconds) in Parallel Mode
200 DPI	208	2.815	1.795
300 DPI	208	8.277	5.774
600 DPI	208	16.062	10.882

As a result of the test studies, it has been revealed that the most optimal performance of the system will be achieved with 200DPI scanning resolution and parallel operation. In order to increase the correct reading performance to 100%, it is thought that it will be achieved by informing the students more about marking and the use of optical form.

References

[1]. Temizkan, M. and M.E. Sallabaş, Okuduğunu Anlama Becerisinin Değerlendirilmesinde Çoktan Seçmeli Testlerle Açık Uçlu Yazılı Yoklamaların Karşılaştırılması. Dumlupınar Üniversitesi Sosyal Bilimler Dergisi, 2011(30): p. 207-220.

[2]. Çakan, M., Geniş ölçekli başarı testlerinin eğitimindeki yeri ve önemi. Eğitim ve Bilim, 2003. 28(128).

[3]. Nguyen, T.D., et al. Efficient and reliable camera based multiple-choice test grading system. 2011. IEEE.

[4]. Aydemir, F., Standart Tarayıcılarla Web Tabanlı Bilgisayar Mühendisliği. 2012.

[5]. Al-Marakeby, A., Multi Core Processors for Camera based OMR. International Journal of Computer Applications, 2013. 68(13): p. 1-5.

[6]. Fisteus, J.A., A. Pardo, and N.F. García, Grading multiple choice exams with low-cost and portable computer-vision techniques. Journal of Science Education and Technology, 2013. 22(4): p. 560-571.

[7]. Sattayakawee, N., Test scoring for non-optical grid answer sheet based on projection profile method. International Journal of Information and Education Technology, 2013. 3(2): p. 273-273.

[8]. Şenol, M. and U. Fidan, C# ile Web Kameradan Optik Form Okuma. Afyon Kocatepe University Journal of Science & Engineering, 2014. 14(2).

[9]. Patel, R., et al. CheckIt-A low cost mobile OMR system. 2015. IEEE.

[10]. Hasan, R.H. and E.I.A. Kareem, An Image Processing Oriented Optical Mark Reader Based on Modify Multi-Connect Architecture MMCA. International Journal of Modern Trends in Engineering and Research (IJMTER), 2015. 2(7).

[11]. Yüksel, A.S., et al., Mobile based optical form evaluation system. Pamukkale Üniversitesi Mühendislik Bilimleri Dergisi, 2016. 22(2): p. 94-99.

[12]. Gyamfi, E.O. and Y.M. Missah, Pixel-Based Unsupervised Classification Approach for Information Detection on Optical Markup Recognition Sheet. Advances in Science, Technology and Engineering Systems Journal, 2017. 2(4): p. 121-132.

[13]. Loke, S.C., K.A. Kasmiran, and S.A. Haron, A new method of mark detection for software-based optical mark recognition. Plos One, 2018. 13(11).

[14]. Küçükkara, Z. and A.E. Tümer, An Image Processing Oriented Optical Mark Recognition and Evaluation System. International Journal of Applied Mathematics Electronics and Computers, 2018. 6(4): p. 59-64.

[15]. Espitia, O., et al. Optical Mark Recognition Based on Image Processing Techniques for the Answer Sheets of the Colombian High-Stakes Tests. 2019. Springer.

[16]. Afifi, M. and K.F. Hussain, The achievement of higher flexibility in multiple-choice-based tests using image classification techniques. International Journal on Document Analysis and Recognition (IJDAR), 2019. 22(2): p. 127-142.

[17]. Ha, T. and N. Thu, An Application of Image Processing in Optical Mark Recognition. Vietnam Journal of Agricultural Sciences, 2020. 3(4 SE - ENGINEERING AND TECHNOLOGY).

[18]. Çayıroğlu, İ., Resim Yumuşatma (Bulanıklaştırma-Blurrıng) Filtreleri. 2021.

[19]. Ballard, D.H., Generalizing the Hough transform to detect arbitrary shapes. Pattern Recognition, 1981. 13(2): p. 111-122.

[20]. Şaan, T.G., MPI İle Paralel Programlama. 2017.